UNIVERSIDAD NACIONAL AUTÓNOMA DE MÉXICO

POSGRADO EN CIENCIAS FÍSICAS
INSTITUTO DE FÍSICA

Light Scattering in Stimuli-Responsive Colloidal Systems: Mie Scattering Solution for Radially Nonhomogeneous PNIPAM and Core/Shell Particles

TESIS
QUE PARA OPTAR POR EL GRADO DE:
DOCTOR EN CIENCIAS (FÍSICA)

PRESENTA:
CHRISTIAN IGNACIO BALDERAS CABRERA

TUTOR PRINCIPAL
DR. ROLANDO C. CASTILLO CABALLERO
INSTITUTO DE FÍSICA, UNAM

MIEMBRO DEL COMITÉ TUTOR
DR. CARLOS IGNACIO MENDOZA RUÍZ
INSTITUTO DE INVESTIGACIÓN EN MATERIALES, UNAM

MIEMBRO DEL COMITÉ TUTOR
DR. JOSÉ MIGUEL MÉNDEZ ALCARAZ
DEPARTAMENTO DE FÍSICA, CINVESTAV

CIUDAD DE MÉXICO, MÉXICO, 2025

PROTESTA UNIVERSITARIA DE INTEGRIDAD Y HONESTIDAD ACADÉMICA Y PROFESIONAL
(Graduación con trabajo escrito)

De conformidad con lo dispuesto en los artículos 87, fracción V, del Estatuto General, 68, primer párrafo, del Reglamento General de Estudios Universitarios y 26, fracción I, y 35 del Reglamento General de Exámenes, me comprometo en todo tiempo a honrar a la Institución y a cumplir con los principios establecidos en el Código de Ética de la Universidad Nacional Autónoma de México, especialmente con los de integridad y honestidad académica.

De acuerdo con lo anterior, manifiesto que el trabajo escrito titulado:

Light Scattering in Stimuli-Responsive Colloidal Systems: Mie Scattering Solution for Radially Nonhomogeneous PNIPAM and Core/Shell Particles

que presenté para obtener el grado de ----Doctorado---- es original, de mi autoría y lo realicé con el rigor metodológico exigido por mi programa de posgrado, citando las fuentes de ideas, textos, imágenes, gráficos u otro tipo de obras empleadas para su desarrollo.

En consecuencia, acepto que la falta de cumplimiento de las disposiciones reglamentarias y normativas de la Universidad, en particular las ya referidas en el Código de Ética, llevará a la nulidad de los actos de carácter académico administrativo del proceso de graduación.

Atentamente

Christian Ignacio Balderas Cabrera
521000459

(Nombre, firma y Número de cuenta de la persona alumna)

VNIVERSIDAD NACIONAL AVPNMA DE MEXICO

COORDINACIÓN GENERAL DE ESTUDIOS DE POSGRADO

CARTA AVAL PARA DAR INICIO A LOS TRÁMITES DE GRADUACIÓN

Universidad Nacional Autónoma de México
Secretaría General
Coordinación General de Estudios de Posgrado

Dr. Alberto Güijosa Hidalgo
Programa de Posgrado en Ciencias Físicas
Presente

Quien suscribe, **Dr. Rolando Crisostomo Castillo Caballeo**, tutor(a) principal de **Christian Ignacio Balderas Cabrera**, con número de cuenta **521000459**, integrante del alumnado de **Doctorado en Ciencias (Física)** de ese programa, manifiesto bajo protesta de decir verdad que conozco el trabajo escrito de graduación elaborado por dicha persona, cuyo título es:

Light Scattering in Stimuli-Responsive Colloidal Systems: Mie Scattering Solution for Radially Nonhomogeneous PNIPAM and Core/Shell Particles

, así como el reporte que contiene el resultado emitido por la herramienta tecnológica de identificación de coincidencias y similitudes con la que se ~~analizó ese trabajo, para la prevención de faltas de integridad académica.~~

De esta manera, con fundamento en lo previsto por los artículos 96, fracción III del Estatuto General de la UNAM; 21, primero y segundo párrafos, 32, 33 y 34 del Reglamento General de Exámenes y; 22, 49, primer párrafo y 52, fracción II del Reglamento General de Estudios de Posgrado, **AVALO** que el trabajo de graduación presentado se envíe al jurado para su revisión y emisión de votos, por considerar que cumple con las exigencias de rigurosidad académica previstas en la legislación universitaria.

Protesto lo necesario,

Ciudad Universitaria, Cd. Mx., a 18 de Marzo de 202 5

Dr. Rolando Crisostomo Castillo Caballero

Tutor(a) principal

Light Scattering in Stimuli-Responsive Colloidal Systems: Mie Scattering Solution for Radially Nonhomogeneous PNIPAM and Core/Shell Particles

A dissertation submitted to the
Posgrado en Ciencias Físicas
Universidad Nacional Autónoma de México
for the degree of
Doctor of Science (Physics)

presented by
Christian Balderas-Cabrera MSc.
PhD. Advisor
Dr. Rolando Castillo

Mexico 2025

A todos mis profesores de la Licenciatura en Física y Matemáticas de la Escuela Superior de Física y Matemáticas del IPN, en especial a los profesores Arturo Méndez Sánchez, Leonor Pérez Trejo, Germán González Santos, y a quienes ya no están con nosotros: los profesores José Antonio "el Tony" Peralta y Rubén Mares Gallardo.

To all my professors from the Physics and Mathematics undergraduate program at the Escuela Superior de Física y Matemáticas (ESFM) of the Instituto Politécnico Nacional (IPN), especially Professors Arturo Méndez Sánchez, Leonor Pérez Trejo, Germán González Santos, and to those who are no longer with us: Professors José Antonio "El Tony" Peralta and Rubén Mares Gallardo.

Agradecimientos

Deseo expresar un afectuoso agradecimiento al Dr. Rolando Castillo por haber sido mi mentor durante esta etapa de mi vida académica. He aprendido mucho de él y espero poder retribuirle en el futuro, siguiendo el ejemplo que nos dio como educador de estudiantes de posgrado y como científico.

Agradezco hoy y siempre a los miembros del comité sinodal, el Dr. José Méndez Alcaraz y el Dr. Carlos Mendoza Ruíz. Sus observaciones y acompañamiento han sido de gran valor en mi desarrollo profesional.

Esta tesis estaría incompleta sin el Dr. Pedro Díaz Leyva, quien nos permitió utilizar su laboratorio en la UAM-Iztapalapa, lo cual fue fundamental para realizar los experimentos de esparcimiento de luz estática que aquí se reportan. También quiero reconocer el valioso apoyo recibido en los laboratorios del grupo de Fluidos Complejos del IFUNAM, en especial de la M. en C. Cristina Garza, con quien aprendí los procedimientos experimentales para la síntesis de las partículas utilizadas en esta investigación, y de Erick Guzmán por todo el soporte técnico brindado.

Agradezco profundamente las atenciones brindadas por el Dr. Raúl Esquivel Sirvent, el Dr. Augusto García Valenzuela, el Dr. Pedro Díaz Leyva, el Dr. José Méndez Alcaraz y la Dra. Catalina Haro Pérez, quienes amablemente aceptaron formar parte del comité evaluador de este trabajo de tesis.

Reconozco con gratitud el apoyo de la Universidad Nacional Autónoma de México, cuyos recursos no solo me permitieron realizar esta investigación, sino también conocer otros países y aprender cómo se hace ciencia fuera de México.

Agradezco también profundamente al CONACYT (ahora SECIHTI) por la beca otorgada para mi manutención durante los estudios de doctorado.

Mi estancia en el Instituto de Física fue más llevadera gracias a la compañía de mis compañeros de posgrado —y ahora grandes amigos— Ricky Santiago y Arturo Reyes. Sinceramente extraño nuestras pláticas durante la comida y las risas compartidas a la hora del café.

Hoy sé que no habría podido culminar mis estudios doctorales sin el amor y el apoyo incondicional de mi dulce esposa Lizeth, ni sin la amorosa presencia de mis entrañables amigos Oscar y Heira, a quienes siempre llevo en el corazón.

Finalmente, mi familia ha sido un pilar fundamental en mi formación humana y mi apoyo en las buenas y en las malas. Por ello, agradezco hoy y siempre a mi mamá Cristina, a mis hermanos Oscar y Anahí, a mi papá Ignacio y a mis tías Bety y Tere.

Acknowledgments

I wish to express my heartfelt gratitude to Dr. Rolando Castillo for being my mentor during this stage of my academic journey. I have learned a great deal from him and hope to give back in the future by following his example as a mentor to graduate students and as a scientist.

I am forever grateful to Dr. José Méndez Alcaraz and Dr. Carlos Mendoza Ruíz, the members of my thesis committee. Their thoughtful feedback and support have been invaluable to my professional development.

This thesis would not be complete without the contribution of Dr. Pedro Díaz Leyva, who kindly allowed us to use his laboratory at UAM-Iztapalapa, making it possible to carry out the static light scattering experiments presented in this work. I also want to acknowledge the support received in the Complex Fluids group laboratories at IFUNAM, particularly from M.Sc. Cristina Garza, who taught me the experimental procedures for synthesizing the particles used in this research, and Erick Guzmán, for all his technical assistance.

I deeply appreciate the kindness and support of Dr. Raúl Esquivel Sirvent, Dr. Augusto García Valenzuela, Dr. Pedro Díaz Leyva, Dr. José Méndez Alcaraz, and Dr. Catalina Haro Pérez, who graciously agreed to serve as members of my thesis defense committee.

I am sincerely thankful to the National University of Mexico, whose resources not only enabled me to complete this doctoral research but also gave me the opportunity to travel abroad and experience how science is done in other parts of the world.

I am also grateful to CONACYT (now SECIHTI) for the scholarship that supported me throughout my doctoral studies.

My time at the Institute of Physics was made much more enjoyable by the company of my fellow graduate students —and now dear friends— Ricky Santiago and Arturo Reyes. I truly miss our lunchtime conversations and the laughter we shared over coffee.

Today, I know that I would not have completed my PhD studies without the love and unconditional support of my sweet wife Lizeth, nor without the heartfelt presence of my dear friends Oscar and Heira, who will always have a place in my heart.

Lastly, my family has been a cornerstone in my human development and a source of unwavering support through good times and bad. For this, I am forever grateful to my mother, Cristina; my siblings, Oscar and Anahí; my father, Ignacio; and my aunts, Bety and Tere.

Contents

Resumen

El estudio del esparcimiento de luz por partículas coloidales es esencial para comprender y controlar las propiedades ópticas de medios complejos. Las técnicas de esparcimiento de luz son especialmente eficaces para caracterizar parámetros físicos clave como el tamaño, la forma y el índice de refracción de las partículas. Estas mediciones son particularmente relevantes en sistemas fotónicos desordenados, donde el transporte de luz está gobernado por eventos de esparcimiento múltiple. La fotónica desordenada tiene diversas aplicaciones, incluyendo el desarrollo de recubrimientos ópticos y sensores ultrasensibles. En estos sistemas, ajustar tanto la estructura coloidal como las propiedades intrínsecas de las partículas, como el índice de refracción y la química superficial, es fundamental para controlar las interacciones luz, materia.

En este contexto, las suspensiones de microgeles sensibles a estímulos, como el Poli(N-IsoPropil Acrilamida) (PNIPAM) y las partículas núcleo-caparazón recubiertas con PNIPAM, representan una estrategia prometedora. Estos sistemas permiten modificar sus propiedades estructurales y ópticas mediante estímulos externos, como la temperatura. Sin embargo, la estructura interna de los microgeles de PNIPAM da lugar a perfiles dieléctricos radialmente inhomogéneos. A pesar de esta complejidad, su comportamiento frente al esparcimiento de luz se analiza comúnmente mediante la aproximación de Rayleigh-Gans-Debye, principalmente por su simplicidad matemática, incluso cuando sus condiciones de validez no son estrictamente válidos.

Esta tesis revisa la solución de esparcimiento de Mie para partículas esféricas homogéneas y multicapa, proporcionando un enfoque exacto al problema del esparcimiento electromagnético. Se desarrollan algoritmos numéricos para ambos casos, incorporando la polidispersidad para modelar con mayor precisión los sistemas experimentales. Estas herramientas se aplican al estudio del esparcimiento de luz por partículas de PNIPAM y partículas núcleo-caparazón recubiertas con PNIPAM. Hasta donde sabemos, esta es la primera vez que se describe el factor de forma de microgeles de PNIPAM hinchados en el régimen de Mie utilizando un perfil radial de índice de refracción. Los resultados demuestran que la teoría de Mie puede aplicarse con éxito a partículas coloidales homogéneas y radialmente inhomogéneas, ofreciendo un marco riguroso y general más allá de las aproximaciones tradicionales.

Abstract

The study of light scattering by colloidal particles is essential to understanding and controlling the optical properties of complex media. Light scattering techniques are particularly effective for characterizing key physical parameters such as particle size, shape, and refractive index. Also, measuring the scattering form factor is especially relevant in disordered photonic systems, where multiple scattering events govern light transport. Disordered photonics has diverse applications, including the development of optical coatings and ultrasensitive sensors. In such systems, tuning both the colloidal structure and the intrinsic properties of the particles, such as refractive index and surface chemistry, is critical to controlling light-matter interactions.

In this context, suspensions of stimuli-responsive microgels, such as Poly(N-IsoPropyl Acrylamide) (PNIPAM) and PNIPAM-coated core-shell particles, represent a promising strategy. These systems enable the modulation of structural and optical properties via external parameters like temperature. However, the internal structure of PNIPAM microgels results in radially inhomogeneous dielectric profiles. Despite this complexity, their light scattering behavior is often analyzed using the Rayleigh-Gans-Debye approximation, largely due to its mathematical simplicity, even in cases where its assumptions are not strictly valid.

This dissertation revisits the Mie scattering solution for homogeneous and multilayer spherical particles, providing an exact approach to the electromagnetic scattering problem. Numerical algorithms are used for both cases, incorporating polydispersity to model experimental systems more accurately. These tools are applied to study the light scattering behavior of PNIPAM and PNIPAM-coated core-shell particles. As far as we know, this is the first time that the form factor of PNIPAM microgels in the swollen state has been described using a radial refractive index profile in the Mie regime. The results demonstrate that Mie theory can be successfully applied to both homogeneous and radially inhomogeneous colloidal particles, offering a rigorous and general framework beyond traditional approximations.

Chapter 1

Introduction

Disordered photonics is a research field that studies the propagation of light through materials or media whose structure does not have a periodic arrangement like that of crystalline solids. [1,2] Unlike conventional photonics, where optical properties are defined by the Bragg condition for a crystal lattice, among other intrinsic properties of crystalline materials, [1–4] disordered photonic media exhibit multiple light scattering, which can lead to diffusive light transport. This behavior can give rise to unusual photonic phenomena, often related to Anderson's localization of the light. [1, 2, 5, 6]. Anderson localization of light is a phenomenon where light transport through disordered media is inhibited. Although it remains primarily a theoretical prediction, it has motivated intense research into the role of the short-range correlations in disordered structures and how engineered correlated disordered media can achieve bandgaps in light transmission or even angle-independent structural colors. [1, 2, 6, 7] Among these media, colloidal suspensions have emerged as versatile model systems due to their capacity to synthesize colloidal particles with well-defined optical properties and their relative ease of experimental manipulation. [2, 8–10]

Disordered photonics has applications spanning a wide range of technological areas. [1,2] Notably, colloidal systems have been proposed for the development of efficient optical coatings, [6, 8] as well as ultrasensitive sensors based on the modification of light transport. [11–13] Furthermore, the possibility of controlling light scattering in these systems has led to their study in the fabrication of random laser devices with potential applications in bioimaging. [1, 2]

Tuning both the structural properties of the colloidal system and the intrinsic characteristics of the colloidal particles is essential to maximizing the performance of these systems in practical applications. Parameters such as particle size, shape, refractive index, and surface functionalization can significantly modify light-matter interactions. [2, 13–15] In this context, the use of stimuli-responsive microgel suspensions, such as Poly(N-IsoPropylAcrylamide) (PNIPAM) and PNIPAM-coated core/shell particle suspensions represent a promising strategy, as they allow simultaneous modification of the structure of the colloidal system, given by the static structure factor, $S(q)$, and

the individual scattering properties of the colloidal particles, provided by the form factor function, $F(\theta)$. [2, 14–17] Thanks to their ability to change size in response to external stimuli, such as temperature, PNIPAM microgel suspensions provide an adaptable platform for engineering dynamic and reconfigurable photonic media. [12,15,18] Given the broad scope of the problem of understanding the photonic properties of colloids, this work focuses on studying the light scattering properties of PNIPAM particles and PNIPAM-coated core/shell particles.

PNIPAM microgel suspensions are made of stimuli-sensitive gel particles obtained during cross-linking N-IsoPropyl Acrylamide (NIPAM) polymerization. [19, 20] When PNIPAM microgels are suspended in water, the microgel network could change their size with temperature; in warmed PNIPAM suspension above cloud point, they undergo a reversible phase transition from a hydrated state (expanded particles) to a dehydrated state (shrunk particles). This transition occurs at around 32 °C, known as the Lower Critical Solution Temperature (LCST). [19, 20]

In the PNIPAM microgels synthesis, the polymers of NIPAM are intentionally cross-linked. Otherwise, PNIPAM microgels cannot be colloidally stable. Polymer cross-linking uses covalent bonds between PNIPAM strands using reagents such as Methylene Bis Acrylamide (MBA). Chemical cross-linking is a non-equilibrium process in which MBA is consumed before NIPAM monomers. Therefore, PNIPAM microgels do not have a uniform composition, leading particles with a non-constant density cross-links profile. [19–21]

In the Stieger *et. al.* work, [22] is reported a study of the structural properties of PNIPAM using the Small-Angle Neutron Scattering (SANS) technique. They found that the PNIPAM microgel structure can be described with an inner constant dense region, also known as the core, and a fuzzy shell, where the density decreases approximately as a Gaussian function. This model is known as the fuzzy sphere model. Currently, this is the benchmark picture of the standard microgel particles. [21, 22] The fuzzy model used to describe the neutron scattering intensity data, where the form factor is estimated as the convolution of the sphere scattering form factor with a Gaussian decay function, is similar, under some approximations, to the Rayleigh-Gans-Debye (RGD) approximation for light scattering. Therefore, under RGD approximation, the form factor function for a fuzzy sphere particle can be written as: [18, 22]

$$F_{fs}(q) = 3\frac{\sin(qR) - qR\cos(qR)}{qR^3}\ \exp\left[-\frac{(\sigma q)^2}{2}\right]. \tag{1.1}$$

Here, R is the core radius, q is the magnitude of the scattering number, and the Gaussian width σ measures the width of the smeared particle surface. [18, 22]

When microgels like PNIPAM are studied with light scattering techniques, the RGD approximation for a fuzzy sphere is usually used to describe the light scattering intensity data as a function of scattering angle. [18,23–25] A key aspect observed in this context is that, despite the Mie scattering solution being the exact treatment for light scattering by spherical particles, the RGD approxi-

mation has been predominantly used in the literature, even in cases where this approximation is invalid. [18, 24–26] One of the main arguments for using the RGD approximation in light scattering experiments despite the microgel particles do not meet the RGD validity conditions is that calculation of the form factor using the Mie scattering solution is impractical. [24] However, in this dissertation, we demonstrate that the main obstacle to the widespread application of Mie scattering solutions is not its complexity but rather the lack of knowledge regarding the dielectric properties of spherical particles, particularly PNIPAM-based colloidal particles. While the RGD approximation circumvents this issue, it also limits the ability to make accurate predictions about their optical behavior.

To address this problem, this dissertation first reviews the Mie scattering solution for homogeneous and multilayered spheres in Chapter 2 and provides computational algorithms for applying these solutions to spherically symmetric particles. Additionally, it discusses the problem of the size particle polydispersity and how it must be accounted for to accurately describe the scattering properties of colloidal suspension. Chapter 3 reviews the light scattering experimental techniques used in this dissertation: Static Light Scattering (SLS) and Dynamic Light Scattering (DLS). In Chapter 4, we successfully implement the Mie scattering solution for multilayered spheres to describe light scattering properties of PNIPAM particles, incorporating a Refractive Index (RI) profile model based on the Gaussian model of the PNIPAM cross-link density profile. We validate this approach using static light scattering data reported in Ref. [18]. Chapter 5 presents the synthesis and characterization of our PolyStyrene/PNIPAM (PS/PNIPAM) core/shell particles and the application of the Mie scattering solution to describe their scattering properties. Finally, Chapter 5.4 explores the descriptive capability of the RI profile model in describing PS/PNIPAM-co-AcrylicACid (PNIPAM-co-AAc) core/shell particles, which differ in their cross-linking structure from conventional PNIPAM microgels. We use static light scattering data reported in Ref. [15]. The conclusions of this dissertation are presented in Chapter 6, and future research directions stemming from this work are briefly outlined in Chapter 7.

Chapter 2

Theoretical Framework

The phenomenon of light scattering is related to the heterogeneities of the medium through which a light beam is propagated. Consider, for example, a light beam that propagates through a continuous medium that contains some heterogeneities with bulk properties different from those of the surrounding medium. When the light beam hits the heterogeneities, the electromagnetic fields of the beam and the heterogeneities' electric charges interact, emitting electromagnetic energy in all directions, known as secondary radiation or light scattering. [27, 28]

The scattering of light depends on the shape and size of the heterogeneities, as well as on the contrast between their dielectric properties and those of the surrounding medium. Consequently, the measurement of the scattered light intensity, I_s, can provide information about the heterogeneities embedded within the medium. This is the underlying principle of all wave scattering experiments, where, in general, the scattered intensity is measured in different directions with respect to the incident wavefront and at various distances from the scattering volume, which can be in the near field or the far field. The resulting data, recorded as a function of orientation and position, are then analyzed using the most appropriate theoretical framework [27, 29].

In particular, the static light scattering technique measures the scattering of light by particles suspended in a liquid medium, with the scattered intensity recorded in the far-field region as a function of the scattering angle, θ, typically ranging from 0° to 180°. Classical electromagnetic theory provides a suitable theoretical framework for data analysis, and its review is the subject of this chapter. Details of the experimental technique are presented in Chapter 3.

Throughout the history of electromagnetic theory, two main approaches to light scattering have been developed: The Raleigh-Gans-Debye approximation (RGD) and the Mie Scattering solution. [27] In both approaches, the most straightforward case consists of studying the scattering of monochromatic plane waves by homogeneous spherical heterogeneities (which, from now on, will be named in this thesis as particles), with linear dielectric properties embedded in a surrounding medium with linear dielectric properties and without free charges (named in this thesis as solvent).

Both approaches can be extended to more complicated cases, such as radially non-homogeneous spherical particles. [27]

The two approaches differ in the following: RGD could describe light scattering only by tiny particles compared to the light's wavelength or particles whose refractive index almost matches that of the surrounding medium. From an experimental point of view, these conditions are very restrictive, but RGD can be used for particles of almost any geometrical shape. Instead, the Mie Scattering solution is an exact solution of Maxwell's electromagnetic equations for a plane monochromatic wave scattered by spherical particles of any size. Still, the analytical solution involves series and special functions that sometimes are awkward for numerical calculation. This limitation is, in many cases, the experimentalists' principal reason to use RGD instead of Mie solution, even for particles that do not fully meet the RGD conditions, preferring to deal with the errors of the RGD approximation rather than with cumbersome calculations of the Mie solution. [24, 26, 27, 30]

One of the principal goals of this thesis is to show how to apply the Mie scattering solution to nonhomogeneous colloidal particles with spherical symmetry. In this chapter, as a starting point, we will review the Mie scattering solution and the RGD approximation of the light scattering for a homogeneous sphere. Then, we explore the generalization of the Mie scattering solution for a non-homogeneous multilayer sphere. Finally, we study the effect of polydispersity in particle size on the scattered light intensity as a function of scattering angle. All the review done in this chapter follows the theoretical development and notation of Bohren and Huffman's book, [27], so in the following, reference [27] will be omitted.

2.1 Scattering by Homogeneous Sphere

2.1.1 Mie Scattering Solution

As previously mentioned, the Mie Scattering Solution for light scattering by homogeneous spheres is an exact solution of Maxwell's electromagnetic (EM) equations for a monochromatic plane wave propagating through a solvent with linear properties without free charges and scattered by particles with linear properties.

For this case, the EM fields for a plane monochromatic wave are given by the following harmonics equations:

$$\mathbf{E}_i = \mathbf{E}_0 \exp(i\mathbf{k}\cdot\mathbf{x} - i\omega t), \quad \mathbf{H}_i = \mathbf{H}_0 \exp(i\mathbf{k}\cdot\mathbf{x} - i\omega t), \tag{2.1}$$

where $\mathbf{k}$ is the wave vector that specifies the propagation direction of the wave, the wave vector magnitude, also known as wavenumber, k, is related to wavelength, λ, as $k = 2\pi n_0/\lambda$, with n_0 the solvent refractive index, and with the angular frequency, ω, as $k = \omega/v$, with v the light speed in

the solvent. The solvent and the scatterer particle have the constitutive relations given by:

$$\mathbf{B} = \mu\mathbf{H}, \quad \mathbf{P} = \varepsilon\mathbf{E}, \tag{2.2}$$

$$\mathbf{J}_f = \sigma\mathbf{E}, \quad \mathbf{B}_1 = \mu_1\mathbf{H}, \quad \mathbf{P}_1 = \varepsilon_1\mathbf{E}, \tag{2.3}$$

where μ and μ_1, ε and ε_1 are the solvent and particle's magnetic permeability and electric susceptibility, respectively, and σ is the conductivity of the sphere.

For the harmonics fields of Eq. (2.1) that propagate through a solvent with the constitutive relations of Eq. (2.2), the Maxwell's equations are:

$$\begin{aligned} \nabla \cdot \mathbf{E} = 0, \quad & \nabla \cdot \mathbf{B} = 0, \\ \nabla \times \mathbf{E} = i\omega\mu\mathbf{H}, \quad & \nabla \times \mathbf{H} = -i\omega\varepsilon\mathbf{E} \end{aligned} \tag{2.4}$$

For the continuity of the EM fields through the particle interface with the solvent, it is enough that the boundary condition for the tangential components of the fields is fulfilled, which is:

$$(\mathbf{E}_i + \mathbf{E}_s - \mathbf{E}_1) \times \hat{\mathbf{e}}_r = 0, \quad (\mathbf{H}_i + \mathbf{H}_s - \mathbf{H}_1) \times \hat{\mathbf{e}}_r = 0, \tag{2.5}$$

where subscript i, s, and 1 are for the incident, scattered EM fields, and the EM field inside the sphere, respectively. From now on, we will describe the wavefront from its electric field, $\mathbf{E}$. The magnetic field, $\mathbf{H}$, can be easily calculated with the relations of Eq. (2.4).

For particles with linear properties, and in the absence of absorption resonances, we can assert that the light scattering by the particle is elastic, where the wavenumber of the incident and scattered wavefront is the same: $|\mathbf{k}|_i = |\mathbf{k}|_s = k_0$.

In this dissertation, we use the Mie scattering solution to describe the scattered electromagnetic (EM) fields in the far-field region. In this regime, the observation distance, r, is much greater than the characteristic size of the scattering object, and the source of the scattered light can be considered to lie at the origin. Under these conditions, the scattered wavefront can be approximated as a transverse spherical wavefront, whose asymptotic form is given by:

$$\mathbf{E}_s \sim \frac{e^{ikr}}{-ikr}\mathbf{A}, \quad kr \gg 1. \tag{2.6}$$

where $\mathbf{A}$ is the scattering amplitude function.

With all the previous considerations, we can assert that the incident and scattered fields are directly related. Since the Mie scattering solution assumes plane wavefronts, it is convenient to describe this linear relationship in terms of the transverse components of the fields, defined by the parallel, $\hat{\mathbf{e}}_{||}$, and perpendicular, $\hat{\mathbf{e}}_{\perp}$, transverse unit vectors. In Figure 2.1, we show a schematic of a plane wavefront incident on a spherical particle. In the far-field region, the propagation directions

of the incident and scattered wavefronts define a scattering plane, within which the transverse components of both wavefronts must be linearly related. The transverse components of the incident plane wavefront propagating along the $\hat{\mathbf{e}}_z$ direction are:

$$E_{||i} = \cos\phi E_{xi} + \sin\phi E_{yi}, \quad E_{\perp i} = \sin\phi E_{xi} - \cos\phi E_{yi}, \tag{2.7}$$

where ϕ is the azimuthal angle. Also, E_{xi} and E_{yi} are the cartesian components of the incident electric field. The scattered electric field at the far-field region is:

$$\mathbf{E}_s = E_{||s}\hat{\mathbf{e}}_{||s} + E_{\perp s}\hat{\mathbf{e}}_{\perp s}, \tag{2.8}$$

where $\hat{\mathbf{e}}_{||s} = \hat{\mathbf{e}}_\theta$ and $\hat{\mathbf{e}}_{\perp s} = -\hat{\mathbf{e}}_\phi$. Observe that $\hat{\mathbf{e}}_{||s} \times \hat{\mathbf{e}}_{\perp s} = \hat{\mathbf{e}}_r$, where $\hat{\mathbf{e}}_r$, $\hat{\mathbf{e}}_\theta$, and $\hat{\mathbf{e}}_\phi$ are the spherical unitary vectors. The transverse components of the incident and scattered electric field are in different sets of basis. Then, from Eq. (2.6), the linear relationship between $\mathbf{E}_s$ and $\mathbf{E}_i$ can be written in matrix form as:

$$\begin{pmatrix} E_{||s} \\ E_{\perp s} \end{pmatrix} = \frac{\mathrm{e}^{ikr}}{-ikr} \begin{pmatrix} S_2 & S_3 \\ S_4 & S_1 \end{pmatrix} \begin{pmatrix} E_{||i} \\ E_{\perp i} \end{pmatrix}, \tag{2.9}$$

where S is the change of the basis matrix, known as the scattering amplitude matrix, and $[S]_j$ is the scattering amplitude coefficient. In the last equation, the scattering amplitude function of Eq. (2.6) is $\mathbf{A} = S\mathbf{E}_i$. In general $[S]_j$ depends on $\mathbf{k}$, the scattering angle, θ, and azimuthal angle, ϕ.

In the problem presented here, solving Maxwell's electromagnetic equations for a given incident EM field, particle size, and the dielectric properties of both the solvent and the particle allows us to determine the electromagnetic fields inside and outside the scattering particle, denoted by $\mathbf{E}_1$ and $\mathbf{H}_1$, and $\mathbf{E}_s$ and $\mathbf{H}_s$, respectively. The solution is expressed, in both regions, as a series expansion involving spherical Bessel and Hankel functions. Full details of the solution to Maxwell's electromagnetic equations for this problem can be found in the book by Bohren and Huffman [27]. After solving the equations, Eq. (2.9) reduces to:

$$\begin{pmatrix} E_{||s} \\ E_{\perp s} \end{pmatrix} = \frac{\mathrm{e}^{ikr}}{-ikr} \begin{pmatrix} S_2 & 0 \\ 0 & S_1 \end{pmatrix} \begin{pmatrix} E_{||i} \\ E_{\perp i} \end{pmatrix}, \tag{2.10}$$

where the coefficients S_1 and S_2 are:

$$\begin{aligned} S_1 &= \sum_n \frac{2n+1}{n(n+1)}(a_n\pi_n + b_n\tau_n), \\ S_2 &= \sum_n \frac{2n+1}{n(n+1)}(b_n\pi_n + a_n\tau_n). \end{aligned} \tag{2.11}$$

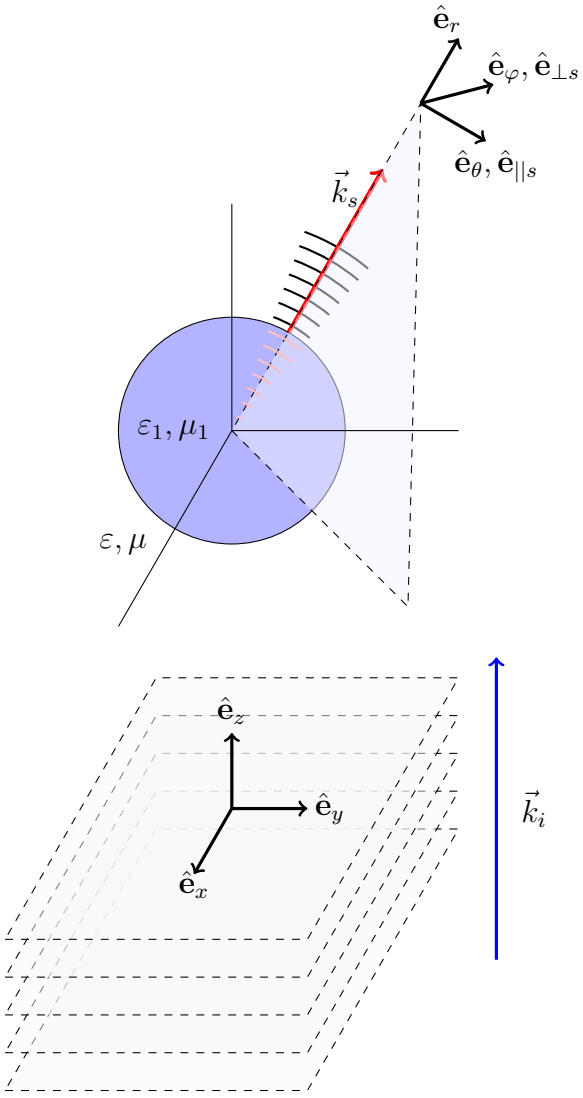

Figure 2.1: Sketch of a monochromatic plane wavefront elastically scattered by a spherical particle with linear properties. The incident wavefront propagates along the direction $\hat{\mathbf{e}}_z$. In the far-field region, the scattered wavefront is approximated as a transverse spherical wavefront, where the azimuthal and polar spherical unit vectors correspond to the perpendicular, $\hat{\mathbf{e}}_{\perp s}$, and parallel, $\hat{\mathbf{e}}_{||s}$, directions of the scattered wavefront. The scattering plane is defined by the incident wave vector, $\mathbf{k}_i$, and the scattering wave vector, $\mathbf{k}_s$. It is therefore possible to construct a change-of-basis matrix that relates the transverse components of the incident and scattered wavefronts.

Here, π_n y τ_n are the angular functions defined as:

$$\pi_n = \frac{P_n^1(\cos\theta)}{\sin\theta}, \quad \tau_n = \frac{dP_n^1(\cos\theta)}{d\theta}, \tag{2.12}$$

where P_n^1 is the associated Legendre function of degree 1. Also, the coefficients a_n and b_n are defined by:

$$a_n = \frac{m\psi_n(mx)\psi_n'(x) - \psi_n(x)\psi_n'(mx)}{m\psi_n(mx)\xi_n'(x) - \xi_n(x)\psi_n'(mx)}, \quad b_n = \frac{\psi_n(mx)\psi_n'(x) - m\psi_n(x)\psi_n'(mx)}{\psi_n(mx)\xi_n'(x) - m\xi_n(x)\psi_n'(mx)}, \tag{2.13}$$

and they are determined by boundary conditions. In the last equation, m is the relative refractive index defined as $m = n_p/n_0$, where n_p and n_0 is the particle and surrounding medium's refractive index, respectively, and x is the size parameter defined by $x = 2\pi n_0 R_p/\lambda$, where R_p is the particle's radius. Also, in Eq. (2.13), the special functions $\psi_n(\eta)$ and $\xi_n(\eta)$ are the Riccati-Bessel functions defined as $\psi_n(\eta) = \eta j_n(\eta)$ and $\xi_n(\eta) = \eta h_n^{(1)}(\eta)$, where $j_n(\eta)$ and $h_n^{(1)}(\eta)$ are the spherical Bessel function of the first kind and the Hankel function of the first kind, with η the function's argument. Observe that the scattering amplitude coefficients, S_1 and S_2, are only a function of scattering angle θ. It is essential to mention that the solvent and particle's magnetic permeability, μ and μ_1, have been considered the same.

Now, it is possible to quantify the light scattered intensity that we can measure in some direction at the far-field region. To do that, we introduce the differential scattering cross-section, $dC_{sca}/d\Omega$, defined as the average scattered energy per unit of solid angle, normalized by the incident light intensity, that is: [27, 28]

$$\frac{dC_{sca}}{d\Omega} = \lim_{r\to\infty} \frac{r^2\hat{\mathbf{r}}\cdot\langle\mathbf{S}_s\rangle}{|\langle\mathbf{S}_i\rangle|}. \tag{2.14}$$

Here, $\langle\mathbf{S}\rangle = \mathrm{Re}(\mathbf{E}\times\mathbf{H}^*)/2$ is the average of the Poynting vector, whose modulus gives the incident and scattered light intensity, and the average in the angular parenthesis, $\langle\cdots\rangle$, are over measurement time. From Eq. (2.6), the Eq. (2.14) could be written as:

$$\frac{dC_{sca}}{d\Omega} = \frac{1}{k_0^2}\frac{|\hat{\varepsilon}_{||,\perp}\cdot\mathbf{A}|^2}{|\mathbf{E}_i|^2}, \tag{2.15}$$

where $\hat{\varepsilon}_{||,\perp}$ are the polarization components of light scattered, and $|\hat{\varepsilon}_{||,\perp}\cdot\mathbf{A}|^2$ is the general expression for the *form factor function*. The form factor function gives the angular distribution of the scattered light. In our case, using Eq. (2.10), the form factor function for incident unpolarized light is:

$$F(\theta) = \frac{1}{2}\left(|S_1|^2 + |S_2|^2\right), \tag{2.16}$$

and the scattering cross section is:

$$C_{sca} = \frac{1}{k_0^2} \int_{\Omega} F(\theta) d\Omega. \tag{2.17}$$

Finally, the total scattered intensity measured at some scattering angle θ is proportional to the total number of particles, N, in the scattering volume defined by the beam light's spot size and the detector's solid angle. Then, for unpolarized light, the total scattered intensity as a function of scattering angle θ is:

$$I_T(\theta) \propto N I_s(\theta) = N F(\theta). \tag{2.18}$$

If the beam light is polarized, the total intensity is:

$$I_{T,\perp}(\theta) \propto N|S_1(\theta)|^2, \quad I_{T,||}(\theta) \propto N|S_2(\theta)|^2, \tag{2.19}$$

for vertical and parallel polarization, $\hat{\varepsilon}_\perp$ and $\hat{\varepsilon}_{||}$, respectively. In the last equations, we consider that the particles are monodisperse in size, *i. e.*, all the particles have the same size. The general case for a polydisperse system will be reviewed in the section 2.3.2.

2.1.2 Computational aspects of the Mie scattering solution

For numerical calculation of the amplitude scattering coefficients of Eq. (2.11), it is necessary to evaluate the special functions $\psi_n(\eta)$ and $\xi_n(\eta)$, and their derivatives for each n until the series in the Eq. (2.11) converge at some cut term, n_c. Historically, various algorithms for numerical calculation of the coefficients $S_1(\theta)$ and $S_2(\theta)$ have been proposed, and Bohren and Huffman's algorithm (BHMIE) is one of the most used to characterize the scattering properties of spherical colloidal particles. [2, 27, 31] In this work, we use the BHMIE algorithm to calculate the scattering properties, and its source code, written in Fortran 77, can be found in Appendix A of Bohren and Huffman's book. Also, we coded a BHMIE algorithm version in Fortran 2008, available as open source code in GitHub (`https://github.com/Complex-Fluids-IFUNAM/Mie-Scattering`).

The BHMIE algorithm uses the empirical Wiscombe's cutoff criterion for the series computation in Eq. (2.11), where the least first series terms to calculate, n_{stop}, after the convergence is reached are defined by: [32]

$$n_{\text{stop}} = \lceil x + 4x^{1/3} + 2 \rceil. \tag{2.20}$$

Here, the parenthesis $\lceil \cdots \rceil$ denotes the ceiling function and gives the least integer greater than the function argument, and $x = k_0 R_p$ is the size parameter.

Due to well-established recurrence relations for the special functions involved in Mie scattering solution, [27,33] it seems that the calculation of angular functions, $\pi_n(\theta)$ and $\tau_n(\theta)$ in Eq. (2.11), and

the Ricatti-Bessel functions in Eq. (2.13), is straightforward. Indeed, this is true for the numerical calculation of $\pi_n(\theta)$ and $\tau_n(\theta)$, where the recurrence relations are followed from the associated Legendre function of degree 1, and can be computed by upward recurrence from the following relations:

$$\begin{aligned}\pi_n(\theta) &= \frac{2n-1}{n-1}\pi_{n-1}(\theta)\cos\theta - \frac{n}{n-1}\pi_{n-2}(\theta),\\ \tau_n(\theta) &= n\pi_n(\theta)\cos\theta - (n+1)\pi_{n-1}(\theta).\end{aligned} \tag{2.21}$$

Here, the recurrence beginning with $\pi_0(\theta) = 0$ and $\pi_1(\theta) = 1$. On the other hand, the numerical calculation of coefficients a_n and b_n cannot follow straightforwardly from recurrence relations of Riccati-Bessel functions. If we calculate the coefficients a_n and b_n as defined in Eq. (2.13), the roundoff numerical errors in the coefficients grow alarmingly with n. To avoid this, the BHMIE algorithm rewrites the coefficients of Eq. (2.13), just for numerical calculations, in the following form:

$$\begin{aligned}a_n &= \frac{[D_n(mx)/m + n/x]\psi_n(x) - \psi_{n-1}(x)}{[D_n(mx)/m + n/x]\xi_n(x) - \xi_{n-1}(x)},\\ b_n &= \frac{[mD_n(mx) + n/x]\psi_n(x) - \psi_{n-1}(x)}{[mD_n(mx) + n/x]\xi_n(x) - \xi_{n-1}(x)},\end{aligned} \tag{2.22}$$

where $D_n(\eta) = \frac{d}{d\eta}\ln\psi_n(\eta)$, and to eliminate $\psi_n'(x)$ and $\xi_n'(x)$ in Eq. (2.13) its have used the recurrence relations:

$$\psi_n'(x) = \psi_{n-1}(x) - \frac{n\psi_n(x)}{x}, \quad \xi_n'(x) = \xi_{n-1}(x) - \frac{n\xi_n(x)}{x}. \tag{2.23}$$

The logarithmic derivative, $D_n(\eta)$, is calculated following a downward recurrence (lower orders are generated from higher orders), defined by:

$$D_{n-1}(\eta) = \frac{n}{\eta} - \frac{1}{D_n(\eta) + n/\eta}. \tag{2.24}$$

Notwhitstanding, the recurrence must beginning at $n_{\max}$ where $D_{n_{\max}} \approx 0$. The BHMIE algorithm choose $n_{\max}$ as:

$$n_{\max} = \max(n_{\text{stop}}, \lceil |mx| \rceil) + 15, \tag{2.25}$$

where the downward recurrence is begun with $D_{n_{\max}} = 0 + i0$. Finally, the Riccati-Bessel functions in Eq. (2.22) are computed by upward recurrence from the following relations:

$$\psi_{n+1}(x) = \frac{2n+1}{x}\psi_n(x) - \psi_{n-1}(x), \tag{2.26}$$

where $\psi_n(x)$ and $\xi_n(x)$ satisfy that $\xi_n(x) = \psi_n(x) + i\chi_n(x)$, and the recurrence begins with:

$$\psi_{-1}(x) = \cos x, \quad \psi_0(x) = \sin x,$$
$$\chi_{-1}(x) = -\sin x, \quad \chi_0(x) = \cos x.$$

In summary, for a given wavelength, λ, solvent's refractive index, n_0, particle's size and refractive index, R_p and n_p, where $n_p \in \mathbb{C}$, and the scattering angles θ_i, the BHMIE algorithm makes the following steps:

1. Calculates $x = 2\pi n_0 R_p/\lambda$ and $m = n_p/n_0$. Then, calculates n_{stop} using Eq. (2.20).

2. Calculates $n_{\max}$ using Eq. (2.25). Then, calculates $D_n(mx)$ for every n in $[0, n_{\max}]$ using the downward recurrence relation of Eq. (2.24). All $D_n(mx)$ values are reserved for those use.

3. Generates a table of scattering angles θ_i and starts the upward recurrences for angular functions with $\pi_0(\theta_i) = 0$ and $\pi_1(\theta_i) = 1$.

4. Starts the upward recurrences for Riccati-Bessel functions with $\psi_0(x) = (\cos x)$, $\psi_1(x) = (\sin x)$, $\chi_0(x) = -\sin x$ and $\chi_1(x) = \cos x$. Then, $\xi_n(x)$ is initialized with $\xi_1(x) = \psi_1(x) - i\chi_1(x)$.

5. Starting series iteration for $S_1(\theta_i)$ and $S_2(\theta_i)$ in Eq. (2.11), from $n = 1$ and to $n = n_{\text{stop}}$. In each iteration, the following steps are performed:

   (a) Angular functions $\pi_n(\theta_i)$ and $\tau_n(\theta_i)$ are computed for all scattering angles θ_i following the recurrence relations of Eq. (2.21).

   (b) Special functions $\psi_n(x)$ and $\xi_n(x)$ are evaluated using Eq. (2.26).

   (c) Coefficients a_n and b_n are evaluated following Eq. (2.22), using the corresponding values of $D_n(mx)$, previously calculated.

   (d) Computes next $n + 1$ term of all angular and Riccati-Bessel functions following the recurrence relations of Eqs. (2.21) and (2.26). Then, restart the loop unless $n + 1$ is greater than n_{stop}.

6. Calculates $|S_1(\theta_i)|^2$ and $|S_2(\theta_i)|^2$ and the form factor function $F(\theta_i)$ as defined in Eq. (2.16). Finally, the algorithm saves results files in a `.dat` format and stops the program.

2.1.3 Raleigh-Gans-Debye approximation

The Raleigh-Gans-Debye (RGD) approximation is another approach that describes light scattering by dielectric heterogeneities. Still, it's limited to tiny particles compared to the beam wave-

length and for particles suspended in a solvent whose refractive index almost matches the solvent one. Mathematically, these two conditions could be written as: [27, 29]

$$|m-1| \ll 1, \qquad kd|m-1| \ll 1 \tag{2.27}$$

where $m = n_p/n_0$ is the relative refractive index, $k = 2\pi n_0/\lambda$ is the wavenumber and d is the particle's characteristic linear dimension. The RGD validity conditions could be interpreted in the next way: the incident plane monochromatic wave is not appreciably reflected at the interface between particle and solvent, and the incident plane monochromatic wave does not undergo an appreciable phase change into the particle.

The RGD approximation estimates the field scattered by a particle, independently of its geometry, as the contribution of infinitesimal spherical volume elements. It can be shown that the contribution of a spherical volume element, Δv, to the field scattered by the particle is:

$$\begin{pmatrix} \Delta E_{||s} \\ \Delta E_{\perp s} \end{pmatrix} = \frac{\mathrm{e}^{ikr}}{-ikr} \Delta v \mathrm{e}^{i\delta} \begin{pmatrix} s_2 & 0 \\ 0 & s_1 \end{pmatrix} \begin{pmatrix} E_{||i} \\ E_{\perp i} \end{pmatrix}, \tag{2.28}$$

where $\delta = k\mathbf{R}\cdot(\hat{\mathbf{e}}_z - \hat{\mathbf{e}}_r)$ with $\hat{\mathbf{e}}_z$ and $\hat{\mathbf{e}}_r$ the propagation direction of the incident and scattered waves, respectively, and $\mathbf{R}$ is the vector that joins two volume elements into the particle that contributes to scattering wave. Also, in Eq. (2.28), s_1 and s_2 are the amplitude scattering coefficients per volume unit defined by:

$$\begin{aligned} s_1(\theta) &:= \lim_{x\to 0} \frac{S_1(\theta)}{v} = -\frac{ik^3}{2\pi}(m-1), \\ s_2(\theta) &:= \lim_{x\to 0} \frac{S_2(\theta)}{v} = -\frac{ik^3}{2\pi}(m-1)\cos\theta. \end{aligned} \tag{2.29}$$

Here, $v = 4/3\pi R_p^3$ and $S_1(\theta)$ and $S_2(\theta)$ are the scattering amplitude coefficient given in Eq. (2.11). The total electric field scattered is obtained by integrating Eq. (2.28) over the particle volume v. Then, the expression for $\mathbf{E}_s$ in Eq. (2.10) is recovery, redefined the amplitude scattering coefficients as follows:

$$\begin{aligned} S_1(\theta) &= -\frac{ik^3}{2\pi}(m-1)v f(\theta,\phi), \\ S_2(\theta) &= -\frac{ik^3}{2\pi}(m-1)v f(\theta,\phi)\cos\theta, \end{aligned} \tag{2.30}$$

where, in the RGD approximation context, $f(\theta, \phi)$ is the form factor function, defined by:

$$f(\theta, \phi) = \frac{1}{v} \int_v \mathrm{e}^{i\delta} dv. \tag{2.31}$$

Therefore, the RGD approximation can describe the light scattering for any particle whenever it is possible to determine a phase function δ, independently of its geometry.

Now, we define the scattering vector, $\mathbf{q}$, as $\mathbf{q} = \mathbf{k}_s - \mathbf{k}_i$. For elastic scattering, the magnitude of scattering vector, q, is related to the scattering angle, θ, as:

$$q = |\mathbf{k}_s - \mathbf{k}_i| = 2k \sin(\theta/2). \tag{2.32}$$

For spherical dielectric particles, the phase function is:

$$\delta = 2k \sin(\theta/2)\xi = q\xi, \tag{2.33}$$

where $\xi = \mathbf{R} \cdot (\hat{\mathbf{e}}_z - \hat{\mathbf{e}}_r)$. Then, the form factor can be calculated over ξ as:

$$f = \frac{1}{v} \int \mathrm{e}^{iq\xi} A(\xi) d\xi, \tag{2.34}$$

where $A(\xi)$ is the area defined by $\mathbf{R} \cdot (\hat{\mathbf{e}}_z - \hat{\mathbf{e}}_r) = R \cos(\mathbf{R}, \hat{\mathbf{e}}_z - \hat{\mathbf{e}}_r) = \pi(R_p^2 - \xi^2)$. After integrating Eq. (2.34), the form factor for a spherical particle in the RGD approximation is:

$$f(\theta) = \frac{3}{(qR_p)^3} [\sin(qR_p) - qR_p \cos(qR_p)]. \tag{2.35}$$

Finally, the scattered intensity as a function of the scattering angle can be estimated with the same relations introduced in Eqs. (2.18) and (2.19).

2.1.4 Mie solution vs RGD approximation

To discuss the differences between the Mie solution and the RGD approximation, let us consider two cases that can be measured in a light scattering experiment: silica colloidal spheres (SiO_2) suspended in decalin and polystyrene colloidal spheres (PS) suspended in water. Also, we consider that a red beam laser with $\lambda = 632.8$nm is used in both suspensions, and the light scattering experiment is carried out with vertical polarization. Then, the scattering intensity predicted by the Mie scattering solution and the RGD approximation is proportional to $|S_1(\theta)|^2$ (see Eq. (2.19)) and particularly, for RGD approximation, $|S_1(\theta)|^2 \propto f(\theta)^2$, with $f(\theta)$ given by Eq. (2.35). To quantify the differences between both predictions, we defined the quadratic difference between the normalized scattering intensity predicted by the Mie scattering solution and RGD approximation as

$\Delta^2_{Mie,RGD} = \sum_i [|S_1^{\text{Mie}}(\theta_i)|^2 - f(\theta_i)^4]$.

For the wavelength considered, the refractive index for SiO_2 is $n_{SiO_2} = 1.457$, while for decalin is $n_{\text{decalin}} = 1.47$. we use the refractive index for PS and SiO_2 reported by Bangs Laboratories Inc. (USA). [34] Therefore, in the first case, we have a suspension in which the particles and solvent are in an index-match regime with a relative refractive index of $m = 0.991$ and $|m - 1| = 0.009$. On the other hand, for the wavelength considered, the refractive index for PS is $n_{\text{PS}} = 1.59$, whereas for water, it is $n_{\text{W}} = 1.331$. Then, in the second case, we have a suspension where the particles and the solvent have a relative refractive index of $m = 1.195$ and $|m - 1| = 0.194$, and it's considered far from an index match regime.

In Fig. 2.2(a), we show $\Delta^2_{Mie,RGD}$ as a function of the size parameter $x = (2\pi n_0/\lambda)R$ for the cases described above. In both cases, $\Delta^2_{Mie,RGD}$ quickly increases with the size parameter x and stabilizes after reaching a maximum. For SiO_2 suspension (black solid line), the maximum difference is reached at $x = 2.014$, and for PS suspension (blue dot-dashed line) at $x = 1.865$. $\Delta^2_{Mie,RGD}$ is remarkably low for SiO_2 suspension compared to that of PS suspension, which is three orders of magnitude larger.

In Fig. 2.2(b) and (c), we show the scattering intensity as a function of the scattering angle for SiO_2 suspension at size parameter $x = 2.014$ and $x = 10$, respectively. We can observe that predictions made by the Mie solution and the RGD approximation are notably similar for both size parameters considered. Note that $x = R_p(2\pi n_0/\lambda) = 10$ corresponds to large particle sizes compared to the wavelength of the light beam, and the RGD approximation is invalid. In Fig. 2.2d and e, we show the scattering intensity as a function of the scattering angle for PS suspension at size parameters $x = 1.865$ and $x = 10$, respectively. We can observe that the RGD approximation prediction deviates from that of the Mie solution for both size parameters. For $x = 1.865$, the deviation is noticeable at large scattering angles. For $x = 10$, the deviation is noticeable in almost all scattering angles, where RGD approximation predicts fewer scattering minimum than the structure predicted by the Mie solution.

From the above analysis, we can conclude that the RGD approximation can be applied to suspensions in which the particles are index-matched with the solvent, even when the particle size exceeds the laser wavelength. In such cases, it is sufficient that the RGD condition $|m - 1| \ll 1$ is satisfied. However, if the particles are not index-matched with the solvent, both conditions of the RGD approximation (see Eq. (2.27)) must be fulfilled. In this context, the Mie solution provides the most robust framework for analyzing the scattering intensity of particles, as it imposes no restrictions on particle size or refractive index contrast in its formulation.

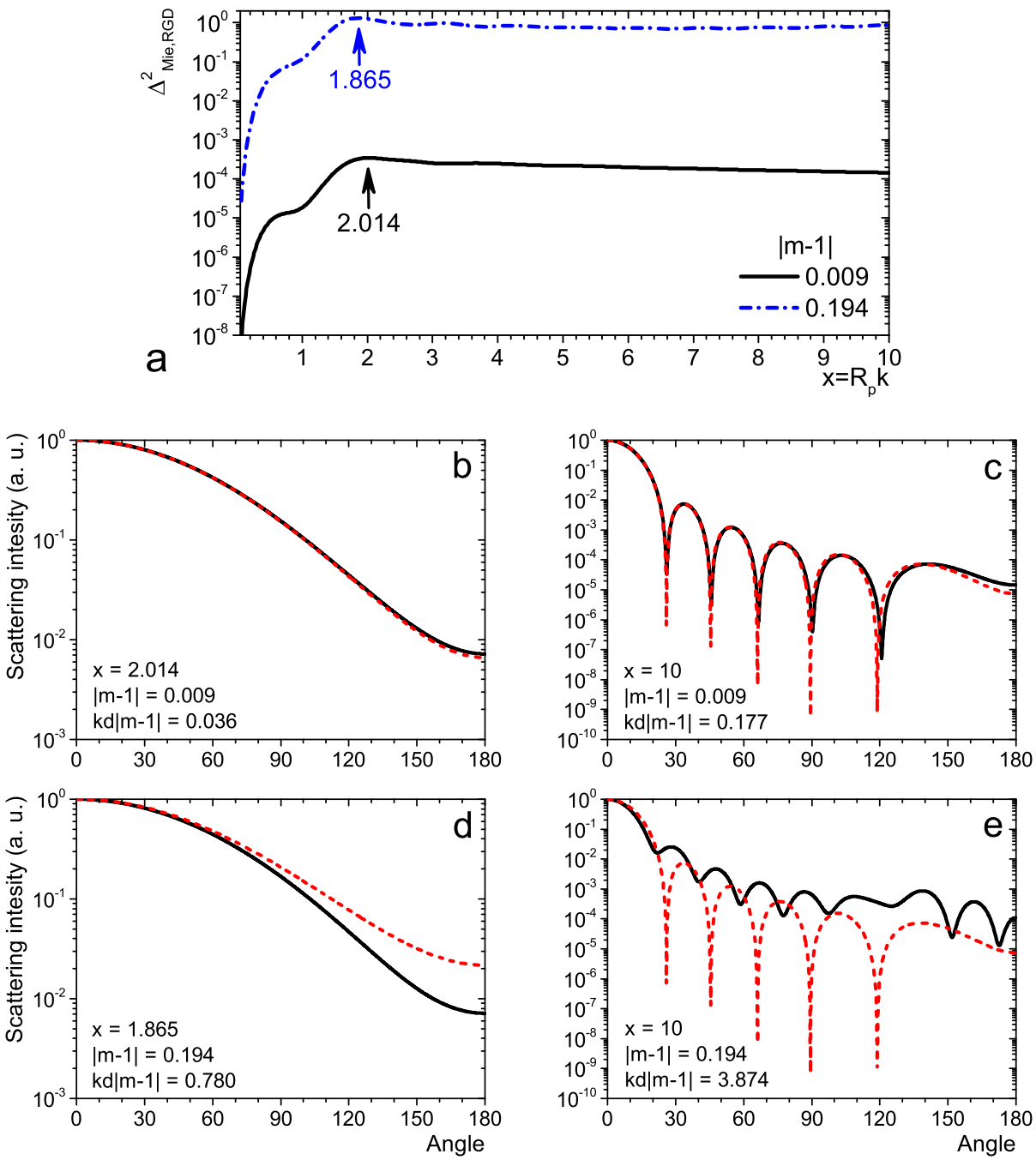

Figure 2.2: (a) $\Delta^2_{Mie,RGD}$ as a function of the size parameter x for silica SiO_2 particles suspended in decalin (red solid line) and PS particles suspended in water (blue dot-dashed line). (b) and (c): scattering intensity as a function of the scattering angle for SiO_2 in water suspension at $x = 2.014$ and $x = 10$, respectively. (d) and (e): scattering intensity as a function of the scattering angle for PS in water suspension at size parameter $x = 1.865$ and $x = 10$, respectively. In (b), (c), (d), and (e), the red dashed line gives the RGD approximation form factor, and the black solid line gives the Mie scattering solution form factor.

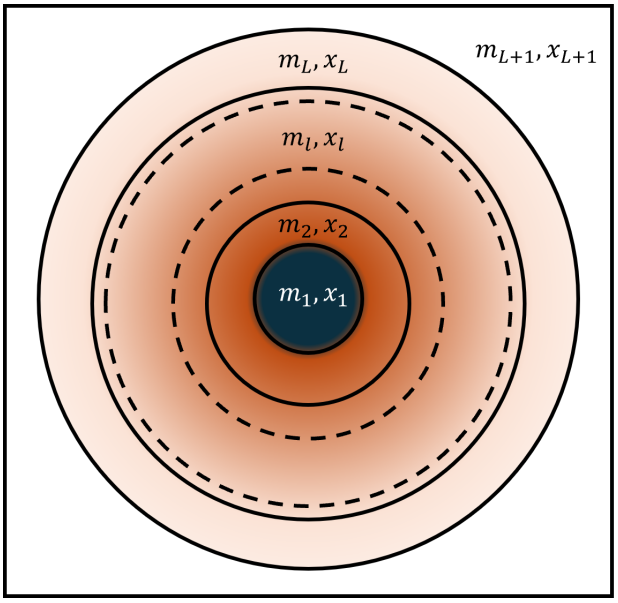

Figure 2.3: Sketch of the geometry of a multilayer sphere. The l layers are labeled from the inner, $l = 1$, to the outer, $l = L$. The solvent is labeled as the $L + 1$ layer. The intensity of color refers to the radial inhomogeneity of dielectric properties.

2.2 Mie Scattering Solution for a Multilayer Sphere

The scattering solution for a homogeneous sphere could be generalized for spheres made up of radial concentric layers, each layer with linear dielectric properties. This generalization is almost straightforward; all the conditions imposed for the Mie solution for a homogeneous sphere are used in the Mie solution for a multilayer sphere (see subsec. 2.1.1). The main difference lies in the fact that the boundary conditions for the continuity of EM fields apply at the interfaces between layers, as well as at the boundary of the outer layer with the solvent. Therefore, the functional form of the scattering amplitude coefficients, $S_1(\theta)$ and $S_2(\theta)$, and the form factor function, $F(\theta)$, are the same as in the Mie solution for a homogeneous sphere (see Eq. (2.11) and (2.16)), but the scattering coefficients a_n and b_n for scattered EM fields are determined by the propagation of EM fields through sphere's layers.

In Fig 2.3, we sketch a sphere stratified in L concentric layers, where two adjacent layers have different linear dielectric properties with spherical symmetry. The layers are labeled from the inner sphere or core with $l = 1$ to the outer layer with $l = L$ and surrounding media with $l = L + 1$. Because the layers have linear dielectric properties, the l layer can be characterized by its refractive index, n_l, so the l layer has a relative refractive index $m_l = n_l/n_{L+1}$, with n_{L+1} the solvent's refractive index. Each layer is characterized by the size parameter $x_l = 2\pi n_{L+1} r_l/\lambda = k r_l$

As in the Mie solution for a homogeneous sphere, we can calculate the EM fields by solving Maxwell's equations, and the solution is written using spherical Bessel's functions (see Appendix

A). In the Mie solution for a multilayer sphere, the EM fields in the core $\mathbf{E}_1$ and $\mathbf{H}_1$ are given by [27]

$$\begin{aligned}\mathbf{E}_1 &= \sum_{n=1}^{\infty} E_n \left(c_n^1 \mathbf{M}_{o1n}^{(j_n)} - i d_n^1 \mathbf{N}_{e1n}^{(j_n)} \right), \\ \mathbf{H}_1 &= -\frac{k_1}{\omega \mu_1} \sum_{n=1}^{\infty} E_n \left(d_n^1 \mathbf{M}_{e1n}^{(j_n)} + i c_n^1 \mathbf{N}_{o1n}^{(j_n)} \right)\end{aligned} \tag{2.36}$$

and the scattered EM fields $\mathbf{E}_s$ and $\mathbf{H}_s$ are given by

$$\begin{aligned}\mathbf{E}_s &= \sum_{n=1}^{\infty} E_n \left(i a_n^{L+1} \mathbf{N}_{e1n}^{(h_n^{(1)})} - b_n^{L+1} \mathbf{M}_{o1n}^{(h_n^{(1)})} \right), \\ \mathbf{H}_s &= -\frac{k}{\omega \mu} \sum_{n=1}^{\infty} E_n \left(-i b_n^{L+1} \mathbf{N}_{o1n}^{(h_n^{(1)})} - a_n^{L+1} \mathbf{M}_{e1n}^{(h_n^{(1)})} \right).\end{aligned} \tag{2.37}$$

In the last four equations $E_n = i^n E_0 (2n+1)/n(n+1)$, $\mathbf{M}_{e1n}^{(z_n)}$, $\mathbf{M}_{o1n}^{(z_n)}$, $\mathbf{N}_{e1n}^{(z_n)}$ and $\mathbf{N}_{e1n}^{(z_n)}$ are the vector harmonic functions given in Eq. (A.1) (see Appendix A). The superscript z_n in the vector harmonic functions denotes the radial dependence determined by the spherical Bessel functions, $j_n(\rho_l)$ and $y_n(\rho_l)$, or by the first kind of the spherical Hankel function, $h_n^{(1)}(\rho_l)$, where $\rho_l = k_l r$.

Note that in Eq. (2.36) and (2.37) only $j_n(\rho_l)$ and $h_n^{(1)}(\rho_l)$ is used, this is due to the need of the convergence of the EM fields in the core and at the far field region. On the other hand, in the intermediate layers, both spherical functions $j_n(\rho_l)$ and $y_n(\rho_l)$ are finite, and it's not necessary to use $h_n^{(1)}(\rho_l)$ because the regions are bounded. Therefore, the EM fields for the layer $l = 2, \cdots, L$ is given by

$$\begin{aligned}\mathbf{E}_l &= \sum_{n=1}^{\infty} E_n [f_n^{(l)} \mathbf{M}_{o1n}^{(j_n)} - i g_n^{(l)} \mathbf{N}_{e1n}^{(j_n)} + v_n^{(l)} \mathbf{M}_{o1n}^{(y_n)} - i w_n^{(l)} \mathbf{N}_{e1n}^{(y_n)}], \\ \mathbf{H}_l &= -\frac{k_l}{\omega \mu_l} \sum_{n=1}^{\infty} E_n [g_n^{(l)} \mathbf{M}_{e1n}^{(j_n)} + i f_n^{(l)} \mathbf{N}_{o1n}^{(j_n)} + w_n^{(l)} \mathbf{M}_{e1n}^{(y_n)} + i v_n^{(l)} \mathbf{N}_{o1n}^{(y_n)}].\end{aligned} \tag{2.38}$$

The boundary conditions for different interfaces are given by

$$(\mathbf{E}_{l+1} - \mathbf{E}_l) \times \hat{\mathbf{e}}_r = 0, \quad (\mathbf{H}_{l+1} - \mathbf{H}_l) \times \hat{\mathbf{e}}_r = 0, \quad \text{at } r = r_l, \tag{2.39}$$

where $l = 1, 2, \cdots, L$. Finally, all scattering coefficients in Eqs. (2.36), (2.37) and (2.38) can be evaluated using Eq. (2.39).

Equations (2.36), (2.37), and (2.38) represent the general solution for light scattering by a multi-layered sphere, first derived by Aden and Kerker [27,35,36]. As in the Mie solution for a homogeneous sphere, it is commonly assumed that the magnetic permeability of the solvent, μ, is approximately equal to that of all the sphere's layers, i.e., $\mu_1 \approx \cdots \approx \mu_L \approx \mu_{L+1} = \mu$. Under this assumption, the calculation of the scattering coefficients in Eqs. (2.36), (2.37), and (2.38) is simplified. However,

this restricts the applicability of the solution to systems in which the permeabilities of the materials involved are indeed approximately equal to that of the solvent.

Despite this simplification, the number of scattering coefficients increases significantly with the number of layers composing the sphere. For an L-layered sphere, the boundary conditions yield a system of $2L$ linear equations for $2L$ unknown coefficients. This system can, in principle, be solved using matrix methods. Nevertheless, as the number of layers increases, matrix-based computation becomes prone to round-off error propagation, which leads to numerical inaccuracies in the results. Additionally, the computational time scales as L^3 [36, 37]. To address this, various recursive algorithms have been proposed to compute the scattering coefficients more efficiently, reducing the computational time to scale linearly with L. However, many of these approaches still suffer from unresolved round-off error issues [31, 37, 38].

Yang developed one of the most stable recursive algorithms to calculate the scattering coefficients, where the numerical round-off errors issues are solved by the use of the first kind of the spherical Hankel function, $h_n^{(1)}(\rho_l)$, instead of the second kind of the Bessel function (see. Eq. (2.38)). [38] $h_n^{(1)}(\rho_l)$ is a linear combination of $j_n(\rho_l)$ and $y_n(\rho_l)$ defined as $h_n^{(1)}(\rho_l) = j_n(\rho_l) + iy_n(\rho_l)$, therefore, replacing $y_n(\rho_l)$ by $h_n^{(1)}(\rho_l)$ in Eq. (2.38), it can be obtained a general expression for the EM fields in any stratified sphere's layer, and is given by:

$$\begin{aligned}
\mathbf{E}_l &= \sum_{n=1}^{\infty} E_n[c_n^{(l)}\mathbf{M}_{o1n}^{(j_n)} - id_n^{(l)}\mathbf{N}_{e1n}^{(j_n)} + ia_n^{(l)}\mathbf{N}_{e1n}^{(h_n^{(1)})} - b_n^{(l)}\mathbf{M}_{o1n}^{(h_n^{(1)})}], \\
\mathbf{H}_l &= -\frac{k_l}{\omega\mu}\sum_{n=1}^{\infty} E_n[d_n^{(l)}\mathbf{M}_{e1n}^{(j_n)} + ic_n^{(l)}\mathbf{N}_{o1n}^{(j_n)} - ib_n^{(l)}\mathbf{N}_{o1n}^{(h_n^{(1)})} - a_n^{(l)}\mathbf{M}_{e1n}^{(h_n^{(1)})}],
\end{aligned} \tag{2.40}$$

with $l = 1, \cdots, L+1$. To recover EM fields of the sphere's core, given in Eq. (2.36), the scattering coefficients $a_n^{(1)} = b_n^{(1)} = 0$, and they are, indeed, the only two known scattering coefficients of the problem.

Using the boundary conditions in Eq. (2.39) with Eq. (2.40), the following set of linear equations for the adjacent layers, labeled with l and $l+1$, is obtained:

$$d_n^{(l+1)}m_l\psi_n'(m_{l+1}x_l) - a_n^{(l+1)}m_l\zeta_n'(m_{l+1}x_l) - d_n^{(l)}m_{l+1}\psi_n'(m_lx_l) + a_n^{(l)}m_{l+1}\zeta_n'(m_lx_l) = 0, \tag{2.41}$$

$$d_n^{(l+1)}\psi_n(m_{l+1}x_l) - a_n^{(l+1)}\zeta_n(m_{l+1}x_l) - d_n^{(l)}\psi_n(m_lx_l) + a_n^{(l)}\zeta_n(m_lx_l) = 0, \tag{2.42}$$

$$c_n^{(l+1)}m_l\psi_n(m_{l+1}x_l) - b_n^{(l+1)}m_l\zeta_n(m_{l+1}x_l) - c_n^{(l)}m_{l+1}\psi_n(m_lx_l) + b_n^{(l)}m_{l+1}\zeta_n(m_lx_l) = 0, \tag{2.43}$$

$$c_n^{(l+1)}\psi_n'(m_{l+1}x_l) - b_n^{(l+1)}\zeta_n'(m_{l+1}x_l) - c_n^{(l)}\psi_n'(m_lx_l) + b_n^{(l)}\zeta_n'(m_lx_l) = 0. \tag{2.44}$$

Here, $\psi_n(z)$ and $\zeta_n(z)$ are the Riccati-Bessel functions for the first kind of spherical Bessel function and the first kind of Hankel function, defined by $psi_n(z) = zj_n(z)$ and $\zeta_n(z) = zh_n^{(1)}(z)$, respectively. Using Cramer's rule to calculate $a_n^{(l+1)}$ and $d_n^{(l+1)}$ from Eq. (2.41) and (2.42), and to calculate $b_n^{(l+1}$

and $c_n^{(l+1)}$ from Eq. (2.43) and (2.44), the following set of equations is obtained:

$$a_n^{(l+1)} = \frac{\left\{\begin{array}{l} m_l\psi_n'(m_{l+1}x_l)[d_n^{(l)}\psi_n(m_lx_l) - a_n^{(l)}\zeta_n(m_lx_l)] \\ \quad - \psi_n(m_{l+1}x_l)[d_n^{(l)}m_{l+1}\psi_n'(m_lx_l) - a_n^{(l)}m_{l+1}\zeta_n'(m_lx_l)] \end{array}\right\}}{m_l\zeta_n'(m_{l+1}x_l)\psi_n(m_{l+1}x_l) - m_l\psi_n'(m_{l+1}x_l)\zeta_n(m_{l+1}x_l)}, \tag{2.45}$$

$$d_n^{(l+1)} = \frac{\left\{\begin{array}{l} m_l\zeta_n'(m_{l+1}x_l)[d_n^{(l)}\psi_n(m_lx_l) - a_n^{(l)}\zeta_n(m_lx_l)] \\ \quad - \zeta_n(m_{l+1}x_l)[d_n^{(l)}m_{l+1}\psi_n'(m_lx_l) - a_n^{(l)}m_{l+1}\zeta_n'(m_lx_l)] \end{array}\right\}}{m_l\zeta_n'(m_{l+1}x_l)\psi_n(m_{l+1}x_l) - m_l\psi_n'(m_{l+1}x_l)\zeta_n(m_{l+1}x_l)}. \tag{2.46}$$

$$b_n^{(l+1)} = \frac{\left\{\begin{array}{l} m_l\psi_n(m_{l+1}x_l)[c_n^{(l)}\psi_n'(m_lx_l) - b_n^{(l)}\zeta_n'(m_lx_l)] \\ \quad - \psi_n'(m_{l+1}x_l)[c_n^{(l)}m_{l+1}\psi_n(m_lx_l) - b_n^{(l)}m_{l+1}\zeta_n(m_lx_l)] \end{array}\right\}}{m_l\zeta_n(m_{l+1}x_l)\psi_n'(m_{l+1}x_l) - m_l\psi_n(m_{l+1}x_l)\zeta_n'(m_{l+1}x_l)}. \tag{2.47}$$

$$c_n^{(l+1)} = \frac{\left\{\begin{array}{l} m_l\zeta_n(m_{l+1}x_l)[c_n^{(l)}\psi_n'(m_lx_l) - b_n^{(l)}\zeta_n'(m_lx_l)] \\ \quad - \zeta_n'(m_{l+1}x_l)[c_n^{(l)}m_{l+1}\psi_n(m_lx_l) - b_n^{(l)}m_{l+1}\zeta_n(m_lx_l)] \end{array}\right\}}{m_l\zeta_n(m_{l+1}x_l)\psi_n'(m_{l+1}x_l) - m_l\psi_n(m_{l+1}x_l)\zeta_n'(m_{l+1}x_l)}. \tag{2.48}$$

Note that there are eight coefficients to calculate, but we have a set of four equations. To have a complete set of equations, it's necessary to use the boundary conditions for the continuity of normal components of EM fields across layer interfaces. It's important to remember that our goal is to determine the coefficients for scattered EM fields in Eq. (2.37). In this way, Yang avoided increasing the number of equations to be solved by introducing the reduced coefficients, $A_n^{(l)}$ and $B_n^{(l)}$, defined as $A_n^{(l)} = a_n^{(l)}/d_n^{(l)}$ and $B_n^{(l)} = b_n^{(l)}/c_n^{(l)}$. [38] Therefore, making Eq. (2.45) over Eq. (2.46) and Eq. (2.47) over Eq. (2.48), we obtain a set of two equations to solve given by

$$A_n^{(l+1)} = \frac{a_n^{(l+1)}}{d_n^{(l+1)}} = \frac{\psi_n(m_{l+1}x_l)}{\zeta_n(m_{l+1}x_l)} \frac{\left\{\begin{array}{l} m_{l+1}[\psi_n'(m_lx_l) - A_n^{(l)}\zeta_n'(m_lx_l)] \\ \quad - m_l\frac{\psi_n'(m_{l+1}x_l}{\psi_n(m_{l+1}x_l)}[\psi_n(m_lx_l) - A_n^{(l)}\zeta_n(m_lx_l)] \end{array}\right\}}{\left\{\begin{array}{l} m_{l+1}[\psi_n'(m_lx_l) - A_n^{(l)}\zeta_n'(m_lx_l)] \\ \quad - m_l\frac{\zeta_n'(m_{l+1}x_l}{\zeta_n(m_{l+1}x_l)}[\psi_n(m_lx_l) - A_n^{(l)}\zeta_n(m_lx_l)] \end{array}\right\}}, \tag{2.49}$$

$$B_n^{(l+1)} = \frac{b_n^{(l+1)}}{c_n^{(l+1)}} = \frac{\psi_n(m_{l+1}x_l)}{\zeta_n(m_{l+1}x_l)} \frac{\left\{\begin{array}{l} m_l[\psi_n'(m_lx_l) - B_n^{(l)}\zeta_n'(m_lx_l)] \\ \quad - m_{l+1}\frac{\psi_n'(m_{l+1}x_l}{\psi_n(m_{l+1}x_l)}[\psi_n(m_lx_l) - B_n^{(l)}\zeta_n(m_lx_l)] \end{array}\right\}}{\left\{\begin{array}{l} m_l[\psi_n'(m_lx_l) - B_n^{(l)}\zeta_n'(m_lx_l)] \\ \quad - m_{l+1}\frac{\zeta_n'(m_{l+1}x_l}{\zeta_n(m_{l+1}x_l)}[\psi_n(m_lx_l) - B_n^{(l)}\zeta_n(m_lx_l)] \end{array}\right\}}. \tag{2.50}$$

Hence, the reduced coefficients $A_n^{(l+1)}$ and $B_n^{(l+1)}$ can be calculated recursively, provided that $A_n^{(l)}$ and $B_n^{(l)}$ are known. Yang takes advantage of the fact that the reduced coefficients are known for the sphere's core, where $A_n^{(1)} = B_n^{(1)} = 0$ because $a_n^{(1)} = b_n^{(1)} = 0$. Therefore, a recursive algorithm

that uses Eq. (2.49) and (2.50) can start at the core. For the EM fields that propagate in the solvent, labeled with the layer number $L+1$, the reduced coefficients must return the scattering coefficients for scattered EM fields a_n and b_n (see Eq. (2.37)). For that reason, $a_n = a_n^{(L+1)} = A_n^{L+1}$ and $b_n = b_n^{(L+1)} = B_n^{L+1}$, where $c_n^{(L+1)} = d_n^{(L+1)} = 1$. Consequently, the EM fields that propagate in the solvent are given by

$$\begin{aligned}
\mathbf{E}_i + \mathbf{E}_s = \mathbf{E}_{L+1} &= \sum_{n=1}^{\infty} E_n[\mathbf{M}_{o1n}^{(j_n)} - i\mathbf{N}_{e1n}^{(j_n)} + ia_n^{(L+1)}\mathbf{N}_{e1n}^{(h_n^{(1)})} - b_n^{(L+1)}\mathbf{M}_{o1n}^{(h_n^{(1)})}], \\
\mathbf{H}_i + \mathbf{H}_s = \mathbf{H}_{L+1} &= -\frac{k_l}{\omega\mu}\sum_{n=1}^{\infty} E_n[\mathbf{M}_{e1n}^{(j_n)} + \mathbf{N}_{o1n}^{(j_n)} - ib_n^{(L+1)}\mathbf{N}_{o1n}^{(y_n)} - a_n^{(L+1)}\mathbf{M}_{e1n}^{(y_n)}],
\end{aligned} \tag{2.51}$$

where the incident EM fields are $\mathbf{E}_i$ and $\mathbf{H}_i$, given in Eqs. (A.2) and (A.3) of Appendix A, respectively. Thus, the recursive algorithm terminates at $l = L+1$. In summary, Yang developed a general formulation in which the solvent is treated as an additional layer, allowing the scattering coefficients to be calculated recursively by taking advantage of the fact that the coefficients for the sphere's core are known.

Finally, we rewrite the Eq. (2.49) and (2.50) in a more readable version as

$$A_n^{(l+1)} = R_n(m_{l+1}x_l)\frac{m_{l+1}H_n^a(m_l x_l) - m_l D_n^{(1)}(m_{l+1}x_l)}{m_{l+1}H_n^a(m_l x_l) - m_l D_n^{(3)}(m_{l+1}x_l)}, \tag{2.52}$$

$$B_n^{(l+1)} = R_n(m_{l+1}x_l)\frac{m_l H_n^b(m_l x_l) - m_{l+1} D_n^{(1)}(m_{l+1}x_l)}{m_l H_n^b(m_l x_l) - m_{l+1} D_n^{(3)}(m_{l+1}x_l)}, \tag{2.53}$$

where $H_n^{(a)}(z)$ and $H_n^{(b)}(z)$ are given by

$$H_n^{(a)}(m_l x_l) = \frac{R_n(m_l x_l)D_n^{(1)}(m_l x_l) - A_n^{(l)} D_n^{(3)}(m_l x_l)}{R_n(m_l x_l) - A_n^{(l)}}, \tag{2.54}$$

$$H_n^{(b)}(m_l x_l) = \frac{R_n(m_l x_l)D_n^{(1)}(m_l x_l) - B_n^{(l)} D_n^{(3)}(m_l x_l)}{R_n(m_l x_l) - B_n^{(l)}}. \tag{2.55}$$

Here, $D_n^{(1)}(z) = \psi_n'(z)/\psi_n(z)$ and $D_n^{(3)}(z) = \zeta_n'(z)/\zeta_n(z)$ are the logarithmic derivative of the Ricatti-Bessel function of the first kind $\psi_n(z)$ and the Hankel function of the first kind $\zeta_n(z)$, respectively, and $R_n(z) = \psi_n(z)/\zeta_n(z)$. For the outer region, $m_{L+1} = 1$, then the scattering coefficients are given by

$$a_n = A_n^{(L+1)} = R_n(x_L)\frac{H_n^a(m_L x_L) - m_L D_n^{(1)}(x_L)}{H_n^a(m_L x_L) - m_L D_n^{(3)}(x_L)}, \tag{2.56}$$

$$b_n = B_n^{(L+1)} = R_n(x_L)\frac{m_L H_n^b(m_L x_L) - D_n^{(1)}(x_L)}{m_L H_n^b(m_L x_L) - D_n^{(3)}(x_L)}. \tag{2.57}$$

For this case, it's convenient to develop the terms $R_n(x_L)$, $D_n^{(1)}(x_L)$ and $D_n^{(3)}(x_L)$ to obtain the following equations:

$$a_n = A_n^{(L+1)} = \frac{H_n^a(m_L x_L)\frac{\psi_n(x_L)}{m_L} - \psi_n'(x_L)}{H_n^a(m_L x_L)\frac{\zeta_n(x_L)}{m_L} - \zeta_n'(x_L)}, \tag{2.58}$$

$$b_n = B_n^{(L+1)} = \frac{m_L H_n^b(m_L x_L)\psi_n(x_L) - \psi_n'(x_L)}{m_L H_n^b(m_L x_L)\zeta_n(x_L) - \zeta_n'(x_L)}. \tag{2.59}$$

Using the recurrence relationship for the Riccati-Bessel functions, given in Eq. (2.23), we can rewrite the Eq. (2.56) and (2.57) as

$$a_n = A_n^{(L+1)} = \frac{[H_n^a(m_L x_L)/m_L + n/x_L]\psi_n(x_L) - \psi_{n-1}(x_L)}{[H_n^a(m_L x_L)/m_L + n/x_L]\zeta_n(x_L) - \zeta_{n-1}(x_L)}, \tag{2.60}$$

$$b_n = B_n^{(L+1)} = \frac{[m_L H_n^a(m_L x_L) + n/x_L]\psi_n(x_L) - \psi_{n-1}(x_L)}{[m_L H_n^a(m_L x_L) + n/x_L]\zeta_n(x_L) - \zeta_{n-1}(x_L)}. \tag{2.61}$$

After computing the scattering coefficients a_n and b_n in Eqs. (2.60) and (2.61), the multilayered sphere's radiative properties can be evaluated using the same expressions of $S_1(\theta)$, $S_2(\theta)$ and $F(\theta)$ deduced from the Mie solution for a homogenous sphere.

2.2.1 Computational aspects of the Mie solution for a multilayer sphere

Yang's algorithm follows almost all steps for numerical calculation established in the Mie solution for a homogeneous sphere (see Subsec. 2.1.2). Also, Yang's algorithm uses the empirical Wiscombe's cutoff criterion for the series computation of scattering amplitude functions $S_1(\theta)$ and $S_2(\theta)$, given in Eq. (2.11). For a multilayer sphere, the series computation is cut at n_{stop}, defined in terms of the sphere's size parameter, x_L, as:

$$n_{\text{stop}} = \begin{cases} \lceil x_L + 4x_L^{1/3} + 1 \rceil, & 0.02 \leq x_L \leq 8; \\ \lceil x_L + 4.05x_L^{1/3} + 2 \rceil, & 8 < x_L \leq 4200; \\ \lceil x_L + 4x_L^{1/3} + 2 \rceil, & 4200 < x_L \leq 20000. \end{cases} \tag{2.62}$$

It's important to note that the cutoff criterion is valid over a particle size parameter range between 0.02 and 20000. Considering a wavelength of 632 nm (red light) and particles suspended in water, the abovementioned range corresponds to a particle size range of approximately 1 nanometer to 1 meter, which covers the mesoscopic scale (from a few nanometers to a few microns).

The round-off numerical errors associated with the Riccati-Bessel functions are avoided, as in the BHMIE algorithm, by introducing their logarithmic derivatives in Eqs. (2.52), (2.53), (2.60) and (2.61). The logarithmic derivative $D_n^{(1)}$ is calculated following a downward recurrence. Therefore, a enough large $n_{\max}$ must be choose to start the downward recurrence at $D_{n_{\max}}^{(1)}(z) \approx 0 + i0$. Yang uses a similar criterion used in the BHMIE algorithm to choose $n_{\max}$, given by

$$n_{\max} = \max(n_{\text{stop}}, \lceil |m_l x_l| \rceil, \lceil |m_l x_{l-1}| \rceil) + 15, \quad l = 1, \cdots, L. \tag{2.63}$$

The logarithmic derivative $D_n^{(3)}(z)$, associated with the first kind of Hankel function, is calculated by Yang using an upward recurrence that begins with $D_0^{(3)} = i$. Both logarithmic derivative $D_n^{(1)}$ and $D_n^{(3)}$ satisfy same recurrence expression given by

$$D_n^{(i)}(z) = [n/z - D_{n-1}^{(i)}(z)]^{-1} - n/z, \quad i = 1, 3. \tag{2.64}$$

The ratio $R_n(z) = \psi_n(z)/\zeta_n(z)$, used in Eqs. (2.52) (2.53), (2.60) and (2.61), can be evaluated using the general recursive relation in Eq. (2.64), as follows,

$$R_n(z) = \frac{\psi_n(z)}{\zeta_n(z)} = \frac{\psi_{n-1}(z)}{\zeta_{n-1}(z)} \frac{[D_n^{(3)}(z) + n/z]}{[D_n^{(1)}(z) + n/z]}. \tag{2.65}$$

This recurrence can be upward evaluated beginning at

$$\psi_0(z)/\zeta_0(z) = \frac{1 - \exp(-2\text{Re}\{z\}i)\exp(2\text{Im}\{z\})}{2}, \tag{2.66}$$

with $z = m_l x_l$, where m_l is in general a complex number. However, $R_0(z) = \psi_0(z)/\zeta_0(z)$ increases exponentially with $\text{Im}\{z\}$, which may be the case for strongly absorbing spheres. The latter may eventually cause a numerical overflow in the recurrence's higher orders. Yang solved this problem by introducing the ratio $Q_n^{(l)} = R_n(m_l x_{l-1})/R_n(m_l x_l)$ in Eqs. (2.54) and (2.55), which can be upward evaluated following the next relation:

$$Q_n^{(l)} = Q_{n-1}^{(l)} \frac{[D_n^{(3)}(z_1) + n/z_1]/[D_n^{(1)}(z_1) + n/z_1]}{[D_n^{(3)}(z_1) + n/z_1]/[D_n^{(3)}(z_1) + n/z_1]}, \tag{2.67}$$

with the starting ratio given by

$$Q_0^{(l)} = \frac{\exp(-i2\text{Re}\{z_1\}) - \exp(-2\text{Im}\{z_1\})}{\exp(-i2\text{Re}\{z_2\}) - \exp(-2\text{Im}\{z_2\})} \exp[-2(\text{Im}\{z_2\} - \text{Im}\{z_1\})], \tag{2.68}$$

where $z_1 = m_l x_{l-1}$ and $z_2 = m_l x_l$. Therefore, the ratio $Q_0^{(l)}$ is always bounded because $\text{Im}\{z_2\} = x_l \text{Im}\{m_l\} > \text{Im}\{z_1\} = x_{l-1}\text{Im}\{m_l\}$, thus avoiding a numerical overflow in the computation of H_n^a

and H_n^b.

To introduce the ratio $Q_n^{(l)}$ in Eqs. (2.54) and (2.55), observe that in Eqs. (2.54) and (2.55), using Eqs. (2.52) and (2.53) we can find the terms $A_n^{(l)}$ and $B_n^{(l)}$, and are given by

$$A_n^{(l)} = R_n(m_l x_{l-1}) \frac{m_l H_n^a(m_{l-1}x_{l-1}) - m_l D_n^{(1)}(m_l x_{l-1})}{m_l H_n^a(m_{l-1}x_{l-1}) - m_{l-1} D_n^{(3)}(m_l x_{l-1})}, \tag{2.69}$$

$$B_n^{(l)} = R_n(m_l x_{l-1}) \frac{m_{l-1} H_n^b(m_{l-1}x_{l-1}) - m_l D_n^{(1)}(m_l x_{l-1})}{m_{l-1} H_n^b(m_{l-1}x_{l-1}) - m_l D_n^{(3)}(m_l x_{l-1})}. \tag{2.70}$$

Replacing Eqs. (2.69) and (2.70) in Eqs. (2.54) and (2.55), respectively, we can write the following equations:

$$H_n^a(m_l x_l) = \frac{\left\{ \begin{array}{l} R_n(m_l x_l) D_n^{(1)}(m_l x_l) \\ \quad - \left[R_n(m_l x_{l-1}) \frac{m_l H_n^a(m_{l-1}x_{l-1}) - m_l D_n^{(1)}(m_l x_{l-1})}{m_l H_n^a(m_{l-1}x_{l-1}) - m_{l-1} D_n^{(3)}(m_l x_{l-1})} \right] D_n^{(3)}(m_l x_l) \end{array} \right\}}{R_n(m_l x_l) - \left[R_n(m_l x_{l-1}) \frac{m_l H_n^a(m_{l-1}x_{l-1}) - m_l D_n^{(1)}(m_l x_{l-1})}{m_l H_n^a(m_{l-1}x_{l-1}) - m_{l-1} D_n^{(3)}(m_l x_{l-1})} \right]}, \tag{2.71}$$

$$H_n^b(m_l x_l) = \frac{\left\{ \begin{array}{l} R_n(m_l x_l) D_n^{(1)}(m_l x_l) \\ \quad - \left[R_n(m_l x_{l-1}) \frac{m_{l-1} H_n^b(m_{l-1}x_{l-1}) - m_l D_n^{(1)}(m_l x_{l-1})}{m_{l-1} H_n^b(m_{l-1}x_{l-1}) - m_l D_n^{(3)}(m_l x_{l-1})} \right] D_n^{(3)}(m_l x_l) \end{array} \right\}}{R_n(m_l x_l) - \left[R_n(m_l x_{l-1}) \frac{m_{l-1} H_n^b(m_{l-1}x_{l-1}) - m_l D_n^{(1)}(m_l x_{l-1})}{m_{l-1} H_n^b(m_{l-1}x_{l-1}) - m_l D_n^{(3)}(m_l x_{l-1})} \right]}. \tag{2.72}$$

Thus, by factorization of the terms $R_n(m_l x_l)$ and $[m_l H_n^a(m_{l-1}x_{l-1} - m_{l-1} D_n^{(3)}(m_l x_{l-1})]$ in Eq. (2.71), and $R_n(m_l x_l)$ and $[m_{l-1} H_n^b(m_{l-1}x_{l-1}) - m_l D_n^{(3)}(m_l x_{l-1})]$ in Eq. (2.72), we can find a numerically stable form for $H_n^a(z)$ and $H_n^b(z)$, given by

$$H_n^a(m_l x_l) = \frac{G_2 D_n^{(1)}(m_l x_l) - Q_n^{(l)} G_1 D_n^{(3)}(m_l x_l)}{G_2 - Q_n^{(l)} G_1}, \tag{2.73}$$

$$H_n^b(m_l x_l) = \frac{\tilde{G}_2 D_n^{(1)}(m_l x_l) - Q_n^{(l)} \tilde{G}_1 D_n^{(3)}(m_l x_l)}{\tilde{G}_2 - Q_n^{(l)} \tilde{G}_1}. \tag{2.74}$$

Here, $G_1, G_2, \tilde{G}_1$ and $\tilde{G}_2$ are defined by

$$\begin{aligned} G_1 &= m_l H_n^a(m_{l-1}x_{l-1}) - m_{l-1} D_n^{(1)}(m_l x_{l-1}), \\ G_2 &= m_l H_n^a(m_{l-1}x_{l-1}) - m_{l-1} D_n^{(3)}(m_l x_{l-1}), \\ \tilde{G}_1 &= m_{l-1} H_n^b(m_{l-1}x_{l-1}) - m_l D_n^{(1)}(m_l x_{l-1}), \\ \tilde{G}_2 &= m_{l-1} H_n^b(m_{l-1}x_{l-1}) - m_l D_n^{(1)}(m_l x_{l-1}). \end{aligned} \tag{2.75}$$

In summary, for a given wavelength, λ, solvent's refractive index, n_0, a sphere stratified in L-layers, where each layer has radius r_l and refractive index n_l, with n_l a complex number, and r_l and n_l sorted in a table progressively from the sphere's core, labeled with $l = 1$, to the sphere's outer layer, labeled with $l = L$, and the scattering angles θ_i, the Yang's algorithm for the Mie solution for a multilayer sphere makes the following steps:

1. For all layers l calculates $x_l = 2\pi n_0 r_l/\lambda = kr_l$ and $m_l = n_l/n_0$. Then, calculates n_{stop} using Eq. (2.62).

2. Calculates $n_{\max}$ using Eq. (2.63).

3. Generates a table of scattering angles θ_i and starts the upward recurrences for angular functions with $\pi_0(\theta_i) = 0$ and $\pi_1(\theta_i) = 1$.

4. Compute series for $S_1(\theta_i)$ and $S_2(\theta_i)$ in Eq. (2.11), from $n = 1$ and to $n = n_{\text{stop}}$. For each n in the series, the next iterative loop is followed:

   (a) $H_n^a(m_L x_L)$ and $H_n^b(m_L x_L)$ are calculated by upward recurrence using the recurrence relations given in Eqs. (2.73) and (2.74) following the next steps:

      i. The recurrence starts at the sphere's core where $H_n^a(m_1 x_1) = H_n^a(m_1 x_1) = D_n^{(1)}(m_1 x_1)$, and $D_n^{(1)}(m_1 x_1)$ is computed following a downward recurrence, from $n_{\max}$ to n, using Eq. (2.64) and starting with $D_{n_{\max}}^{(1)}(m_1 x_1) = 0 + i0$.

      ii. For the layers $l = 2, \cdots, L$, the next iterative loop is followed:

         A. Computes $D_n^{(1)}(m_l, x_{l-1})$ following a downward recurrence, from $n_{\max}$ to n, using Eq. (2.64) and starting with $D_{n_{\max}}^{(1)}(m_l x_{l-1}) = 0 + i0$.

         B. Computes $D_n^{(3)}(m_l x_{l-1})$ following an upward recurrence, from $n = 1$ to n, using Eq. (2.64) and starting with $D_0^{(1)}(m_l x_{l-1}) = i$.

         C. Evaluates G_1, G_2, $\tilde{G}_1$ and $\tilde{G}_2$ using Eq. (2.75).

         D. Computes $D_n^{(1)}(m_l, x_l)$ following a downward recurrence, from $n_{\max}$ to n, using Eq. (2.64) and starting with $D_{n_{\max}}^{(1)}(m_l x_l) = 0 + i0$.

         E. Computes $D_n^{(3)}(m_l x_l)$ following an upward recurrence, from $n = 1$ to n, using Eq. (2.64) and starting with $D_0^{(1)}(m_l x_l) = i$.

         F. Computes the ratio $Q_n^l = R_n(m_l x_{l-1})/R_n(m_l x_l)$ following an upward recurrence, from $n = 1$ to n, using Eq. (2.67) and starting by the evaluation of Eq. (2.68). Note that the values of $D_n^{(1)}(m_l, x_{l-1})$, $D_n^{(1)}(m_l, x_l)$, $D_n^{(3)}(m_l, x_{l-1})$ and $D_n^{(3)}(m_l, x_l)$, computed in the previous steps, are used for the evaluation of Eq. (2.67).

G. Evaluates $H_n^a(m_l x_l)$ and $H_n^b(m_l x_l)$ using Eqs. (2.73) and (2.74), where values of G_1, G_2, $\tilde{G}_1$, $\tilde{G}_2$, $Q_n^{(l)}$, $D_n^{(1)}(m_l, x_l)$ and $D_n^{(3)}(m_l x_l)$, computed in the previous steps in the present loop, are used.

H. Save the computed value of $H_n^a(m_l x_l)$ and $H_n^b(m_l x_l)$ as $H_n^a(m_{l-1} x_{l-1}) = H_n^a(m_l x_l)$ and $H_n^b(m_{l-1} x_{l-1}) = H_n^b(m_l x_l)$, where will be used for the evaluation of G_1, G_2, $\tilde{G}_1$ and $\tilde{G}_2$ of the next layer.

I. Moves to next layer $l = l+1$ and restart the current iterative loop. If $l+1 > L$, the loop is stopped.

(b) After evaluation of $H_n^a(m_L x_L)$ and $H_n^b(m_L x_L)$, we can compute the scattering coefficients $a_n = a_n^{(L+1)}$ and $b_n = b_n^{(L+1)}$ using the Eqs. (2.60) and (2.61), where the Riccati-Bessel functions $\psi_n(x)$ and $\zeta_n(x)$ are evaluated using Eq. (2.26).

(c) Angular functions $\pi_n(\theta_i)$ and $\tau_n(\theta_i)$ are computed for all scattering angles θ_i following the recurrence relations of Eq. (2.21).

(d) For all scattering angles θ_i, the n summand of $S_1(\theta_i)$ and $S_2(\theta_i)$ in Eq (2.11) is evaluated and added to the previous $n-1$ summands.

(e) Moves to the evaluation of the next $n+1$ summand of $S_1(\theta_i)$ and $S_2(\theta_i)$. If $n+1 > n_{\text{stop}}$, the loop is stopped.

5. Calculates $|S_1(\theta_i)|^2$ and $|S_2(\theta_i)|^2$ and the form factor function $F(\theta_i)$ as defined in Eq. (2.16). Finally, the algorithm saves results files in a `.dat` format and stops the program.

Our version of Yang's algorithm of the Mie solution for a multilayer sphere was coded in Fortran and compiled with the GNU Fortran 2008 compiler. All code and executables are available in our open-source GitHub repository (`https://github.com/Complex-Fluids-IFUNAM/Mie-Scattering`).

2.2.2 Luneburg's lens: a case of light scattered by a multilayer sphere

The Luneburg lens is a particular spherical lens with two focal points, one on the sphere's surface and the other at infinity. [36, 39] In Fig. 2.4a, we show two focus points on the sphere's surface, where two collections of light rays hit the sphere. All rays that hit a specific focus are deflected in the sphere until they are parallel. In the same way, if two plane wavefronts come from different directions, sketched as parallel rays, these plane wavefronts will be focused on a point on the sphere's surface. Rudolf Luneberg found that a spherical lens with the characteristics described above must have a radially nonhomogeneous refractive index (RI) profile with spherical symmetry, $n(r)$, which depends on the radius, r, as

$$n(r) = \sqrt{2 - (r/a)^2}, \tag{2.76}$$

with a the radius of the sphere. [36, 39] Observe that the RI profile goes to $\sqrt{2}$ when $r \to 0$, and

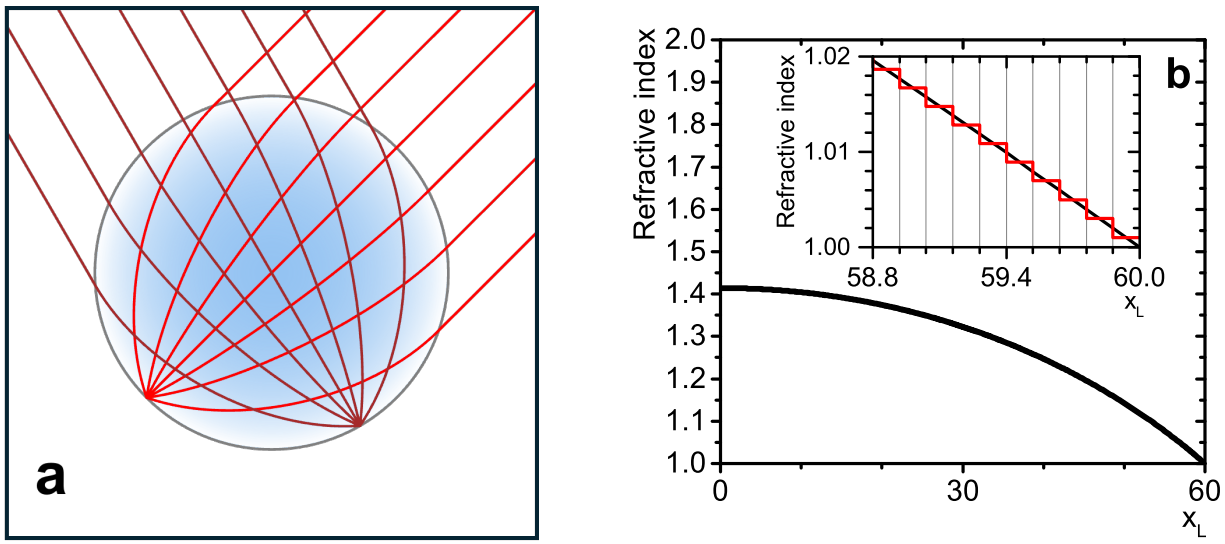

Figure 2.4: (a) Luneburg's lens sketch. The lines are light rays deflected by the optical properties of the lens. The radially blue shaded color depicts the lens' refractive index profile. (b) RI profile for a Luneburg lens with a size parameter of $x_L = 60$ stratified in 500 layers. Inset: detail of the last 10 layers of the lens, where the red line is the discrete RI profile, and the black line is the continuous Luneburg's lens RI profile in Eq. (2.76)

is one when $r = a$. The RI profile is presented as a blue color gradient in Fig. 2.4a. This kind of lens has been used in radar technology, and its possible applications have recently been explored in photonics, where the main challenge is synthesizing microscopic-sized Luneburg lenses. [36, 39, 40] Also, the Luneburg lens scattering properties have been studied using the Mie solution formalism, whose analytic solution is written in terms of generalized confluent hypergeometric function, and the solution for a multilayer sphere can describe, exactly, the scattering properties of such lens. [36] This allows the algorithms for the Mie solution for a multilayer sphere to be tested, especially the effect of the number of layers and their spacing on the discrete approximation of radially nonhomogeneous continuous profiles. [36–38]

Yang tested his algorithm using several discrete RI profiles, proving it does not propagate numerical errors. Yang's algorithm can, in particular, describe the scattering properties of a Luneburg's lens stratified in thin layers without losing its numerical stability. We replicate the form factor of the Luneburg lens to test our algorithm and verify that we can reproduce the same results as Yang. [38]

Fig 2.4b shows the RI profile for a Luneburg lens, used by Yang, with size parameter $x_L = 60$ and stratified into $L = 500$ equidistant layers. Observe that the discrete character cannot be distinguished because the layers are thin ($\Delta x \approx 0.12$) compared to the size parameter of the sphere. The RI profile in Eq. (2.76) is discretized as $m(\bar{x}_l) = \sqrt{2 - (\bar{x}_l/x_L)}$, where $\bar{x}_l = (x_{l-1} + x_l)/2$, with

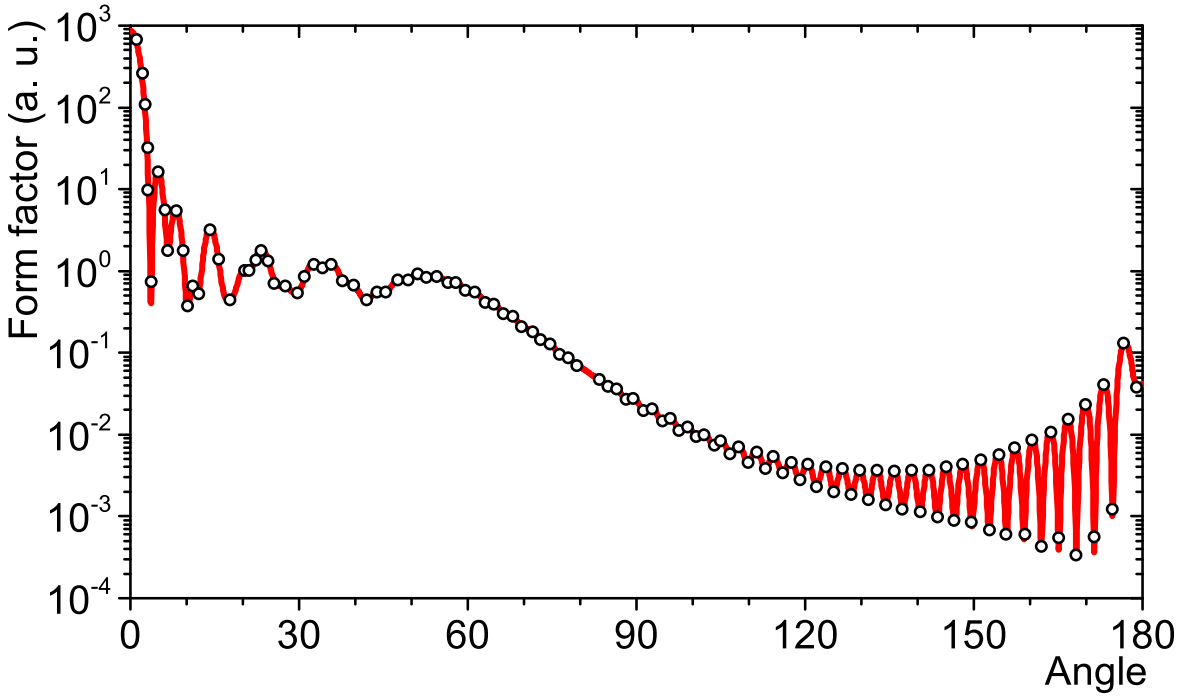

Figure 2.5: Form factor as a function of scattering angle (degrees) for a Luneburg lens with size parameter $x_L = 60$ and stratified in 500 layers. The circles were digitalized from Yang's results. [38]

$L = 1, \cdots, 500$, and $x_0 = 0$, *i. e.*, $\bar{x}_l$ is the mean radius between the two interfaces that define a layer. In the inset of Fig 2.4b, the RI profile of the last ten layers (red solid line) is compared with the continuous RI profile in Eq. (2.76). Observe that the RI of the last layer is not equal to one.

In Fig. 2.5, we show the form factor in arbitrary units (a. u.) as a function of the scattering angle θ for the Luneburg lens described above. Observe that the lens scatter light mainly in the forward direction. Also, we can see that the scattered intensity has a rippled structure along all scattering angles, with scattering intensity minima up to six orders of magnitude smaller than predicted in the forward direction ($\theta \to 0$). Also, we show some digitalized points (white circles) from Yang's results, showing that our code version of Yang's algorithm replicates his results successfully. [38]

Suppose the Luneburg lens, after described, is surrounded by air ($n_0 \approx 1$) and is illuminated by a light beam with a wavelength of $\lambda = 632.8$ nm (red light). Therefore, for this case, the lens has a radius of $a \approx 6043$ nm, and the layers have a thickness of $\Delta r \approx 12$ nm. So, we can conclude that Yang's algorithm can describe the scattering properties of multilayer spheres whose layers have a few nanometers of thickness. Nevertheless, we must be careful to set the thickness of the layers not only due to numerical issues but also due to the consistency of the physical framework; choosing layers with a thickness of less than a few nanometers could be outside the scope of classical electromagnetic theory. This discussion is not the subject of this thesis dissertation, so care will only be taken not

to force the theory beyond its known limits. [28]

2.3 Particles with size polydispersity

In light scattering experiments on colloidal suspensions, the laser's beam and the solid angle of the photodetector define a scattering volume with N scatterers. The multiple scattering is avoided if the suspension's colloid concentration is sufficiently diluted. For this case, the total scattering intensity measured by the photodetector is, in principle, proportional to the scattering intensity of a single particle, *i. e.*, $I_T \propto N I_s(\theta)$, as was discussed for Eqs. (2.18) and (2.19). However, this is only true for suspensions with identical colloidal particles, also known as monodisperse suspensions. Because, in practice, the particles embedded in a fluid are rarely monodisperse, the effect of scatterers' polydispersity must be considered. The particles in the suspension can, in general, be polydisperse in composition, shape, and size. In this dissertation, we will only consider that the particles are polydisperse in size and identical in constitution and shape.

The effect of size polydispersity on the total scattering intensity can be evaluated by considering that the total scattering intensity is the scattering intensity average over radii with a probability density distribution (PDF) of size, $\rho(R)$. Therefore, the scattering intensity by a single particle now depends on the radius, R, and the scattering angle where it is measured, θ. Then, the total scattering intensity by homogeneous particles can be calculated as

$$I_T(\theta) \propto \bar{I}_s(\theta) = \int_R I_s(R,\theta)\rho(R)dR, \tag{2.77}$$

and for core-shell particles can be calculated as

$$I_T(\theta) \propto \int_{R_s}\int_{R_c} I_s(R_c,R_s,\theta)\rho(R_c)\rho(R_s)dR_c\ dR_s, \tag{2.78}$$

where R_c and R_s are the core and shell's radius whose size has been considered independent. The PDF used for the average evaluation is chosen considering those where $R > 0$. For the case of spherical colloidal particles, it's common to assume that particles have a size distribution that follows a lognormal distribution. [41–45] This assumption has been tested by direct measurement of spherical particles' sizes using techniques such as Scanning Electron Microscopy (SEM) and Atomic Force Microscopy (AFM). [43] Some growth models in particle synthesis consider that the volume change is a random process with an exponential drift, which causes a lognormal behavior in the particles' size. [42] Therefore, we assume that the particles studied in this thesis dissertation follow a lognormal size distribution.

The lognormal distribution is defined as a continuous PDF of a random variable whose logarithm, in this case, the radius' logarithm, $\ln R$, is normally distributed instead of R. The following equation

gives the lognormal PDF: [41, 46, 47]

$$\rho(R) = \frac{1}{R\sqrt{2\pi}\ln\sigma_{\text{stg}}} \exp\left\{-\frac{1}{2}\left[\frac{\ln\left(R/\tilde{R}\right)}{\tilde{\sigma}_g}\right]^2\right\}, \quad R \in (0,\infty) \tag{2.79}$$

where $\tilde{\sigma}_g = \ln\sigma_{\text{g}}$, and σ_{g} is the geometric standard deviation. Note that $\tilde{\sigma}_g > 0$, therefore $\sigma_{\text{g}} > 1$. If $\sigma_{\text{g}} = 1$, then the particles are monodisperse. In this thesis dissertation, σ_g is used to measure the size of polydispersity. On the other hand, in Eq. (2.79), $\tilde{R}$ is the median population value. The lognormal distribution is not centered at the average value, $\bar{R}$, which also differs from the most probable value or mode, R_0. It can be shown that the mean and modal value is related to the average value as $\bar{R} = \tilde{R}\exp\left(\tilde{\sigma}_g^2/2\right)$ and $R_0 = \tilde{R}\exp -(\tilde{\sigma}_g^2)$. For our purposes, it's convenient to write the lognormal distribution as a function of the modal value. After some algebraic operations, we can show that Eq. (2.79) can be written in terms of R_0 as

$$\rho_{\text{ZOLD}}(R) = \frac{\exp\left(-\tilde{\sigma}_g^2/2\right)}{\sqrt{2\pi}R\tilde{\sigma_g}} \exp\left\{-\frac{1}{2}\left[\frac{\ln(R/R_0)}{\tilde{\sigma}_g}\right]^2\right\}, \quad R \in (0,\infty) \tag{2.80}$$

where is also known as the Zeroth-Order Logarithmic Distribution (ZOLD). [44, 46, 47] Fig. 2.6 is shown the ZOLD PDF for the size polydispersity of a particle with modal radius $R_0 = 500$ nm and $\sigma_g = 1.10$. Note that a ZOLD PDF with the mentioned characteristics is similar to a Normal PDF. Nevertheless, the average radius is $\bar{R} = R_{avg} = 506.9$ nm and the median radius is $\tilde{R} = R_{\text{median}} = 504.6$ nm. Therefore, a slight positive kurtosis is observed.

Although Eq. (2.80) is defined for $R \in (0,\infty)$, the particle size is finite. Then, the integrals in Eqs. (2.77) and (2.78) must be definite integrals, where the integration interval, $[R_{\text{min}}, R_{\text{max}}]$, should be chosen to cover most of the radii population. In our case, the integration interval is set by $R_{\text{min}} = R_0\sigma_g^{-\sqrt{18}}$ and $R_{\text{max}} = R_0\sigma_g^{\sqrt{18}}$, that covers $\sim 99.7\%$ of the population, similar to the 3σ rule for normal distribution. [45] For the case presented in Fig. 2.6, the $R_{\text{min}} = 333.7$ nm and $R_{\text{max}} = 749.2$ are shown in red dashed-lines. Finally, the total scattering intensity for homogeneous spherical particles can be calculated using the following equation:

$$I_T(\theta) \propto \int_{R_0\sigma_g^{-\sqrt{18}}}^{R_0\sigma_g^{\sqrt{18}}} I_s(R,\theta)\rho_{\text{ZOLD}}(R)dR \tag{2.81}$$

and for core-shell spherical particles using the following equation:

$$I_T(\theta) \propto \int_{R_{s_{\text{min}}}}^{R_{s\text{max}}} \int_{R_{c_{\text{min}}}}^{R_{c\text{max}}} I_s(R_c,R_s,\theta)\rho_{\text{ZOLD}}(R_c)\rho_{\text{ZOLD}}(R_s)dR_c\ dR_s. \tag{2.82}$$

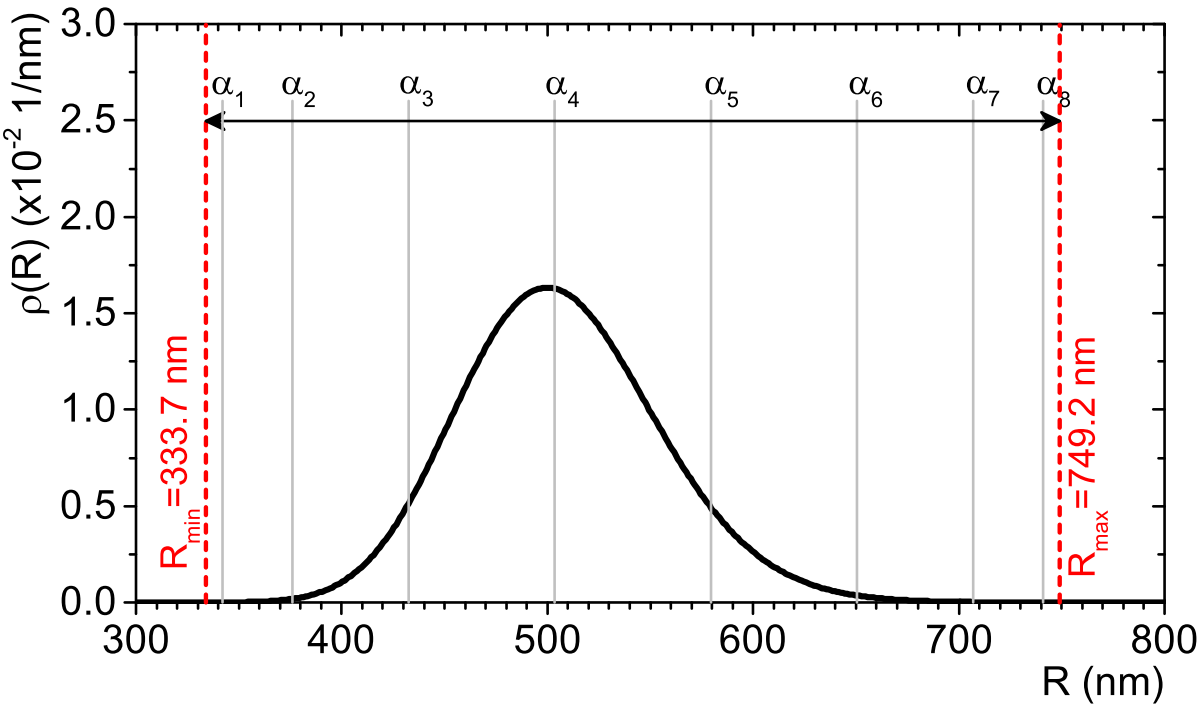

Figure 2.6: Zeroth-order logarithmic distribution function for the size polydispersity of a spherical particle with modal radius $R_0 = 500$ nm and geometrical standard deviation $\sigma_g = 1.10$. Here, the integration interval for the average integral is shown with red dashed lines. The nodes, α_i, are shown in gray lines for the numerical evaluation of the average integral. The latter is described in Subsection 2.3.1

2.3.1 Numerical evaluation of the average's integrals for scattering intensity by particles with size polydispersity

The evaluation of integrals in Eqs. (2.81) and (2.82) involves the computation of scattering intensity for several radii along the integration interval $[R_{\min}, R_{\max}]$. Also, because the scattering intensity could change their rippled structure with the size's particle, the numerical evaluation of Eqs. (2.81) and (2.82) by trapezoidal quadratures would require that the integration interval must be partitioned into many subintervals to obtain accurate results, increasing the computation time. Therefore, it becomes necessary to use a quadrature that allows us to get an estimation of the effect of polydispersity on scattering intensity with the least amount of subintervals possible.

The Gaussian quadratures can approximate integrals using fewer nodes N than trapezoidal quadratures by carefully choosing non-equally spaced nodes α_i and weight coefficients w_i. The integral of a function $g(x) = W(x)f(x)$ over the interval $[a, b]$, can be approximated to a Gaussian

quadrature as: [48, 49]

$$\int_a^b W(\alpha) f(\alpha) d\alpha \approx \sum_{i=1}^{N} w_i f(\alpha_i), \tag{2.83}$$

where $W(\alpha)$ is a given weight function. The theory of Gaussian quadratures with arbitrarily $W(\alpha)$ uses the formalism of orthonormal polynomials to find the nodes α_i and weight coefficients w_i. A more detailed introduction to these quadratures can be found in ref. [49].

In the literature, we can find algorithms for calculating the nodes and their weight coefficients for well-studied weight functions. [48] Particularly, the Gauss-Legendre quadrature is defined with $W(x) = 1$ in Eq. (2.83), where the nodes α_i are the roots of Legendre's polynomial function, $P_N(x)$, and the following equation defines the weight coefficients: [48]

$$w(\alpha_i) = \frac{2}{(1-\alpha_i^2)[P'_N(\alpha_i)]^2}. \tag{2.84}$$

Extending quadrature for multiple integrals is easy if the integration interval is rectangular. The product integration rule allows approximate two-dimensional (or more) integrals over a rectangular region by the following Gauss-Legendre quadrature: [49]

$$\int_{-1}^{1}\int_{-1}^{1} f(\alpha, y)\ d\alpha\ dy \approx \sum_{i=1}^{N_x} w_i \left[\sum_{j=1}^{N_y} w_j f(\alpha_i, y_j)\right]. \tag{2.85}$$

Gauss-Legendre quadrature is suitable for the evaluation of the average integrals in Eqs. (2.81) and (2.82), where we can set $W(\alpha) = 1$. Therefore, we can approximate the average integral in Eqs. (2.81) by following Gauss-Legendre quadrature:

$$\int_{R_{\min}}^{R_{\max}} I_s(R,\theta)\rho_{\mathrm{ZOLD}}(R)dR = \int_{-1}^{1} f(\alpha)d\alpha \approx \sum_{i=1}^{N} w(\alpha_i) f(\alpha). \tag{2.86}$$

Here, a linear parametrization for R is proposed as $R(\alpha) = R_m\alpha + R_b$, where the sloop is $R_m = (R_{\max} + R_{\min})/2$ and the R-intercept is $R_b = (R_{\max} + R_{\min})/2$. For the case presented in Fig. 2.6, we can observe that if eight nodes are used for the numerical evaluation of the average integral, the nodes are not centered at R_0 (gray lines). Because ZOLD has a positive kurtosis, there will be a higher node density for size above R_0.

In the same way, for the evaluation of the average integral in Eq. (2.82), the following Gauss-

Legendre quadrature is proposed:

$$\int_{R_{s_{\min}}}^{R_{s_{\max}}} \int_{R_{c_{\min}}}^{R_{c_{\max}}} I_s(R_c, R_s, \theta)\rho_{\text{ZOLD}}(R_c)\rho_{\text{ZOLD}}(R_s)\, dR_c\, dR_s = \int_{-1}^{1}\int_{-1}^{1} f(\alpha, y)\, d\alpha\, dy \approx \sum_{i=1}^{N_x} w_i \left[\sum_{j=1}^{N_y} v_j f(\alpha_i, y_j)\right], \quad (2.87)$$

where a linear parametrization for R_c and R_s is proposed similarly to the proposal for Eq. (2.86).

In summary, for a given wavelength, λ, solvent's refractive index, n_0, the dielectric properties of a homogeneous sphere with a modal size and a geometric standard deviation, R_0 and σ_g, or a stratified sphere whose characteristic sizes are the core and shell's radius, with modal radius values and geometric standard deviations, R_{c_0} and R_{s_0}, and σ_{g_c} and σ_{g_s}, respectively, and the nodes' number for the Gauss-Legendre quadrature, N, the algorithm for calculating of the average scattering intensity due particles size's polydispersity makes the following steps:

1. Calculates the integration limits for the average in Eqs. (2.86) and (2.87) as $R_{\min}^{\max} = R_p\sigma_{g_p}^{\pm\sqrt{18}}$, where R_p and σ_{g_p} are the modals radius and the geometric standard deviation for a homogeneous sphere, R_0 and σ_g, or for a stratified sphere whose characteristic sizes are the modal core and shell's radius, R_c and R_s, with geometric standard deviations σ_{g_c} and σ_{g_s}.

2. In the loop from $i = 1$ to $i = N_x$, with N_x the nodes' number, calculates the i-th node and weight coefficient, α_i and w_i, following the next steps:

   (a) Calculates the i-th root of the Legendre polynomial function of degree N, α_i, using the Newton-Raphson's method. [48]

   (b) Calculates the weight coefficient w_i using the Eq. (2.84) with the previously calculated roots, α_i.

   (c) For average integral in Eq. (2.87), the current loop is repeated for the shell's radius with nodes and weight functions y_j and v_j, and then the loop stops. For homogeneous spheres, the loops stop.

3. Initializes quadrature with sums equal to zero. Note that if the scattering intensity is calculated for non-polarized light, $I(R, \theta) \propto F(\theta)$, or if it's calculated for vertical-vertical polarized light, $I(R, \theta) \propto |S_1(\theta)|^2$. Therefore, the quadrature sums the functions $F(R_{s_i}, \theta)\rho(R_{s_i})$ or $|S_1(R_{s_i}, \theta)|^2\rho_{\text{ZOLD}}(R_{s_i})$, depending on the case.

4. **If** the average integral in Eq. (2.87) is calculating, follows the next steps:

   (a) In a loop from $i = 1$ to $i = N_x$, with N_x the nodes' number, the following steps are performed:

i. For the α_i node, evaluates R_{c_i} in the integration interval $[R_{c_{\min}}, R_{c_{\max}}]$ according to the core's radius parametrization $R_{c_i} = R_{c_m}\alpha_i + R_{c_b}$.

ii. In a loop from $j = 1$ to $j = N_y$, where N_y are the nodes' number for the shell's radius integration interval, following the next steps:

A. For the y_j node, evaluates R_{s_j} in the integration interval $[R_{s_{\min}}, R_{s_{\max}}]$ according to the shell's radius parametrization $R_{s_j} = R_{s_m}x_j + R_{s_b}$.

B. Using Yang's algorithm for the Mie solution's multilayer sphere, calculates $F(R_{c_i}, R_{s_j}, \theta)$ or $|S_1(R_{c_i}, R_{s_j}, \theta)|^2$.

C. Evaluates ZOLD PDF function for core and shell, $\rho(R_{c_i}, R_{c_0}, \sigma_{g_c})$ and $\rho_(R_{s_j}, R_{s_0}, \sigma_{g_s})$ using Eq. (2.80).

D. Calculate $S_{(i,j)} = \sum_{j=1}^{N_y} v_j F_(R_{c_i}, R_{s_j}, \theta)\rho(R_{c_i}, R_{c_0}, \sigma_{g_c})\rho(R_{s_j}, R_{s_0}, \sigma_{g_s})$, where v_j is the j-th weight coefficient. If $j = 1$, then the sum is starting.

iii. Evaluates the sum $\sum_{i=1}^{N_x} w_i[S_{(i,j)}]$, where w_i is the i-th weight coefficient and the term $S_{(i,j)}$ was calculated in the previous loop.

Else if the average integral for a homogeneous sphere in Eq. (2.86) is calculating, in a loop from $i = 1$ to $i = N_x$, with N_x the nodes' number, the following steps are performed:

(a) For the α_i node, evaluates R_i in the integration interval $[R_{\min}, R_{\max}]$ according to the radius parametrization $R_i = R_m\alpha_i + R_b$.

(b) Using the BHMIE algorithm for the Mie solution's homogeneous sphere, calculates $F(R_i, \theta)$ or $|S_1(R_i), \theta)|^2$.

(c) Evaluates ZOLD PDF function for the sphere's radius, $\rho(R_i, R_0, \sigma_g)$ using Eq. (2.80).

(d) Calculates $\sum_{i=1}^{N_x} w_j F(R_i, \theta)\rho(R_i, R_0, \sigma_g)$, where w_i is the i-th weight coefficient. If $i = 1$, then the sum is starting.

5. Return results in a table with columns defined as $[\theta_i, F_{\text{poly}}(\theta_i), |S_{1\text{poly}}(\theta_i)|^2]$ and saves the result file in a `.dat` format and stops the program

Implementing the algorithm to calculate the average integral due to size polydispersity for homogeneous spheres is straightforward. However, care must be taken in the case of core-shell spheres, where the polydispersity values of the core and shell, given by σ_{g_c} and σ_{g_s} respectively, may cause overlap at the extreme values of the core and shell sizes, which should be avoided. For spheres with three or more layers, the algorithm implementation becomes more complex. Although Gauss-Legendre quadrature can be generalized to account for polydispersity in the size of each layer, the computation time increases considerably with the number of polydisperse layers. In our case, as will be shown later, a multi-thread computing module was used to parallelize the most time-consuming

part of the Gauss-Legendre quadrature, reducing the calculation time for polydisperse scattering intensity curves of PNIPAM and core-shell PS-PNIPAM particles, whose refractive index profiles are modeled with dozens of layers.

2.3.2 The effect of particle size polydispersity on light scattered intensity

Generally, for systems with size polydispersity, we can observe that the rippled structure in the average scattering intensity is damped compared to those in the monodisperse case. If the particle is small enough this effect is not observed. Let us consider a system of spherical polystyrene particles in water with $R_0 = 500$ nm, illuminated by a non-polarized red light beam with ($\lambda = 632.8$ nm). Then, the light scattered intensity is proportional to the form factor. Also, the particle's size parameter and relative refractive index are $x \approx 6.61$ and $m \approx 1.194$, respectively.

In Fig. 2.7, the form factor as a function of the scattering angle is shown for the system described above, both for monodisperse particles (black dashed line) and for particles with size polydispersity characterized by $\sigma_g = 1.05$ (red solid line), $\sigma_g = 1.10$ (green solid line), and $\sigma_g = 1.20$ (blue solid line). We can observe a rippled structure along all scattering angles with five minima for the monodisperse case. For particles with $\sigma_g = 1.05$ and $\sigma_g = 1.10$, the four first minima in the monodisperse system are attenuated, as was expected. Still, the last minimum, located at $\theta \sim 170°$, is more noticeable when σ_g increases. For particles with $\sigma_g = 1.20$, the two first minima in the monodisperse system are lost. Still, the third and fourth minima in the monodisperse system are more noticeable and shifted to low scattering angles compared to monodisperse and polydisperse systems with $\sigma_g = 1.05$ and $\sigma_g = 1.10$. Note that an additional minimum is formed at $\theta \sim 165°$.

In the inset of Fig. 2.7 is shown the ZOLD for polydisperse particles with $\sigma_g = 1.05$ (red solid line), $\sigma_g = 1.10$ (green solid line) and $\sigma_g = 1.20$ (blue solid line). Note that particles with $\sigma_g = 1.05$ and $\sigma_g = 1.10$ are similar to the Normal distribution function. However, the positive kurtosis is appreciable for $\sigma_g = 1.20$. As was mentioned, σ_g is a measure of polydispersity. Therefore, at higher polydispersity, the contribution of large particles than of small particles to the average scattered intensity is more significant. The latter could cause, as observed in Fig. 2.7, the formation of new minima in the average scattering intensity at large scattering angles concerning those in the monodisperse case.

As we have seen, for spherical particles, the formation of a rippled structure in the light scattered intensity as a function of the scattering angle depends mainly on the ratio between the size particle and the wavelength of the scattered light (see Fig. 2.2). If the particles are small enough not to scatter light with a rippled pattern along scattering angles, we can assume that a large polydispersity could generate a rippled structure on the average scattering intensity as a function on scattering angle.

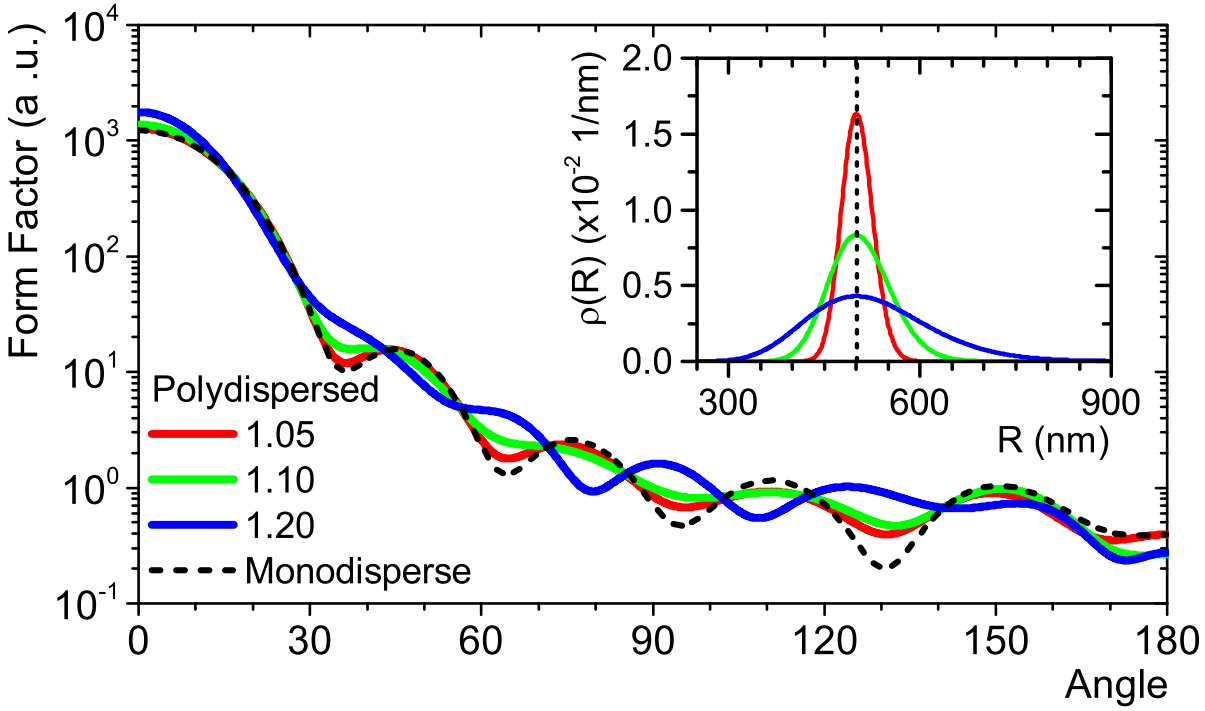

Figure 2.7: Form factor as a function of scattering angle for spherical polystyrene particles in water with $R = 500$ nm. Here, $\lambda = 632.8$ nm (red light). Inset: ZOLD for polydispersed particles. The cases shown correspond to the following: monodispersed particles in dashed-line and polydispersed particles with $\sigma_g = 1.05$ (red line), $\sigma_g = 1.10$ (green line) and $\sigma_g = 1.20$ (blue line).

The rippled feature in the angle scattering intensity is also presented for multilayer spheres. So we can expect the same damped effect on the rippled structure or the formation of a rippled structure on the average scattering intensity.

Chapter 3

Experimental techniques

As mentioned in this dissertation's introduction, our goal is to describe the light scattering behavior of the colloidal particles using the Mie scattering solution for multilayer spheres. For this reason, although other experimental techniques were used to characterize our synthesized particles, in this chapter, we review the two Light Scattering (LS) techniques used in this dissertation: Static Light Scattering (SLS) and Dynamic Light Scattering (DLS).

SLS and DLS are complementary and powerful techniques for characterizing particles in solution. In general, both techniques use the same experimental setup and measure the intensity of light scattered by the particles in suspension. However, they differ in how the experimental data are analyzed. While SLS relies on different theoretical approaches to light scattering phenomena, such as those discussed in Chapter 2, to describe the scattering intensity as a function of the scattering angle and thereby extract information such as particle shape, size, or even molecular weight, DLS analyzes fluctuations in the scattered intensity over time at a fixed scattering angle to estimate the diffusion coefficient, mean square displacement, and other dynamic properties of the suspended particles [50].

3.1 Static Light Scattering (SLS)

The static light scattering technique is based on the principle that when a beam of light is transmitted through a medium with dielectric heterogeneities, these heterogeneities scatter light in different directions and with varying intensities. In our case, these heterogeneities are spherical colloidal particles suspended in a solvent and, in general, could be any mesoscopic particles or even the thermal fluctuations in the liquid phase. The light scattering intensity by a homogeneous colloidal suspension is directly related to the particle concentration in the solvent (see sec. 2.3.2).

The SLS technique uses a laser source that emits a monochromatic and coherent light beam. The

light beam's size and the photodetector's area at a given position used to measure the scattering intensity define a scattering volume that encloses N colloids of the total number of particles in the suspension. Therefore, only the light scattered by the N particles in the scattering volume is detected by the photodetector at a given position (see Fig. 3.1). A data acquisition system (DAQ) filters and digitizes the signal from the photodetectors, enabling subsequent mathematical analysis. The acquired data are typically displayed as a histogram that relates the number of digital counts, measured in Hz (i.e., counts per second) over a given time interval, to the detected light intensity, accounting for the efficiency of the photo detector. Subsequently, the geometric mean of the recorded counts is calculated and reported as the mean light scattering intensity I_s of the suspension, expressed in kHz, at a given scattering angle θ.

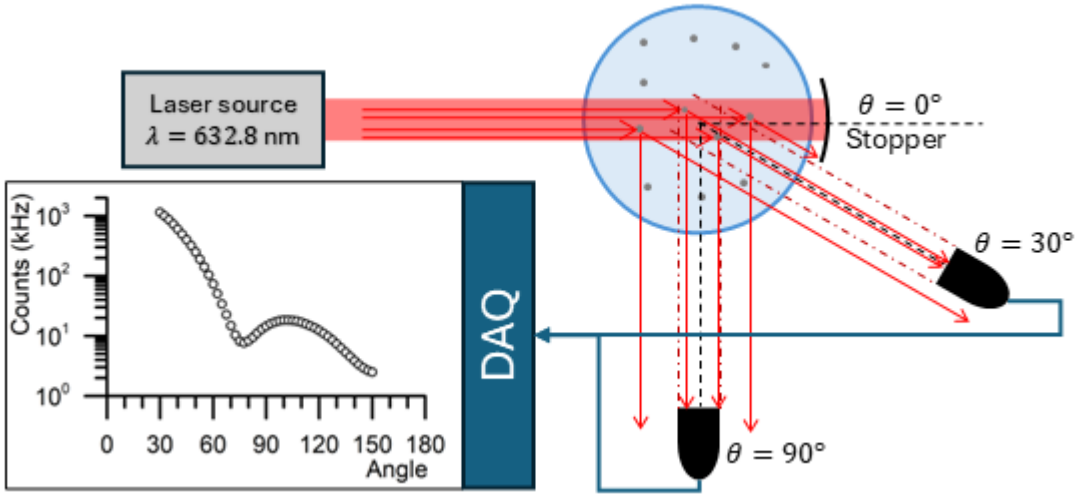

Figure 3.1: A schematic representation of a static light scattering experiment. Only the light scattered by the colloidal particles in the scattering volume is measured by a photodetector. Then, the signal detected is filtered and digitized by a DAQ system. The time-average digital counts are used to determine the sample's scattering intensity.

Specifically, we used an SLS setup designed by LS Instruments (Switzerland) and installed at the Metropolitan Autonomous University, Iztapalapa campus, in Mexico City, Mexico. The device, the 3D-DLS LS Instruments, employs a He-Ne laser source ($\lambda = 632.8$ nm), with the laser beam vertically polarized, and features the ability to split the captured scattered light and process it using two separate detector modules in a cross-correlation configuration. This cross-correlation configuration offers significant advantages over single-detector setups, as it effectively suppresses spurious correlations arising from detector afterpulsing and stray light, thereby enabling more accurate measurements, particularly in weakly scattering samples. Although the laser source operates at a constant output intensity, the intensity incident on the sample can be adjusted by placing neutral density filters along the optical path, allowing control over the illumination conditions without

modifying the laser's output power. Fig. 3.2 illustrates the general setup of the LS Instruments device used in this dissertation.

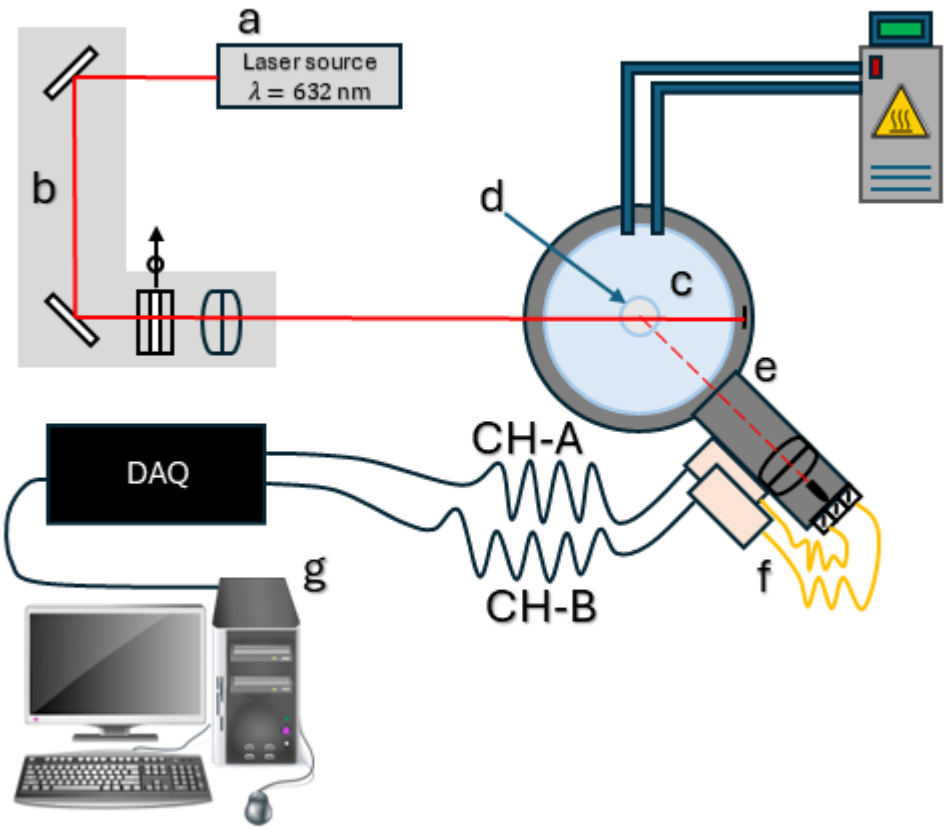

Figure 3.2: A typical SLS setup consists of the following components: (a) a laser source that provides a well-characterized monochromatic plane beam; (b) an optical system composed of mirrors, lenses, polarizers, and pinholes, which shape and direct the laser beam with proper alignment toward the sample. A simple photodetector measures the intensity of the incident light beam; (c) a thermostatted optical-glass sample chamber filled with a refractive index-matching liquid, such as decalin, which stabilizes the sample environment and minimizes thermal fluctuations; (d) a cuvette made of high-precision, optically transparent material, typically Pyrex glass or quartz, in which the sample is placed; (e) a goniometer that adjusts the angular position of the detector; (f) a light detection module consisting of lenses, optical filters, beam splitters, and an optical fiber that transmits the light scattered by the sample to the photodiodes; and (g) a data acquisition system that digitizes and processes the signal measured by the photodiodes.

3.1.1 Absolute scattering intensity

Since our goal is to measure the form factor of the colloidal particles, it is necessary to subtract the scattering intensity contributions from the solvent and the cuvette material, which are considered background scattering. This correction is expressed as $I_s(\theta) = I^*(\theta) - I_b(\theta)$, where $I_s(\theta)$ is the scattering intensity due to the colloidal particles, $I^*(\theta)$ is the total scattering intensity measured from the suspension within the cuvette, and $I_b(\theta)$ is the background scattering intensity.

As reviewed in Section 2.1.2, the differential scattering cross-section, $dC_{sca}/d\Omega$, given in Eq. (2.14), is defined as the ratio of the scattered to the incident light intensity. In SLS measurements, the scattered light is collected within the geometrical plane defined by the goniometer and at a fixed distance R from the scattering volume V_s. Therefore,

$$\frac{dC_{sca}}{d\Omega} = \frac{I_s(\theta)R^2}{I_0} \tag{3.1}$$

where I_0 is the intensity of the incident light beam, measured in milliwatts (mW). The scattering intensity, measured as the mean count rate, is normalized by the incident light intensity, which is adjusted using optical filters, since the laser operates at a constant output power. Thus, $I_s(\theta)$ has units of kHz/mW.

On the other hand, the scattering intensity by the colloidal particles in V_s is directly related to the average form factor function $\langle F(\theta)\rangle$ and the average static structure factor, $\langle S(\theta)\rangle$, as: [51, 52]

$$I_s(\theta) \propto \ \langle S(\theta)\rangle\langle F(\theta)\rangle. \tag{3.2}$$

In the last equation, the averages in $\langle\cdots\rangle$ are calculated here considering only the polydispersity of the particle size. The static structure factor $S(\theta)$ gives the contribution of the scattering due to the interaction between particles. When the suspension is sufficiently diluted to ensure the light is scattered only once into V_s, $S(\theta) \approx 1$. Therefore, Eq. (3.2) can be written as:

$$I_s(\theta) \propto \langle F(\theta)\rangle, \tag{3.3}$$

as was introduced by the Eq. (2.18) in sec. 2.1.2. Thus, using Eq. (3.1) in Eq. (3.3), a relation between $I_s(\theta)$ and $F(\theta)$ can given by the following equation: [52]

$$\frac{I_s(\theta)R^2}{I_0} = cKM\ \langle F(\theta)\rangle, \tag{3.4}$$

where c is the colloidal particle concentration, K is the optical contrast of the sample as a function of the concentration c, and M is the molecular weight of the colloidal particles. In practice, estimating the distance R is difficult, and the intensity of the incident light beam can fluctuate for various

reasons. Therefore, the Eq. (3.4) is normalized using the scattering intensity of a reference sample. A pure toluene sample is often used because its light scattering properties are well-behaved and widely reported in the literature. [51–53] Finally, the Eq. (3.4) can be written after the normalization as:

$$\frac{I_s(\theta)}{I_{\text{tol}}(\theta)} R_{\text{tol}} \left(\frac{n_0}{n_{\text{tol}}} \right)^2 = \kappa \langle F(\theta) \rangle, \tag{3.5}$$

where $I_{\text{Tol}}(\theta)$ is the scattering intensity measured for a pure toluene sample, $R_{\text{tol}} = 1.02074 \times 10^{-5}(1/\text{cm})$ is the Toluene Raleigh ratio, n_0 and n_{Tol} are the solvent and toluene RI, respectively, and κ is a proportional constant that contains all information of cKM and other experimental parameters and has units of (1/cm). The last equation allows the establishment of an experimental protocol to obtain an absolute scattering intensity of the particles in the suspension using the SLS technique and is given in the next subsection.

Finally, concerning the Eq. (3.5), it's important to note that this equation is often written in terms of q, quoting Ref. [51] verbatim, *for historical reasons*. Recall that $q = 2k_0 \sin\theta/2$, where $k_0 = 2\pi n/\lambda$ and θ is the scattering angle, so the use of Eq. (3.5) in terms of q or of the scattering angle θ is equivalent.

3.1.2 Experimental protocol

SLS experiments in very dilute suspensions allow us to approximate the measured scattering intensity to the form factor function, as given in Eq. (3.5). After properly calibrating the SLS setup with a toluene reference sample, we follow the steps below to measure the absolute scattering intensity of the suspended particles based on the key features of the protocol proposed in Ref. [51]:

1. **Sample preparation.** In this step, it is necessary to know the particle concentration in the suspension. In this dissertation, a diluted suspension sample with a solids concentration of 0.005% w/w in filtered deionized (DI) water is prepared in a cylindrical NMR Pyrex cuvette.

2. **Measurement of the scattering intensity of the diluted suspension.** The SLS experiment is conducted at a controlled temperature over a scattering angle range from 30° to 125°, in steps of 1°. Ten one-second scattering intensity measurements are taken at each scattering angle until the entire angular range is covered. This procedure is repeated six times, resulting in 60 one-second measurements per scattering angle. The 60 measurements at each angle are averaged and normalized by the incident light beam intensity. The final result previous any correction is the suspension scattering intensity, $I^*(\theta)$, with units of kHz/mW.

3. **Measurement of the background scattering intensity.** A cylindrical NMR Pyrex cuvette filled with filtered DI water is prepared. Then, an SLS experiment is conducted under the

same conditions as in the previous step. The final result is the background scattering intensity, $I_b(\theta)$, with units of kHz/mW.

4. **Estimation of the particle scattering intensity.** Equation (3.5) is evaluated using the measurements from the last two steps. The following constant values are used: $n_{\text{water}} = 1.332$, $n_{\text{Tol}} = 1.494$, and $R_{\text{Tol}} = 1.02074 \times 10^{-5}$ cm^{-1}. Additionally, $I_{\text{Tol}}(\theta)$, obtained from the device calibration, is used (see Fig. 3.3).

The result is reported as the particle scattering intensity, $I_s(\theta)$, in arbitrary units (a.u.). These results will be used to fit the Mie scattering solution for homogeneous or multilayer spheres (see Section 4.2).

Finally, an example of SLS experiment results is shown in Fig. 3.3. The SLS experiment is carried out for a diluted suspension of PS standard particles in filtered DI water, where the particles are reported by the manufacturer (Bangs Labs Inc.) as monodisperse, with a nominal radius of $R_{PS} = 50.1$ nm. In this experiment, we follow the above experimental protocol at a controlled temperature of 20 °C.

Figure 3.3(a) shows the mean scattering intensity for the three signals required to compute the absolute scattering intensity of the PS standard particles: the suspension scattering intensity $I^*(\theta)$, the background scattering intensity $I_b(\theta)$, and the toluene reference scattering intensity $I_{\text{Tol}}(\theta)$. Note that the toluene scattering signal is almost a flat line (red squares), which ensures that the SLS device has the proper optical and mechanical alignment to operate correctly. [51, 52]

In Fig. 3.3(b), the absolute scattering intensity of the PS standard particles is reported as a function of scattering angle, computed using Eq. (3.5). Also, the Mie scattering solution for a homogeneous sphere for monodisperse PS particles is shown. Notably, the Mie scattering solution for particles with the nominal radius value and for that one with a best-fit radius of 51.3 nm are very similar. The details for the numerical fit scheme will be reviewed in Chapter 5. These results confirm that the SLS setup is properly calibrated.

3.2 Dynamic Light Scattering

The Dynamic Light Scattering (DLS) technique measures the dynamic properties of mesoscopic particles in suspension. As in the SLS technique, the intensity of light scattered by suspension is measured at a given scattering angle and time interval in a DLS experiment. However, the scattering intensity measured is not time-averaged; instead, the intensity fluctuations recorded over the time interval are analyzed by computing the time correlation of the measured data. In mesoscopic particle suspensions, the thermal agitation keeps the suspended particles in constant motion.

Fig. 3.4 shows a schematic representation of a DLS experiment, where the photodetector measures the light scattered by the colloidal particles in V_s. The photodetector signal is filtered and

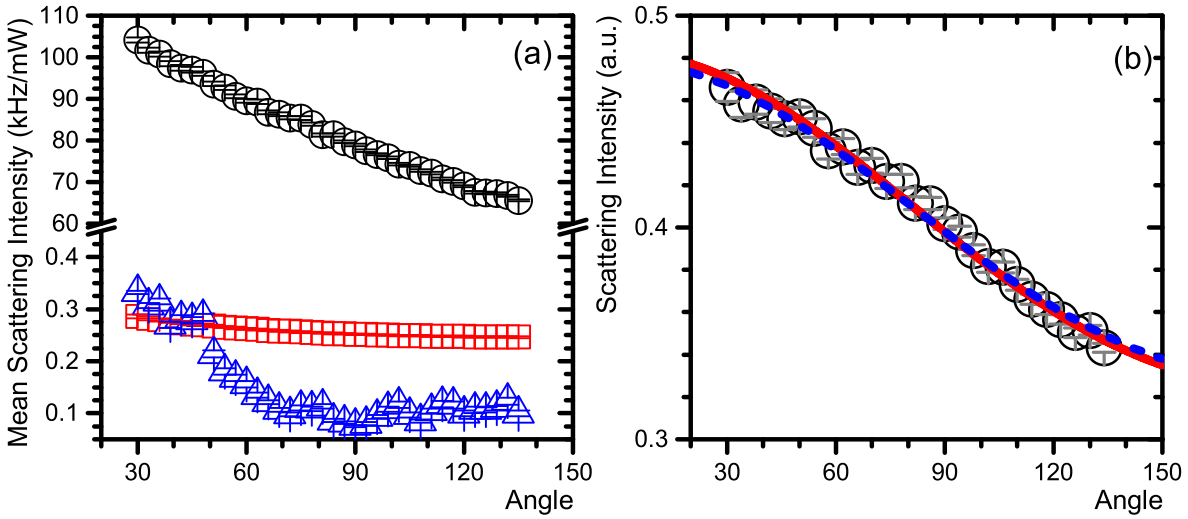

Figure 3.3: (a) Mean scattering intensity as a function of scattering angle for toluene reference sample I_{Tol} (red squares), background scattering intensity I_b (blue triangles), and PS standard particles suspension I^* (black circles). (b) I_s of the PS standard particles (black circles) and the Mie scattering solution for homogeneous particles for nominal radius $R = 50.1$ nm (blue dashed line) and the best-fit Mie scattering solution to the scattering intensity (black solid line). The best-fit radius is $R = 51.3$ nm.

digitized in a DAQ system, where the digital counts measure the light scattering intensity and have units of kHz. Then, the intensity autocorrelation function against a delay time is computed using the following equation:

$$g_2(\tau) = \frac{\langle I(t) \cdot I(t+\tau) \rangle}{\langle I(t) \rangle^2}, \tag{3.6}$$

where $I(t)$ is the scattering intensity at a time t, and $I(t-\tau)$ is the scattering intensity measured at a delay time $t+\tau$. The average in the angular parenthesis $\langle \cdots \rangle$, are over measurement time t. The intensity autocorrelation function measures how similar is the intensity at time t compared to the intensity after a delay τ.

The DLS experimental setup is usually similar to that of the SLS technique. In our case, we use the same 3D-DLS device (LS instrument, Switzerland), described in Section 3.1 (see Fig. 3.2), in one beam cross correlation setup, also known as pseudo-cross correlation setup. In this setup the one beam light scattering is splitter and collected by two independent detectors, A and B. Then, the detector test the same scattering volume but through different optical pats. Now, instead compute the autocorrelation function given in equation (3.6), the intensity pseudo-cross correlation function is computed using the signals from the two detectors as:

$$g_2(\tau) = \frac{\langle I_A(t) I_B(t+\tau) \rangle}{\langle I_A(t) \rangle \langle I_B(t) \rangle}. \tag{3.7}$$

Regardless the setup of the light scattering device, the intensity autocorrelation or the intensity

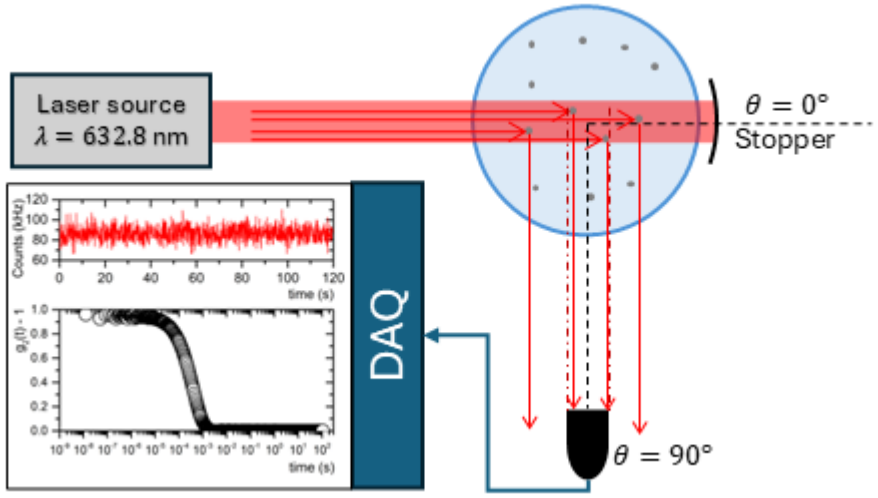

Figure 3.4: A dynamic light scattering experiment cartoon at a scattering angle of 90°. The colloidal particles are constantly in movement due to thermal agitation. Therefore, the light scattering intensity fluctuates over time. The autocorrelation function for the scattering intensity signal could provide information on the colloidal particle dynamics.

pseudo-cross correlation can be related to the dynamics of colloidal particles. Notably, if the solvent is Newtonian and the particles are spherical, the suspended particles could describe a Brownian motion, for which it is possible to find a relationship between the intensity correlation functions given in Eq. (3.6) and (3.7) with the particle size. This is the subject of the next subsection.

3.2.1 DLS for noninteracting colloidal particles

The intensity correlation functions $g_2(\tau)$, given in Eqs. (3.6) and (3.7), can be related to the correlation function of the scattered electric field through the Siegert relation, given by the following equation: [51, 54]

$$g_2(\tau) = \beta|g_1(\tau)|^2 + B = \beta\left|\frac{\langle \mathbf{E}_s(t)\mathbf{E}_s^*(t+\tau)\rangle}{\langle|\mathbf{E}_s(t)|\rangle}\right|^2 + B, \tag{3.8}$$

where $g_1(\tau)$ is the correlation function of the scattered electric field, β is a normalization constant, B is the long-time value of $g_2(\tau)$, also known as the baseline, and $\mathbf{E}_s(t)$ and $\mathbf{E}_s^*(t+\tau)$ is the scattered electric field at time t and its complex conjugate at a delay time $t-\tau$, respectively. The Siegert relation is valid only when: (i) the system is ergodic, that is, the time-average is equivalent to ensemble average; and (ii) the system must be stationary. [52, 55, 56]

As in the SLS technique, the static structure factor does not contribute to the scattering intensity measured if the suspension is sufficiently diluted. Thus, we can assess that the colloidal particles do not interact with each other and that the light is scattered only once in V_s. In this case, for

monodisperse particles, it can be shown that $g_1(\tau)$ is related to the mean squared displacement, $\langle \Delta r^2(\tau) \rangle$, by the following equation: [51, 52]

$$g_1(\tau) = \exp\left[-\frac{q^2 \langle \Delta r^2(\tau) \rangle}{6}\right], \tag{3.9}$$

where $q = 2k_0 \sin(\theta/2)$ is the magnitude of the scattering wave vector, $\mathbf{q}$. Since the particles in the suspension move due to thermal agitation, their motion is Brownian if they are immersed in a solvent such as water. Thus, $\langle \Delta r^2(\tau) \rangle = 6D\tau$, where D is the diffusion coefficient. The Stokes-Einstein equation relates the diffusion coefficient to thermal energy and the dissipative drag force due to the motion of the particles in the solvent and is given by:

$$D = \frac{k_B T}{6\pi\eta R_h}, \tag{3.10}$$

where k_B is the Boltzmann's constant, T the system temperature, η is the solvent's viscosity and R_h is the hydrodynamic radius of the colloidal particles. Using Eq. (3.9) in Eq. (3.8), the following relation is obtained for the scattering intensity correlation function $g_2(\tau)$ for monodisperse particles: [51, 52]

$$g_2(\tau) = \beta \exp\left[-2\Gamma\tau\right] + B, \tag{3.11}$$

where $\Gamma = q^2 D$. Therefore, the autocorrelation of the scattering intensity measured in a DLS experiment decays exponentially with a characteristic decay time of $1/\Gamma$; that is, in a DLS experiment, the scattering intensity fluctuations are correlated to the time it takes for a colloidal particle to move a distance similar to $q^{-1} \sim \lambda$.

Nevertheless, as reviewed in Section 2.3.2, colloidal particles are rarely monodisperse in size. Therefore, as in Eqs. (2.81) and (2.82), we must introduce a size distribution function, $G(\Gamma)$, into Eq. (3.11). Consequently, $g_2(t)$ is related to an average exponential decay, given by: [51, 57]

$$g_2(\tau) = \beta \left[\int_0^\infty \exp(-\Gamma\tau) G(\Gamma) d\Gamma\right]^2 + B. \tag{3.12}$$

Notably, the integral in the last equation matches the definition of the moment-generating function of a real-valued random variable. Then, the integral in Eq. (3.12) can be expressed with a cumulants series expansion as: [51, 57]

$$\int_0^\infty \exp(-\Gamma\tau) G(\Gamma) d\Gamma = \exp\left(-\langle\Gamma\rangle\tau + \frac{1}{2}\kappa_2\tau^2 - \frac{1}{3}\kappa_3\tau^3 + \cdots\right), \tag{3.13}$$

where $\langle\Gamma\rangle$ is the first cumulant and describes the average decay rate of the distribution, κ_2 is the second cumulant and gives the variance of the distribution, and κ_3 is the third cumulant and provides

a measure of the skewness of the distribution. In this dissertation, we use a second-order cumulant expansion. Finally, the autocorrelation of scattering intensity measured in DLS experiments can be used to fit the next model: [57]

$$g_2(\tau) = \beta \exp\left(-2\langle\Gamma\rangle\tau\right)\left(1 + \frac{\mu_2}{2}\tau^2\right)^2 + B. \tag{3.14}$$

3.2.2 Sample preparation and experiment calibration

In this dissertation, the following experimental protocol was followed to carry out a DLS study:

1. **Sample preparation.** As in SLS experiments, a dilute suspension with a solid concentration of 0.005% w/w in filtered deionized (DI) water is prepared in a cylindrical NMR Pyrex cuvette.

2. **Measurement of the scattering intensity of the diluted suspension.** The DLS experiment is conducted at a controlled temperature over a scattering angle range from 60° to 120°, in steps of 5°. At each scattering angle, 120-second scattering intensity measurements are taken until the entire angular range is covered. The DAQ system automatically performs the autocorrelation of the measured scattering intensity data, so the result for each measurement angle is its corresponding $g_2(\tau)$.

3. **Estimation of the size particle.** We use the Frisken cumulant model, given in Eq. (3.14), to fit the DLS data. One of the fit parameters is the baseline B. The LS Instruments software reports $g_2(\tau) - 1$, implicitly assuming a baseline of $B = 1$. Therefore, we add 1 to the data exported from the LS Instruments software before analysis. The processed data are then imported into OriginPro 9, a software package specialized in scientific data analysis. Using the nonlinear fitting tools in OriginPro 9, the imported data are fit to Eq. (3.14).

   Subsequently, $\langle\Gamma\rangle$ is plotted against q^2, and a linear model is applied. The slope of this fit corresponds to the diffusion coefficient D. Finally, the hydrodynamic radius is estimated using the Stokes-Einstein relation, Eq. (3.10). Since $\langle\Gamma\rangle = \langle D\rangle q^2$, it is also possible to compute the hydrodynamic radius for each scattering angle and report the mean hydrodynamic radius.

   The polydispersity index (PDI) is estimated as the ratio of the second cumulant to the first cumulant in Eq. (3.14), i.e., the second cumulant divided by $\langle\Gamma\rangle$. The PDI provides a measure of the heterogeneity in the sample's hydrodynamic radius. As a general guideline, PDI $<$ 0.05 indicates a highly monodisperse system, $0.05 \leq$ PDI < 0.1 corresponds to a narrow distribution, and PDI ≥ 0.1 denotes a polydisperse system [58].

In DLS experiments, the solvent must be appropriately filtered; otherwise, the autocorrelation of the scattering intensity could present an intermediate plateau due to impurities like dust, which

would prevent the data from being analyzed with the cumulant model given in Eq. (3.14). Suppose the solvent of the colloidal suspension was correctly filtered, but there are one or more intermediate plateaus in the autocorrelation of the scattering intensity data. In that case, it is an unequivocal sign that there is more than one population of particle sizes or the solvent is a non-Newtonian fluid, so the results cannot be analyzed with the model in Eq. (3.14).

As mentioned, we will use the same LS Instrument device for DLS experiments. Additionally, a DLS experiment on standard monodisperse particles is carried out to ensure that the procedure followed allows the reproduction of the size estimation reported by the manufacturer. For DLS calibration, PS standard particles with 100.2 nm of nominal diameter were used (Bangs Laboratories, Inc.), and the experiment was carried out at a controlled temperature of 291 °K (18.25 °C). Fig. 3.5(a) $g_2(\tau)$ versus delay time τ for the standard sample is shown. Although all the angles mentioned in the above protocol were measured, we only show in Fig. 3.5 the results for scattering angles θ of 60° (black boxes), 90° (red circles) and 120° (blue triangles) to have a clear presentation of the results. The solid lines are the best-fit result for the cumulants model given in Eq. (3.14). Fig. 3.5(b)

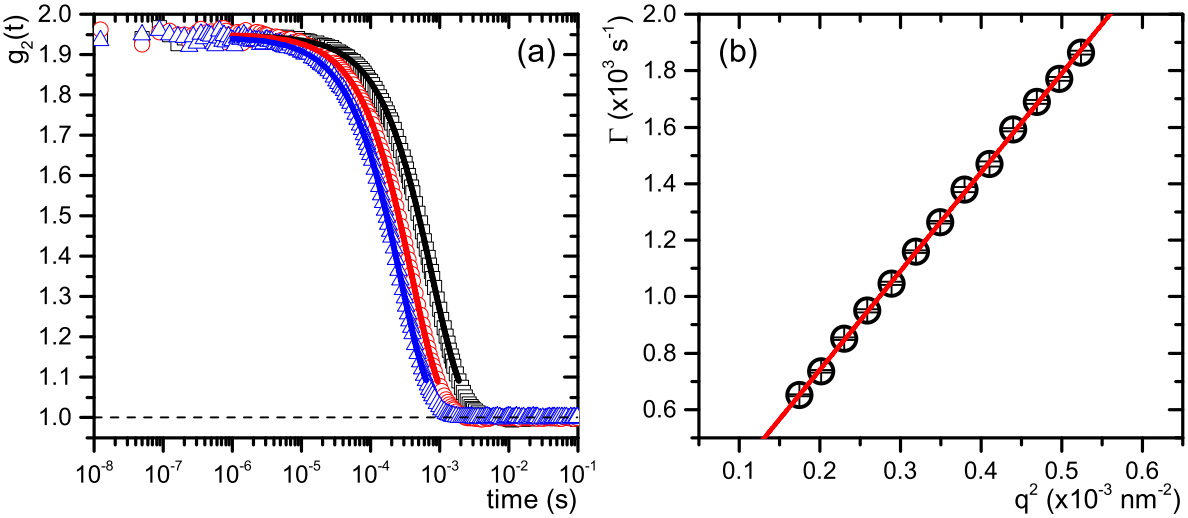

Figure 3.5: (a) Intensity autocorrelation function as a function of time for a diluted suspension of PS standard particles, measured at scattering angles of 60° (black squares), 90° (red circles), and 120° (blue triangles). The solid lines are their second-cumulant fit for the scattering intensity autocorrelation functions, respectively. (b) Inverse of the characteristic decay time Γ as a function of q^2 (black circles) from the DLS experiment at different scattering angles. The red line represents the linear best fit.

shows Γ as a function of q^2 for all the scattering angles described in the protocol above, where $q = (4\pi n_0/\lambda)\sin(\theta/2)$. The data exhibit an excellent linear fit, yielding a diffusion coefficient of $D = 3.49813 \times 10^6 \pm 20082$ nm^2/s. From this value, the hydrodynamic radius is estimated to be $R_h = 58.3 \pm 0.3$ nm.

The percentage deviation from the nominal radius reported by the manufacturer, $R_n = 50.1$ nm,

is calculated as $\Delta\% = (|R_h - R_n|/R_n) \times 100 = 16\%$. Since the hydrodynamic radius is typically larger than the geometric radius, we consider our estimate of R_h and its deviation from the nominal value to be acceptable [59].

Additionally, we estimate a polydispersity index of $\text{PDI} = 0.03 \pm 0.01$, which indicates a highly monodisperse particle size distribution [58], consistent with the manufacturer's specifications. In conclusion, we consider the 3D-DLS device used in this dissertation to be calibrated appropriately.

Chapter 4

Light scattered by spherical PNIPAM microgels

In this chapter, we apply the Mie scattering solution for a multilayer sphere to describe the static light scattering of PNIPAM microgels, demonstrating that its implementation is not impractical as long as the dielectric properties of the microgels are known. For this purpose, we use the experimental data reported by Reufer *et. al.*, [18] who, in turn, used the RGD approximation to analyze their reported data. This allows us to compare the predictive capability of the Mie scattering solution for a multilayer sphere with that of the reported RGD fuzzy sphere approximation.

4.1 PNIPAM refractive index profile model

The PNIPAM microgels don't have a constant cross-link density profile, so it's to be expected that the refractive index (RI) profile will not be either. PNIPAM microgels in water has a core-shell structure, and there's expected to be a higher mass proportion of cross-linked PNIPAM concerning water mass in the dense core region of the microgel, which decreases, according to the fuzzy sphere model, with a Gaussian decay, increasing in the same proportion the water's mass quantity. Some authors suggest that in PNIPAM, the RI profile is proportional to its density cross-links profile, and the shell RI profile could be modeled as: [23]

$$n(r) = (n_c - n_0)\exp\left[-\frac{(r-R_c)^2}{\sigma^2}\right] + n_0, \quad R_c < r \leq R_s, \tag{4.1}$$

with R_c being the core radius with a constant RI, R_s is the shell radius, and n_c and n_0 are the core and solvent refractive indexes, respectively. Although the RI is not necessarily proportional to the density of the microgel, this model has given good results for determining the effective refractive

index of PNIPAM suspensions in water. [23] However, the refractive index profile given in Eq. (4.1) had not previously been used to describe the scattering intensity as a function of the scattering angle for PNIPAM particles until the doctoral research presented in this dissertation.

As was mentioned in sec. 2.2.2, the Mie scattering solution for multilayer spheres can also determine the scattering properties of materials with a continuous radially nonhomogeneous RI profile if some adequate discretization of the sphere is proposed. We discretize the proposed PNIPAM RI profile model in Eq. (4.1) with the first layer $l = 1$, the core, whose size parameter and relative RI is $x_1 = k_0 R_c$ and $m_1 = n_c/n_0$, respectively. The successive $L - 1$ layers are equally spaced as $\Delta x = (R_s - R_c)/(L - 1)$; each layer has a relative RI $m_l = n(\bar{x}_l)/n_0$ where $\bar{x}_l = (x_{l-1} + x_l)/2$ with $x_l = R_c + (l-1)\Delta x$, for $l = 2, \cdots, L-1$. For the last layer, where $x_L = k_0 R_s$, we require that the RI of PNIPAM and the medium almost match. By numerical convenience, we set $m_L = (n_0 + 0.0001)/n_0$. Therefore, with the given R_c, R_s, n_c, and n_0, the value of the Gaussian width σ in Eq. (4.1) can be calculated.

We follow two criteria to choose the L number of layers to discretize Eq. (4.1). The first one considers the accuracy between the scattering intensity curves generated by RI profiles discretized with a large L number of layers (as many layers as the discrete RI profile and the continuous RI profile in Eq. (4.1) are essentially indistinguishable) and that discretized with few layers. The second one considers using a practical computing time which increase with L. For the first criterium, we assume that $L = 500$ layers, as in the Luneburg lens (see sec. 2.2.2), can mimic the continuous case. We measure how different both scattering intensity curves are by the quadratic differences between them as: $\Delta^2 = \sum_i^N [F_{500}(\theta_i) - F_L(\theta_i)]^2$, where $F_{500}(\theta_i)$ is the form factor for the RI profile in Eq. (4.1) discretized with 500 layers and $F_L(\theta_i)$ is the form factor generated by few L number of layers.

In Fig. 4.1(a) is shown, for a monodisperse PNIPAM microgel with $R_c = 290$ nm, $R_s = 437$ nm, $n_c = 1.45$ and $n_0 = 1.332$, Δ^2as a function of L (black squares). We consider that a $\Delta^2 \leq 10^{-3}$ gives enough accuracy between the quasi-continuous RI profile and the RI profile discretized with few layers. Also, in Fig. 4.1(a) is shown Δ^2 for the same PNIPAM microgel but with polydispersity in R_c and R_s, whose polydispersity was set as $\sigma_{g_c} = 1.13$ and $\sigma_{g_s} = 1.01$, respectively, calculated with an without the multi-thread computing module OpenMP (red circles and green asteriscs, respectively). Remember that OpenMP is a module that reduces the computing time in the polydispersity average integrals, so the results achieved with and without OpenMP must be equal. Note that, in monodisperse and polydisperse cases, we can achieve a $\Delta^2 < 10^{-3}$ with $L = 30$.

In Fig. 4.1(b) is shown the computing time for the same cases in Fig. 4.1(a). Observe that for $L = 30$, the computing time in monodisperse and polydisperse calculated with OpenMP cases is below one second. Therefore, we consider $L = 30$ met the two criteria we have established to discretize the RI profile in Eq. (4.1). These parameters were chosen based on the results reported in ref. [18].

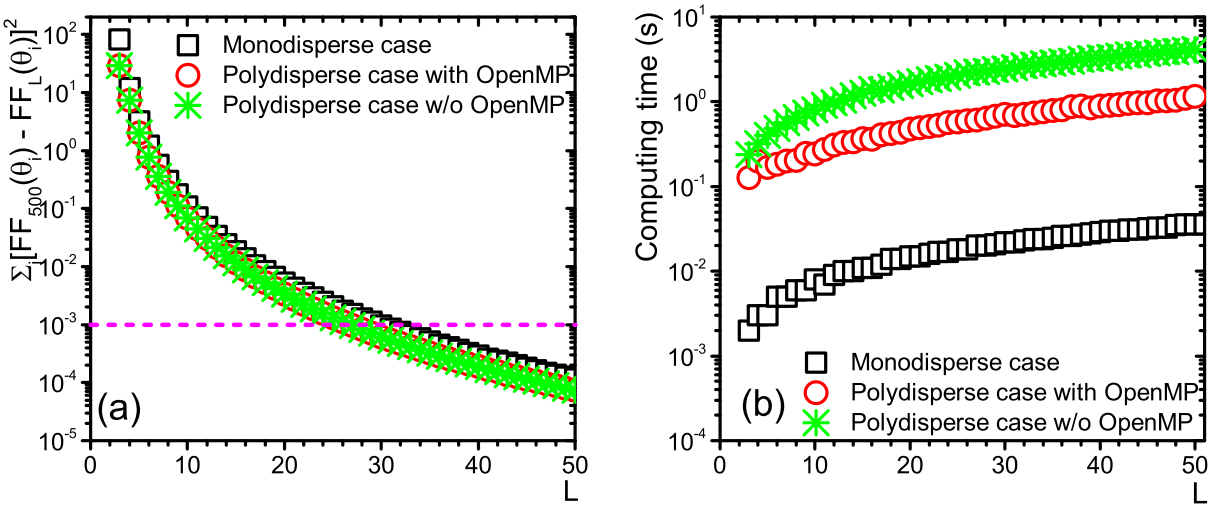

Figure 4.1: (a) Quadratic differences as a function of the number of layers L for monodisperse and polydisperse PNIPAM microgels, with a refractive index profile modeled by Eq. (**??**). (b) Computing time for form factor calculation as a function of L for the same monodisperse and polydisperse PNIPAM microgels shown in (a).

Finally, regarding the discretization of the RI profile model proposed for PNIPAM microgels in the inset of Fig. 4.2, we show the RI profile proposed for a PNIPAM microgel with parameters after mentioned, discretized with three layers, 30 layers, and 500 layers. While the RI profile for 3 and 30 layers is a rough approximation, the RI profile for 500 layers approximation is almost a smooth curve. Fig. 4.2 shows the form factors for the three cases, which are similar despite the roughness approximation with 3 and 30 layers. Notably, the form factors for the 30- and 500-layer approximation are essentially the same. Therefore, we consider a 30-layer discretization an excellent approximation of the continuous case.

4.2 Fitting numerical scheme

To assess the PNIPAM refractive index (RI) profile model using the Mie scattering solution for a multilayer sphere, we fit the calculated scattering intensities to experimental data as a function of the scattering angle using least-squares minimization. Our numerical method requires eight parameters: λ, n_0, R_h, R_c, n_c, σ_{g_c}, R_s, and σ_{g_s}, where σ_{g_c} and σ_{g_s} are the geometric standard deviations of the core and shell radii, respectively. Among these, n_0, R_h, and λ are fixed parameters defined by the scattering experiment.

The numerical method proceeds through the following steps:

1. Read the input experimental variables: λ, n_0, R_h, and other system-specific parameters,

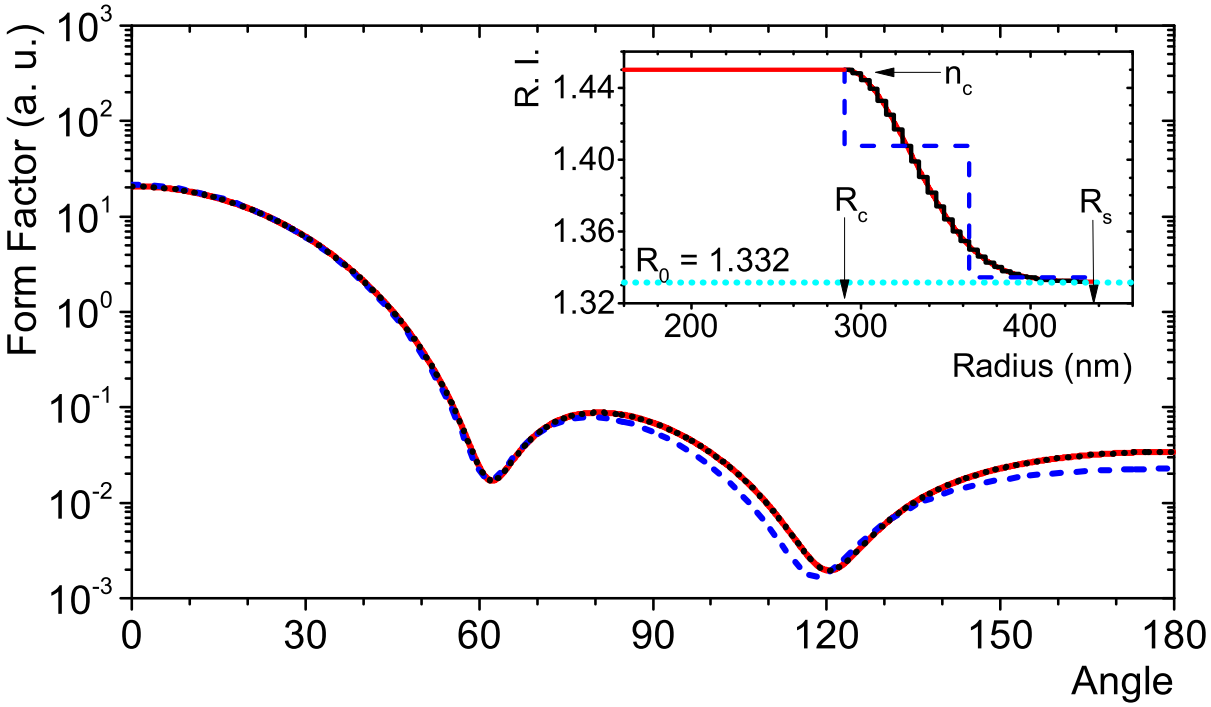

Figure 4.2: Form factor function for a mesoscopic particle (Diam. $= 2R_s > \lambda$) vs angle for the three radial RI profiles given in the inset. The core RI is the same in all the cases. Inset: radial RI profile model for a PNIPAM microgram approximated as a multilayer sphere with three layers (dashed blue line), 30 layers (dotted black line), and 500 layers (solid red line).

namely R_c and n_c, along with the number of layers L used to define the multilayer sphere.

2. Read the experimental scattering intensity data, provided as a table with three columns: angle in degrees θ_i, intensity in arbitrary units $I(\theta_i)$, and the experimental standard error α_i.

3. Perform the numerical fitting procedure. We implement an iterative grid search method using nested loops to minimize the chi-square goodness-of-fit parameter, $\chi^2 = \sum_i (y_i - \hat{y}_i)^2/\alpha_i^2$, where y_i and $\hat{y}_i$ represent the experimental and calculated values, respectively. The calculated quantities (indicated with a circumflex) are derived from the fitting parameters. For each scattering angle θ_i, we compute the form factor $\hat{F}(\theta_i)$ or $|\hat{S}_1(\theta_i)|^2$, depending on the polarization setup, using the Mie scattering solution for a multilayer sphere as described in Section 2.2.1. For each set of trial values within the search intervals of R_c, n_c, R_s, σ_{g_c}, and σ_{g_s}, the algorithm performs the following steps:

   (a) Compute the Gaussian decay width σ in Eq. (**??**) and generate a discretized RI profile table with L entries.

(b) Calculate $\hat{F}(\theta_i)$ or $|\hat{S}_1(\theta_i)|^2$ using Yang's algorithm for the monodisperse case (see Section 2.2.1) or the size-polydispersity algorithm (see Section 2.3.1).

(c) Evaluate χ^2 and update the minimum value χ^2_{min} whenever a lower value is found.

(d) Continue iterating through the parameter space, scanning all values of n_c for a given R_c, then all values of R_s for each n_c, and so on, until all combinations within the R_c interval have been evaluated.

The set of parameters corresponding to the minimum χ^2 defines the best-fit solution. Since the grid search method may converge slowly, we rely on prior knowledge of the system, such as the hydrodynamic radius or the bulk refractive index of PNIPAM, to define appropriate search intervals. Otherwise, the computation time increases considerably.

4.3 Results and discussion

As mentioned earlier, some authors suggest that the PNIPAM RI profile could be modeled by Eq. (4.1). Nevertheless, although the proposed RI profile was successfully compared with effective refractive index measurements of PNIPAM microgel suspensions in water, it had not been previously validated by fitting scattering intensity data as a function of the scattering angle for PNIPAM microgels. To this end, we will use the experimental data reported by Reufer *et. al.*. [18] These authors studied the light scattering of PNIPAM microgel suspension in water over a temperature range of 10 °C $\leq T \leq$ 40 °C, and the SLS results are shown in Fig. 4.3. Also, they used a red light beam (λ = 680.4 nm) without specifying its polarization, so we will consider that the experiment uses unpolarized light. They synthesized their PNIPAM microgels by free radical cross-linking polymerization of NIPAM with MBA using potassium persulfate (KPS) as the polymerization initiator. The hydrodynamic radius R_h reported by the authors is presented in Table 4.1.

Reufer *et. al.* ranged the size of particles from 468 nm at 10 °C (swollen state) to 271 nm at 40 °C (shrunk state). Note that the size of the particles is typically in the Mie scattering regime. However, they used the RGD fuzzy sphere approximation to fit the experimental scattering intensity to estimate the fuzzy sphere parameters. They argued that the RGD approximation is valid because the particles have a large amount of water inside them, making the optical contrast of the particles with the water within the RGD approximation's validity conditions. These fits are also shown in Fig. 4.3. We can observe in Fig. 4.3 that the RGD approximation fits the experimental data with an acceptable agreement for temperatures below LCST, reproducing the first form factor minimum in all cases but not for the second minimum. For temperatures above LCST, the RGD approximation fit is far from the experimental scattering intensities. The authors admit that particles at a temperature higher than the LCST (in a shrunk state) must have a high enough optical contrast with water

not to meet the validity conditions of the RGD approximation. Also, the authors consider that PNIPAM microgels in a shrunk state are like homogeneous spheres. They used the Mie scattering solution for a homogeneous sphere to fit the experimental data for 35 and 40 °C (cyan dash-dot line), which allowed them to estimate the RI of the particles at these temperatures at $n_p = 1.46$. In all cases, they estimated a size polydispersity of 9.5%, but they did not mention the PDF used. All the best-fit parameters estimated by the authors are summarized in Table 4.1.

Our results, shown in Fig. 4.3, correspond to fits of the same experimental data provided by Reufer *et al.* To perform these fits, we require the proportionality constant κ in the relationship $I_T(\theta) \propto F(\theta)$ for each case, which depends on specific experimental details of the measurement setup. Since the authors did not report the value of κ, we implemented two different fitting routines to align our calculated form factors with the experimental data. We refer to these approaches as Multilayer Sphere Approximations (MSAs).

In the first routine (MSA1), we estimate κ as the average of the ratios at the first and last experimental angles: $\kappa = 0.5\left[\frac{I(\theta_1)}{\hat{F}(\theta_1)} + \frac{I(\theta_N)}{\hat{F}(\theta_N)}\right]$, where θ_1 and θ_N are the first and last experimental angles, and $\hat{F}(\theta_i)$ and $I(\theta_i)$ are the calculated form factor and the experimental intensity, respectively.

In the second routine (MSA2), we estimate κ as the average over all data points: $\kappa = \frac{1}{N}\sum_{i=1}^{N}\left[\frac{I(\theta_i)}{\hat{F}(\theta_i)}\right]$. In both cases, the predicted scattering intensity is calculated as $\hat{I}(\theta_i) = \kappa\hat{F}(\theta_i)$. It is important to note that the MSA1 routine is a relaxed version of MSA2, and we apply it in cases where the experimental data are particularly noisy.

We minimize the chi-square goodness-of-fit parameter, χ^2, to determine the best-fit model parameters for both MSA1 and MSA2, using the numerical scheme described in Section 4.2. For the core refractive index, we set the fitting range between 1.332 (the RI of water) and 1.46 (the expected maximum in the collapsed state). For the core and shell radii, we set an upper limit equal to the hydrodynamic radius reported by Reufer *et al.* (see Table 4.1) [18].

The polydispersity parameters are constrained to avoid overlap, such that $R_c < R_s$. The step sizes used in the fitting procedure are $\Delta R_c = \Delta R_s = 1$ nm for the radii, $\Delta n_c = 0.01$ for the core refractive index, and $\Delta\sigma_c = \Delta\sigma_s = 0.01$ for the polydispersity parameters. The resulting best-fit parameters obtained from the MSA1 and MSA2 routines are presented in Table 4.1.

Fig. 4.3 shows the results for both MSA1 and MSA2 fit from 10 to 40 °C. MSA1 and MSA2 present an excellent agreement up to 30 °C. MSA1 at 10 and 20 °C slightly shifts the first form factor minimum to small angles, whereas MSA2 replicates the first form factor minimum very well but not the second minimum. This may be due to a deficient weighted error evaluation of the experimental points at high scattering angles with smaller intensity values. MSA1 and MSA2 produce better fits than RGD approximation because RGD cannot replicate the second form factor minimum. MSA1 and MSA2 fit at 25 °C are very similar and give a better description of the experimental data than RGD approximation. At 30 °C, MSA1, MSA2, and RGD approximation fits are practically the same.

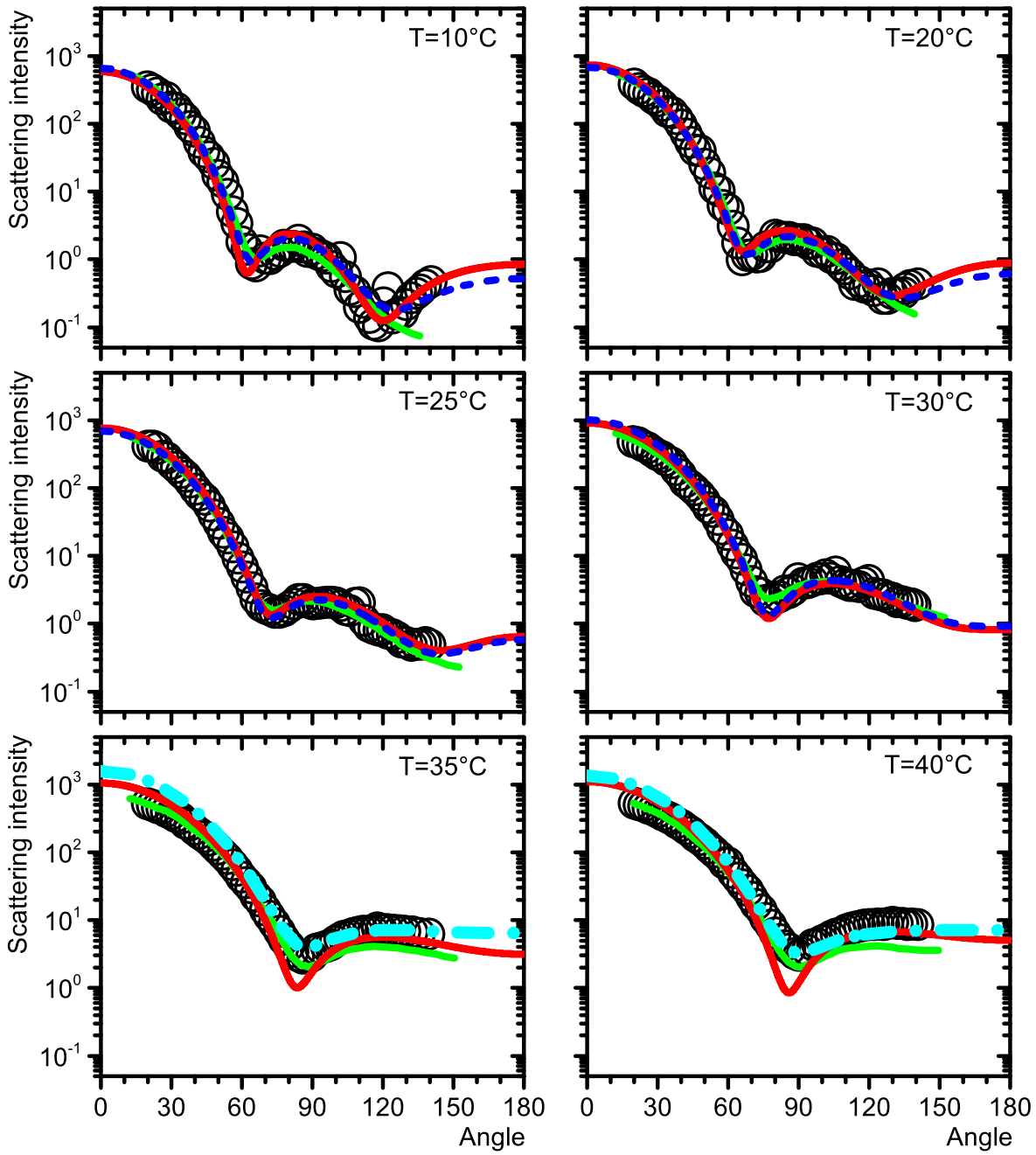

Figure 4.3: Scattering intensity (arbitrary units) vs scattering angle (degrees). Experimental temperature-dependent scattering intensities as a function of scattering angles (circles from ref. [18]). The best fit for MSA1 and MSA2 is represented by the solid red lines and blue dashed lines, respectively, up to 40 °C. At 35 and 40 °C, HSPH fit is indicated by the cyan dashed-dotted lines. Regarding ref [18], in solid green lines, RGD approximation fit with a polydispersity of 9.5% is indicated.

Reufer *et. al.* mentioned this is a limit case because even a homogeneous sphere fit can describe the experimental data well but underestimate the microgel radius.

At 35 and 40 °C, the PNIPAM refractive index profile model given by Eq. (4.1), combined with our polydispersity model, fails to accurately describe the experimental data. In this temperature range, the microgel is in a collapsed state and behaves like a solid, homogeneous sphere. Consequently, above the lower critical solution temperature (LCST), the PNIPAM microgel can no longer be accurately described as a core-shell particle with a fuzzy shell using the complete model employed in this dissertation, that is, the refractive index profile given by Eq. (4.1) combined with a polydispersity model in which the core and shell polydispersities are treated independently. As a future direction, it would be valuable to explore how variations in parameters such as core and shell polydispersity influence the form factor. Above the LCST, the Mie scattering solution for a homogeneous sphere provides a more appropriate model for describing the scattering behavior of the microgel. However, even this model exhibits deviations from the experimental data, as shown in Fig. 4.3 [18, 21].

Fig. 4.4(a) shows the radial refractive index profiles obtained from the MSA1 fits presented in Table 4.1, and Fig. 4.4(b) displays a comparison between the measured and fitted particle radii using different theoretical methods. At 10 °C, the fitted refractive index of the microgel core is $n_c = 1.44$. For temperatures above 10 °C, the fitted core refractive index remains nearly constant at $n_c = 1.46$. This latter value coincides with the maximum estimated refractive index reported by Reufer *et al.* [18]. These results suggest that the core of the PNIPAM microgel retains approximately the same amount of water in the swollen state, even as the suspension approaches the LCST. In future work, it will be important to investigate why our refractive index results do not show a monotonic trend.

Table 4.1: Parameters obtained using different approximation parameters for the best-fit values using MSA1 and MSA2, as well as the results by ref. [18] for experimental hydrodynamic radius R_h^e as a function of temperature T and their best-fit parameters using RGD approximation. All the radius values are in nanometers, the temperature in °C, and κ in arbitrary units.

		RGD	MSA1						MSA2					
T	R_h^e	R	R_c	n_c	σ_c	R_s	σ_s	κ	R_c	n_c	σ_c	R_s	σ_s	κ
10	468	335	292	1.44	1.13	432	1.01	33.09	255	1.44	1.13	468	1.01	42.46
20	433	321	257	1.46	1.13	433	1.00	42.10	242	1.45	1.15	440	1.00	51.29
25	416	308	229	1.46	1.15	415	1.00	69.02	229	1.46	1.15	416	1.00	61.39
30	383	290	242	1.46	1.09	349	1.00	118.04	242	1.46	1.09	349	1.00	131.5
35	299	262	243	1.46	1.05	299	1.00	203.42	242	1.46	1.05	298	1.00	270.6
40	271	257	249	1.46	1.02	271	1.00	623.35	246	1.46	1.05	268	1.00	380.5

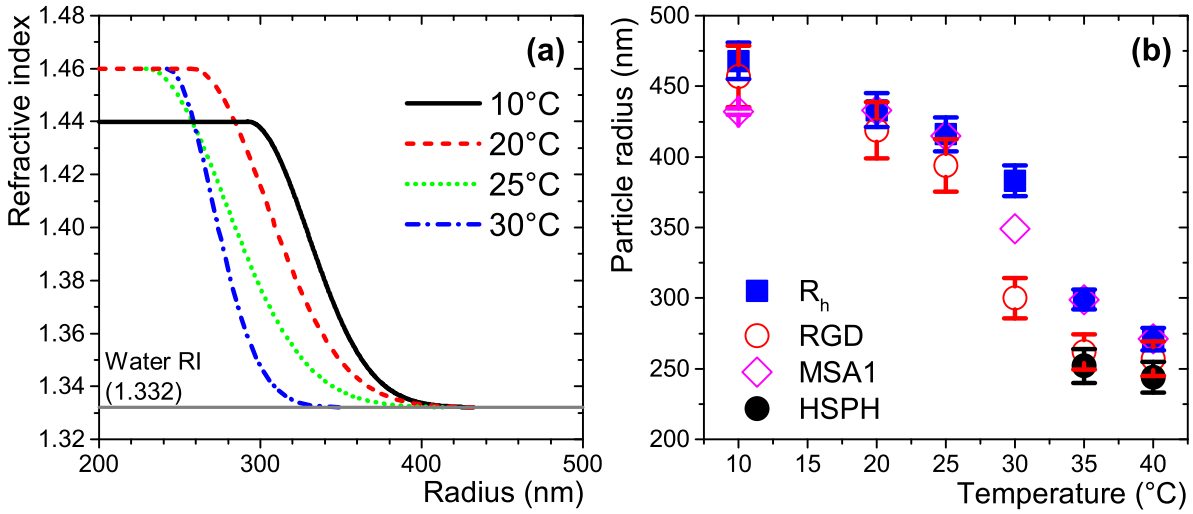

Figure 4.4: (a) Radial refractive index profile of MSA1 fitted for the microgel in the swollen state. (b) Comparison of particle hydrodynamics radius (experimental DLS data in blue squares) as a function of the temperature with our model predictions. We included the RGD fits from the work by Reufer *et. al.*, [18] and the particle radius from the solid sphere model at 35 and 40 °C.

Fig. 4.4(b) shows that the MSA1 approach slightly underestimates the particle radius at 10°C and 30°C. At other temperatures, the MSA1 fits agree well with the hydrodynamic radius measured by Reufer *et al.*, even for microgels in the collapsed state. An important observation in Fig. 4.4(b) is that, despite the RGD fit showing excellent agreement with the data at 30 °C, it results in a significant error when evaluating the transition temperature between the swollen and collapsed states of the microgel (around 32 °C), with a percentage deviation of 21.7% from R_h. In contrast, the MSA1-fitted radius at 30 °C shows a smaller percentage deviation of 8.9% from R_h. At 35 °C and 40 °C, the HSPH model underestimates the hydrodynamic particle radius, despite providing a better description than the PNIPAM refractive index profile model combined with our polydispersity approach. This suggests that the actual radial refractive index profile in the collapsed state is more complex than a homogeneous profile, or that the polydispersity model requires further refinement.

To the best of our knowledge, this is the first time that the form factor of PNIPAM microgels in the swollen state has been described in the Mie scattering regime using a radial refractive index profile.

Chapter 5

Light scattered by PS/PNIPAM core/shell particles

This chapter presents a comprehensive study of the light scattering properties of PS/PNI- PAM. We begin by describing the synthesis protocol for PS/PNIPAM core/shell particles, carried out via free radical polymerization using AIBN to obtain neutral PNIPAM shells. The resulting particles are characterized through thermal analysis, morphological examination, and measurements of the hydrodynamic radius as a function of temperature. We then analyze the angular-dependent light scattering intensities using the Mie scattering solution for a multilayer sphere, comparing the results with experimental data to evaluate the accuracy of the refractive index profile model in describing the angular-dependent scattering behavior of the synthesized particles. Finally, we extend our analysis to core/shell particles in which the PNIPAM shell is functionalized with acrylic acid (AAc), PS/PNIPAM-co-AAc core/shell particles, and discuss how the refractive index profile model used in this dissertation for PNIPAM microgels may fail to describe the scattering behavior when synthesis conditions are modified.

5.1 Synthesis of PS/PNIPAM core/shell particles

Currently, several reported protocols for synthesizing PNIPAM microgels exist, and one of the most used is the free radical polymerization of NIPAM monomers cross-linked with MBA, where AzobisIsoButyroNitrile (AIBN) is used as the radical initiator. [19, 20] One of the reasons why protocols using AIBN as a radical initiator are preferred is that this route allows the production of neutrally charged PNIPAM microgels. In other reported works, such as the one reported by Reufer *et al.* (see 4.3), [18], potassium persulfate is used as a radical initiator, causing the PNIPAM bearing negatively charged end groups, which must be taken into account depending on the intended

use. [19, 20]

Because AIBN is a hydrophobic reagent, when the polymerization by AIBN radical initiator occurs in water, the growing radical chain becomes insoluble. Also, when a solution of NIPAM and MBA in water is heated to above 70 °C, the NIPAM and MBA molecules in water acquire a hydrophobic character. [19, 20, 60] Therefore, if the polymerization by AIBN radical initiator is carried out in water, a higher concentration of PNIPAM chains is expected in the center of the microgel. [20] In Fig. 5.1, the chemical equation for the free radical polymerization of PNIPAM cross-linked with MBA using AIBN as radicals initiator carried out in water is shown. Note that water doesn't participate in the chemical reaction, and the NIPAM, MBA, and AIBN water solution is heated to 76 °C. [18–20, 23] In the inset of Fig. 5.1 is shown a cartoon of the PNIPAM microgel structure where the MBA cross-linking PNIPAM polymers as steps on a ladder. [19, 20, 61, 62]

On the other hand, several chemical protocols were also reported in the literature to produce core/shell particles where the PNIPAM could be the core or the shell, taking advantage of the physical-chemical properties of the PNIPAM and the complementary material in the core/shell particle. [15–17, 19, 63–67] One of the synthesis' protocol proposal that presents a possible technical advantage for this PhD dissertation is the one reported by Zhu *et al.* [67]

In the protocol of Zhu *et al.*, [67], the synthesis of core/shell particles composed of a solid PolyStyrene (PS) core coated with PNIPAM microgel is reported. To this end, the authors take advantage of the hydrophobic character in the polymerization of PNIPAM described above to coat the PS cores without the need for previous chemical treatment on the PS cores. This is achieved because PS is a hydrophobic polymer. For this reason, the PNIPAM structure that coats the core is expected to decrease in its cross-linking density as a function of the final shell radius. Also, this represents a technical advantage for this dissertation since it's possible to use commercially available PS particles whose size polydispersity is low concerning the nominal size reported by the manufacturer. However, using particles manufactured by a third party could have the disadvantage of not knowing the procedures and reagents in their production of PS particles for reasons of industrial secrecy, which could modify the known general properties of the PS particles. Synthesizing solid particles with low polydispersity could be technically challenging, but the synthesis of polystyrene particles is beyond the scope of this dissertation. Therefore, we have decided to deal with the possible disadvantages of purchasing PS cores manufactured by a third party to synthesize PS/PNIPAM core/shell particles following the protocol reported by Zhu *et al.* [67]

The protocol of Zhu *et al.* can be summarized in three steps. [67] In the first step, AIBN is dissolved in ethanol (EtOH), and then the PS cores are added. AIBN is initially crystalline and can dissolve in organic liquids such as EtOH. A three-neck flask containing degassed DeIonized (DI) water is prepared in the second step. The solution of AIBN and PS cores in EtOH is added, along with NIPAM and MBA, which have been dissolved in degassed DI water from the three-neck flask.

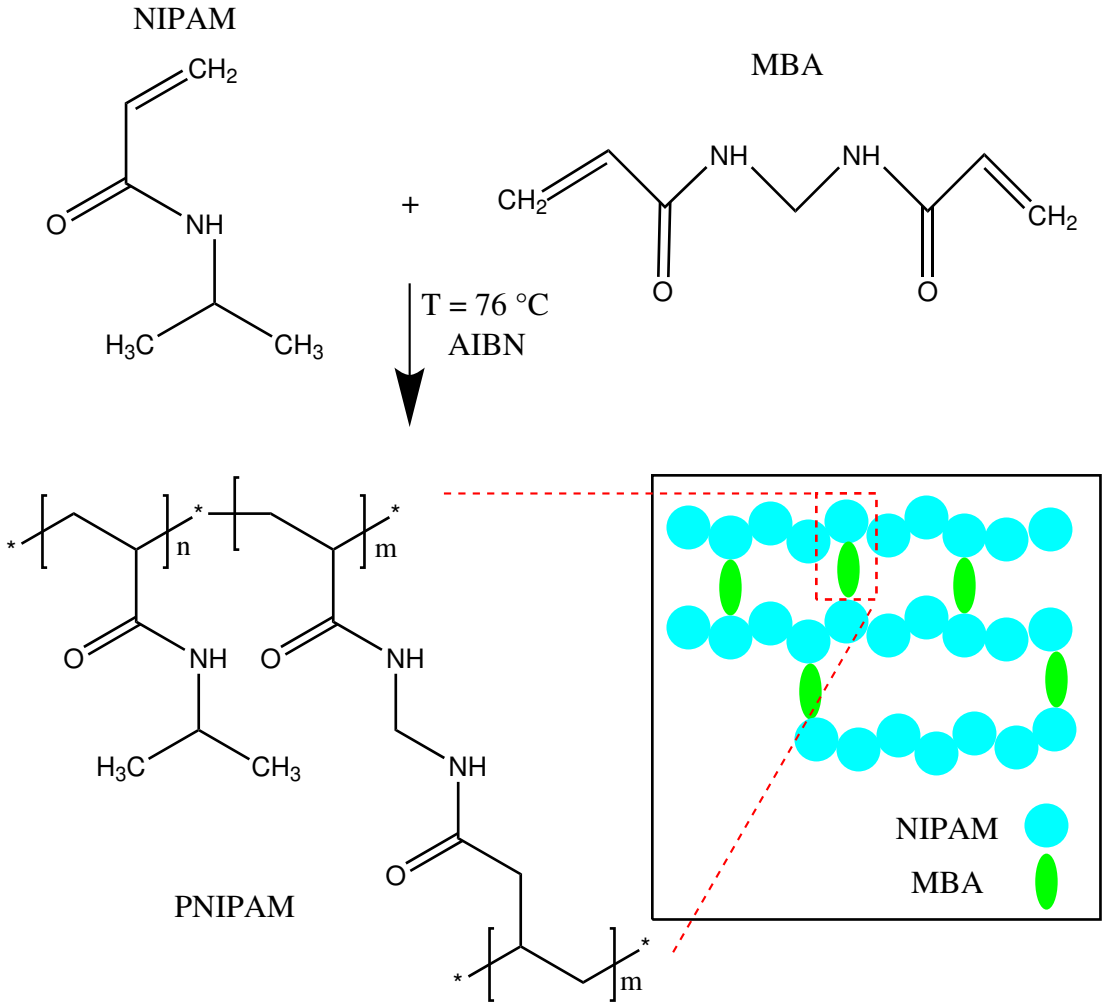

Figure 5.1: Chemical equation for the free radical polymerization of NIPAM monomers cross-linked with MBA, where AIBN is used as radical initiator. Inset: a sketch of PNIPAM microgel structure. The square in red dashed lines encloses a block of the PNIPAM polymer cross-linked with MBA, indicating its corresponding chemical formula in the chemical equation.

At this stage, the dissolved AIBN molecules tend to accumulate in hydrophobic regions within the aqueous medium, specifically around the PS cores, which are also hydrophobic. In the last step, the reaction mixture is heated to a temperature of 76 °C in a N_2 atmosphere with constant stirring. When the temperature exceeds 40 °C, AIBN releases radicals. Above 70 °C, NIPAM and MBA molecules exhibit hydrophobic behavior, preferentially localizing around the PS cores, where AIBN is also concentrated. This facilitates free radical polymerization around the PS cores. Finally, after four hours of reaction at 76 °C, the product is cooled overnight at room temperature with constant stirring. Then, the PS/PNIPAM core/shell particles are cleaned by dialysis and stored. Fig. 5.2

illustrates the main steps followed by Zhu *et al.* to synthesize PS/PNIPAM core/shell particles described above. Additionally, the figure includes red-boxed cartoons depicting reagent molecules' behavior at different synthesis stages.

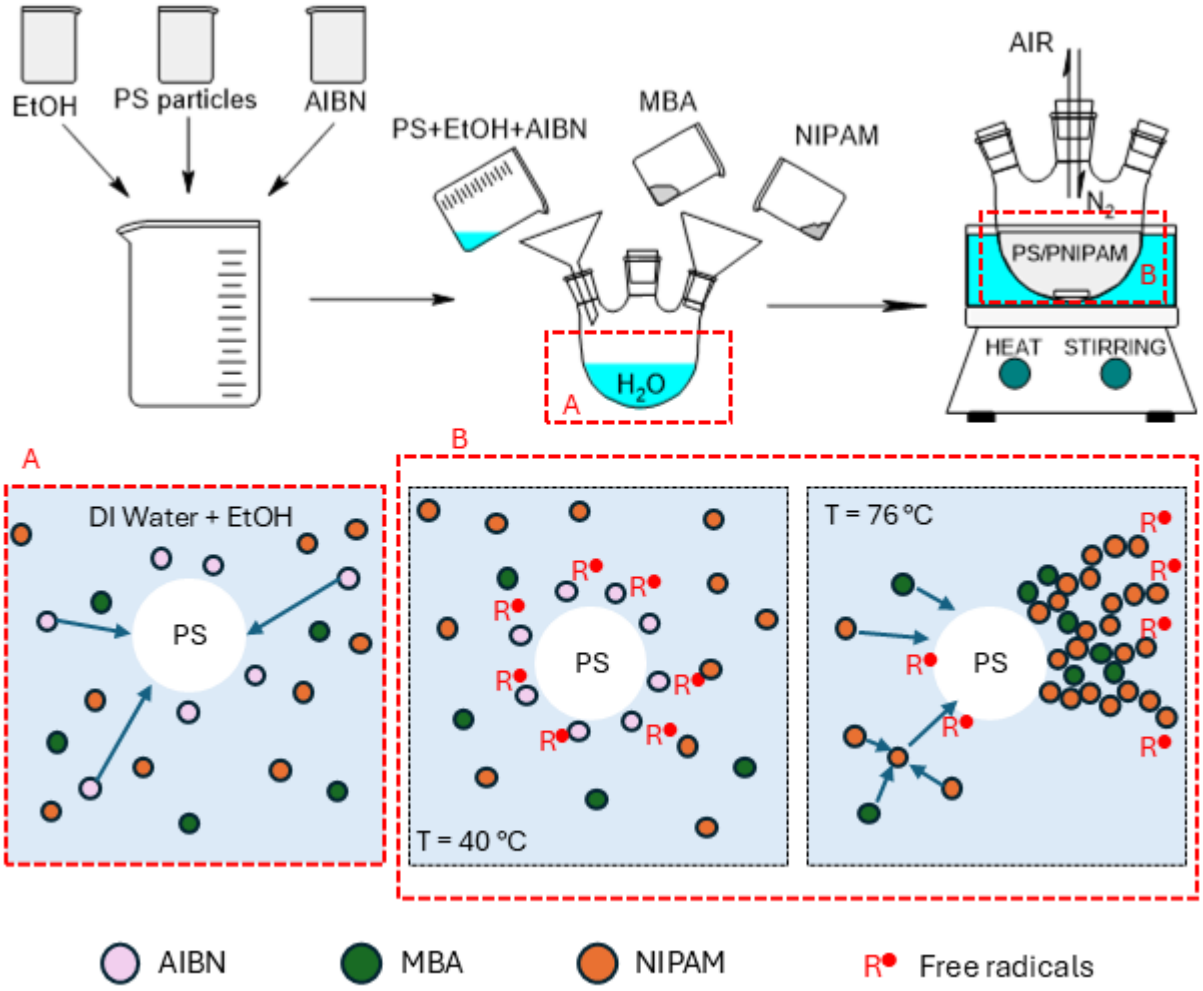

Figure 5.2: Cartoon of the synthesis route followed to produce PS/PNIPAM core/shell particles using the protocol proposed by Zhu *et al.* [67]

In the Zhu *et al.* synthesis, 160 mg of dry PS particles with 210 nm of diameter are mixed with 20 mL of EtOH, dispersing the suspension by sonication for 30 minutes. Then, 10.17 mg of AIBN is added to the PS particle suspension, and the AIBN is dissolved by sonication for 20 minutes. After that, the solution is transferred to a three-neck flask containing 160 mL of degassed DI water, followed by the addition of 702 mg and 96 mg of NIPAM and MBA, respectively.

In our case, to synthesize PS/PNIPAM core/shell particles, we used PS particles with a di-

ameter of 99 nm (10.02% w/w water suspension, Bangs Laboratories Inc.). Also, the reagents were used as received: N-IsoPropylAcrylaMide (NIPAM) ($\geq$ 99%, Sigma-Aldrich, USA); N, N'-MethyleneBis(Acrylamide) (MBA) (99%, Sigma-Aldrich, USA); and AzoBisIsoButyroNitrile [AIBN, 2,2'-Azobis(2-methylpropiNitrile)] (99%, Sigma-Aldrich, USA). Because our PS particles have a different size than the ones of Zhu *et al.*, and the manufacturer supplies PS particles suspended in water with surfactant ($\leq 0.5\%$ in product) and sodium azide ($\leq 0.09\%$ in product) that helps prevent particle aggregation and bacterial growth in the suspension, [68] adapting the Zhu *et al.* protocol to our needs will be necessary.

Due to the difference between the PS cores' size used by Zhu *et al.* concerning the used by ours, it's necessary to change the reagent quantity to use in the synthesis. To this end, we proposed a linear relation between cores' size and shells' size, defined as $R_s = yR_c$ and $R'_s = y'R_c$, where the primed variables correspond to the dimensions of our particles. Therefore, the volume of the PNIPAM shell in both syntheses can be related to the PS core radius as $V_s = (4/3)\pi(y^3 - 1)R_c^3$ and $V'_s = (4/3)\pi(y'^3 - 1)R_c'^3$, respectively. Suppose the NIPAM density in both syntheses is equal between them. In that case, we can relate the number of molecules of NIPAM, (#NIPAM), necessary in our synthesis with the number of molecules of NIPAM used by Zhu *et al.* and with the cores' radii ratio used in each synthesis as $(\#\text{NIPAM}) = (\#\text{NIPAM})'[(y'^3 - 1)R'^3/(y^3 - 1)R_c^3]$. Consequently, if we know the cores' radii and their proportions with the shells' sizes, we can estimate the quantity of reagents for our synthesis.

From work reported by Zhu *et al.*, we can calculate the ratio of the number of molecules of NIPAM over the number of PS particles, (#NIPAM)/(#e_{ps}), in (#NIPAM)/(#e_{ps})=2.138×10^7, and also the ratio of NIPAM with MBA and AIBN in (#NIPAM)/(#MBA)$\sim$ 10 and (#NIPAM)/(#AIBN)$\sim$ 100, respectively. The proportionality constant between the shell and core's size of the PS/PNIPAM particle synthesized by Zhu *et al.* at collapsed state is $y = 4/3$. In our case, we established a proportionality constant between the shell and core size of the PS/PNIPAM particle to synthesize by us in $y' = 3/2$. Thus, we expect a shell 3/2 bigger than our PS cores, that is, $R'_s \approx 75$ nm at collapsed state. The mass amount of reagents used by Zhu *et al.* and by us to synthesize PS/PNIPAM core/shell particles are given in Table 5.1.

Finally, the protocol followed to synthesize our PS/PNIPAM core/shell particles, based on Zhu *et al.* work, [67] consists of the following steps:

1. Cleaning of PS solution by dialysis in DI water. The DI water was changed daily for 2 days. A membrane with MWCO of 300 kDa (pores ~ 11 nm^2) was used. In this step, the additives from the original suspension provided by the manufacturer were removed.

2. AIBN is dissolved in 25 mL of EtOH by sonication for 30 minutes. Ice is used to prevent the AIBN solution from overheating.

3. The cleaned PS particle solution in water is poured into the AIBN solution in EtOH. At this stage, AIBN molecules tend to accumulate around the PS particles.

4. A three-neck round-bottom flask is prepared with 250 mL of DI water. The central neck and one of the side necks are sealed with a septum, while the other side neck is closed with a glass stopper. Then, N_2 is bubbled into the DI water through the side septum, and the air is purged using a needle inserted into the septum in the central neck for 30 minutes at 35 °C under constant stirring.

5. The NIPAM and MBA are weighted and placed in separate flasks. The flasks are sealed with a septum, and the air is replaced with N_2.

6. Using a syringe, degassed water is withdrawn from the three-neck flask and transferred into the flasks containing NIPAM and MBA, with 50 mL added to each flask.

7. The AIBN and PS particles solution in water and EtOH is poured into the three-neck flask containing degassed DI water, and N_2 gas is bubbled into the solution for 15 minutes under constant stirring. Then, the side neck is sealed with a septum.

8. The solutions of NIPAM and MBA are withdrawn into a syringe and poured into the three-neck flask containing the AIBN and PS particles solution under an N_2 atmosphere.

9. The final solution is heated to 76 °C under constant stirring. The needle used to purge the air is sealed with a balloon filled with N_2. The reaction is maintained at a constant temperature for 4 hours.

Table 5.1: The mass amount of reagents used by Zhu *et al.* and by us to synthesize PS/PNIPAM core/shell particles. Also, the reagents' molecular mass M is reported.

Zhu *et al.* synthesis			
PS cores	NIPAM	MBA	AIBN
$R_c = 105$ nm	$M = 113.16$ g/mol	$M = 154.17$ g/mol	$M = 164.21$ g/mol
$m = 160$ mg	$m = 702$ mg	$m = 96$ mg	$m = 10.72$ mg
$\#e_{PS} = 3.14 \times 10^{13}$	$\#NIPAM = 3.736 \times 10^{21}$	$\#MBA = 3.75 \times 10^{20}$	$\#AIBN = 3.931 \times 10^{19}$
In our synthesis			
PS cores[a]	NIPAM	MBA	AIBN
$R_c = 49.5$ nm	$M = 113.16$ g/mol	$M = 154.17$ g/mol	$M = 164.21$ g/mol
$m = 209.6$ mg	$m = 1584.2$ mg	$m = 215.0$ mg	$m = 22.9$ mg
$\#e_{PS} = 3.93 \times 10^{14}$	$\#NIPAM = 8.402 \times 10^{21}$	$\#MBA = 8.405 \times 10^{20}$	$\#AIBN = 8.402 \times 10^{19}$

[a] Mass of PS suspension at 10.02% w/w of water.

10. Allow the reaction to cool overnight at room temperature.

11. The final product is evaporated under reduced pressure until the volume is approximately 30 mL. At this stage, the EtOH is removed from the product.

12. The evaporated product is cleaned by dialysis with DI water. The DI water was changed daily for 4 days. In this stage, the product is purified from AIBN and the remnants of reagents that did not participate in the polymerization.

13. The product is characterized and stored in a glass flask with a Teflon seal. It is kept under refrigeration to prevent the evaporation of water in the product.

5.2 PS/PNIPAM core/shell particles characterization

In this section, we discuss the characterization of the particles we synthesized. The PS/PNIPAM core/shell particle suspension was characterized in terms of thermal degradation, morphology, and hydrodynamic size as a function of temperature.

In thermal degradation characterization, the sample mass is measured as a function of the temperature. This technique is also known as Thermo-Gravimetric Analysis (TGA). In TGA equipment, the sample is heated under controlled atmosphere conditions, where temperature ramps are typically applied at a rate of 10 to 20 °C/min, depending on the suspected properties of the sample. The sample is placed in a pan attached to a scale in a furnace. The pan is usually made of platinum. A TGA for suspensions determines the mass content of particles within suspension. If the particles are composed of materials that degrade at different and well-determined temperatures, it is possible to quantify the materials' mass concentration that constitutes the particles. In our case, we determined the concentration of PS/PNIPAM particles in the suspension obtained from the synthesis described in the previous section and the concentration of PNIPAM and PS in the suspension. For this purpose, we used a ThermoGravimetric Analyzer TGA-Q500 by TS Instruments Inc. The analysis was carried out under a N_2 atmosphere, and we used a temperature ramp from room temperature to 600 °C with a rate of 10 °C/min.

Fig. 5.3(a) shows the TGA curve as a function of temperature for the PS solution used in the synthesis of our PS/PNIPAM particles. The measurement is presented as the absolute weight percentage of the sample (black solid-line). Also is shown the Weight Derivative (WD) against temperature (blue solid-line). Two key features can be observed. The first one corresponds to a total mass loss of 89.33% from room temperature to 150 °C. In this stage, all liquid solvents, including water, are evaporated. Therefore, by drying the sample, we determined the mass concentration of PS particles in the original suspension provided by the manufacturer to be 10.67% w/w in water. In the second feature, a mass loss is observed from $\sim$ 400 to 450 °C, corresponding to PS degradation

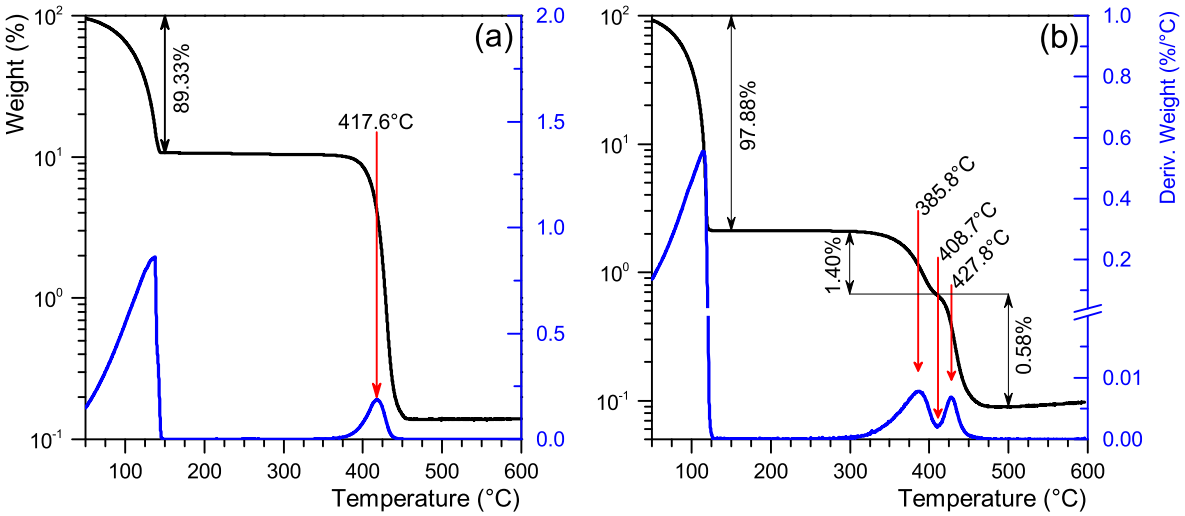

Figure 5.3: Weight percentage as a function of temperature (black solid-line) and weight derivative against the temperature (blue solid line) for: (a) PS particles from the original suspension provided by the manufacturer, and (b) PS/PNIPAM core/shell particles synthesized by us.

into ashes. From the WD curve, we can estimate that the maximum mass loss rate in PS degradation is at 417.6 °C. Our result is consistent with those reported in the literature. [69]

Fig. **??**(b) shows the TGA curve as a function of temperature for the PS/PNIPAM particles synthesized in this work, presented as the absolute weight percentage of the sample (black solid line) and the weight loss derivative with respect to temperature (blue solid line). Three thermal degradation events are observed. In the first stage, similar to the TGA result for the PS solution in Fig. 5.3(a), all solvents are evaporated. From this, by drying, we estimate the mass concentration of the synthesized PS/PNIPAM particles to be 2.12% w/w in water.

The second and third degradation events are identified by their respective peaks in the derivative weight loss curve. We assume that the minimum between these two peaks marks the transition from PNIPAM to PS thermal degradation. The second thermal degradation occurs approximately between 300 and 408.7°C, with a maximum mass loss rate at 385.8°C, which we associate with the thermal degradation of PNIPAM. [70] The third degradation event is observed between 408.7 and 470°C, with a maximum mass loss rate at 427.8°C, corresponding to PS decomposition. [69] Based on these results, we estimate the mass concentrations of PNIPAM and PS in the sample to be 1.40% and 0.58% w/w in water, respectively. From the TGA analysis, we conclude that our synthesized product contains both PNIPAM and PS in the concentrations stated above.

Since TGA analysis of our synthesized product cannot confirm if the PNIPAM coats PS particles, a direct imaging technique is required to determine if the synthesis successfully produced

PS/PNIPAM core/shell particles. To this end, we used a Scanning Electron Microscopy (SEM) at the Central Laboratory of Microscopy of the Institute of Physics, National Autonomous University in Mexico. The sample was prepared with a dilution of 1:1000 and dried at room temperature. The SEM facility is equipped with a JEOL JSM-7800 microscope.

Fig. 5.4(a) shows a micrograph of PS particles, where the cores exhibit a well-defined circular morphology. In Fig. 5.4(b), a micrograph of our synthesized particles is shown, where they depict a rough surface. The inset in Fig. 5.4(b) presents a zoomed-in micrograph of one of the synthesized particles in Fig. 5.4, where we can observe that the synthesized particles have a well-defined core/shell structure. The core is measure with a diameter of 99.7 nm, while the shell has a thickness of 38.8 nm. Thus, the PS/PNIPAM particle in the micrograph has total radius of 69.2 nm at fully collapsed state. This size is very similar to the expected value based on our reagents estimation in sec. 5.1. From the micrographs, we can conclude that our synthesized particles are indeed core/shell particles.

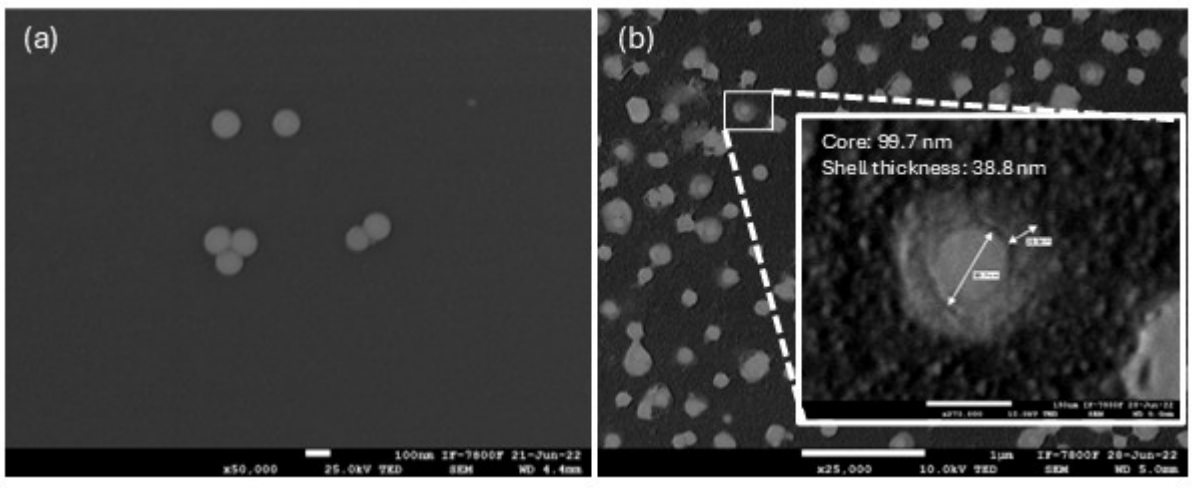

Figure 5.4: Scanning electron microscopy micrographs. (a) Micrograph of PS particles. (b) Micrograph of our synthetized PS/PNIPAM core/shell particles. Inset: a zoomed-in view of a single PS/PNIPAM particle.

Finally, we measured the hydrodynamic radius as a function of temperature T, $R_h^{\mathrm{DLS}}(T)$, of our PS/PNIPAM particles in water suspension, where it's expected to be larger than that measured by SEM, as the particles are dry in the latter case. In the suspension, the PNIPAM structure retains water even above the LCST. [19, 60] To determine the particle size in the suspension, we use the Dynamic Light Scattering (DLS) technique, following the protocol described in chap. 3. Using a previously calibrated chiller, the temperature of the scattering chamber is set at 10, 15, 20, 25, 30, 32, 35, and 40 °C. In all cases, the scattering chamber was allowed to thermalize for one hour before

starting the DLS measurements. DLS measurements were performed from the lowest temperature (10 °C) to the highest (40 °C). In Fig. 5.5, R_h is shown as a temperature function. As expected, R_h decreases with increasing temperature. Below LCST ($\sim$ 32 °C) PNIPAM is swollen, whereas above LCST, it transitions to a shrunk state.

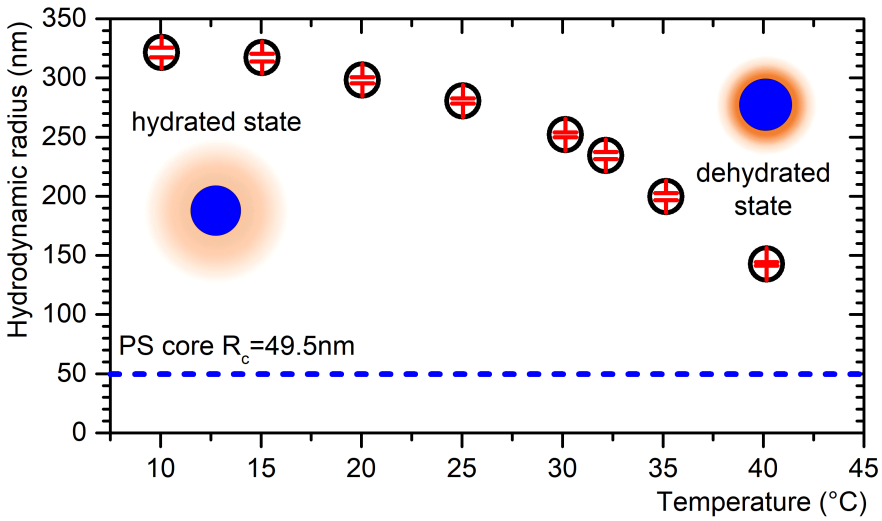

Figure 5.5: Hydrodynamic radius as a function of temperature for a PS/PNIPAM core/shell particle suspension in water (black circles). In the red bars, the standard error in the sizing is shown. Also, it shows the PS core radius in a blue dashed line.

The hydrodynamic radius R_h^{DLS} as a function of temperature T and its respective polydispersity index (PDI) is shown in Table 5.2. We can observe that the PDI below temperatures of 32 °C is greater than 0.1. Thus, for our PS/PNIPAM particles, below the LCST, the particle size distribution is polydisperse. On the contrary, the PDI from and above 32 °C is less than 0.02. Therefore, for our particles, above the LCST, the particle size distribution is highly monodisperse.

Table 5.2: Hydrodynamic radius measured by DLS, R_h^{DLS} at different scattering chamber temperature T. The hydrodynamic radius is in nanometers, the temperature is in °C, and the polydispersity index (PDI) is dimensionless.

T	R_h^{DLS}	PDI	T	R_h^{DLS}	PDI
10	321.6 ± 0.2	0.192 ± 0.041	30	252.0 ± 0.2	0.131 ± 0.026
15	317.2 ± 0.2	0.235 ± 0.032	32	234.4 ± 0.2	0.005 ± 0.005
20	298.0 ± 0.2	0.193 ± 0.022	35	199.6 ± 0.2	0.002 ± 0.002
25	280.6 ± 0.2	0.164 ± 0.031	40	159.5 ± 3.4	0.002 ± 0.002

From all the characterization results described in this section, we can conclude that the synthesis protocol produced well-defined spherical PS/PNIPAM core/shell particles, where the PNIPAM

coating exhibits the expected thermo-responsive behavior below and above the LCST. Also, our synthesized particles are polydisperse below the LCST and highly monodisperse above the LCST.

5.3 Results and discussion

Fig. 5.6(a) shows our experimental scattering intensities vs scattering angles for PS plain standard particles with mean diameter = 100 nm (Bangs Laboratories, Inc. USA) (black squares), showing that the calibration of our SLS device is correct. It also indicates PS/PNIPAM core/shell particles at 20 °C (blue circles) and 40 °C (red triangles) synthesized by us. At small scattering angles, we can observe that PS/PNIPAM core/shell particles scatter around one order of magnitude more than PS plain standard particles, even though PS plain standard particles and the core of PS/PNIPAM particles have a very close size. To fit the experimental scattering data shown in Fig. 5.6(a), we use a similar procedure to MSA2 because it presents a low experimental noise. This allows us to estimate κ rigorously without any data masking. Considering that scattering intensities are measured in vertical polarization setup, the proportionally constant κ is calculated as an average of all the experimental points ratios with $|\hat{S}_1(\theta)|^2$, *i.e.*, $\kappa = (1/N)\sum_{i=1}^{N}[I_s(\theta_i)/|\hat{S}_1(\theta_i)|^2]$, where the scattering amplitude, $|\hat{S}_1(\theta)|^2$, is given in Eq. (2.13) and is calculated as a homogeneous sphere or multilayer sphere, as appropriate. Therefore, in both cases, the predicted scattering intensity for our model would be $\hat{I}(\theta_i) = \kappa|\hat{S}_1(\theta_i)|^2$, and we will name these routines HSPH and MSA3, respectively.

We consider the PS/PNIPAM particles to have a monodisperse PS core with a homogeneous refractive index (RI), $n_{PSc} = 1.59$. The nominal core radius, $R_{PSc} = 49.5$ nm, is taken from the manufacturer's specifications. The RI of the PNIPAM shell is approximated using the refractive index profile model given in Eq. (4.1). In the multilayered sphere approximation, the parameters obtained from the best fit are the thickness and RI of the PNIPAM plateau region in the shell, denoted as T_{PP} and n_{PP}, respectively, as well as the overall shell radius R_s, and the polydispersity of both the PNIPAM plateau region, σ_{PS}, and the full shell, σ_S (see inset in Fig. **??**(a)).

Following the same procedure used to determine the number of layers for discretizing the RI profile, we choose a discretization with $L = 12$ layers, which provides a good balance between the precision of the form factor estimation and the computational cost of its calculation. The first layer represents the PS core, the second corresponds to the RI plateau, and the remaining ten layers are used to model the Gaussian decay in the refractive index profile.

To fit the experimental data of PS plain standard particles, we used the SSPH routine. We set the hydrodynamics radius provided by DLS as an upper search limit value for the particle radius. For PS/PNIPAM particles, to save computing time, we first fit the PS/PNIPAM experimental data for 40 °C, whose results allow us to set the search limits for PS/PNIPAM at 20 °C because at 40 °C, the PNIPAM shell is shrunk, and a large amount of water is expelled. Hence, at 40 °C, the PNIPAM

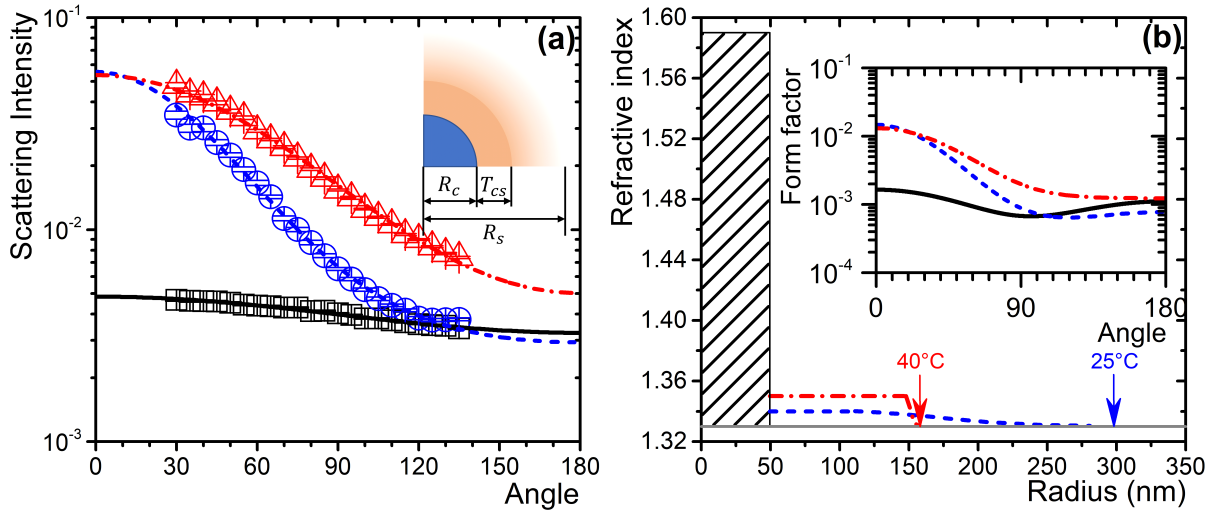

Figure 5.6: (a) Experimental temperature-dependent scattering intensity (arbitrary units) as a function of the scattering angle (degrees) of PS plain standard particles with 100 nm of mean diameter (black squares) and of PS/PNIPAM at 20 °C (blue circles) and 40 °C (red triangles). Models: homogeneous sphere for PS plain standard particles (black line); MSA2 for core/shell particles are indicated by the blue dashed and red dashed-dotted lines at 20 and 40 °C, respectively. The inset presents a cartoon of the core/shell particle structure. (b) RI profiles from fits the experimental data of PS/PNIPAM particles at 20 and 40 °C; the dashed rectangle represents the PS core. The inset presents the form factor fits for the PS plain and core/shell particles.

RI plateau must be at maximum, setting an upper search limit value for the PNIPAM RI plateau for 20 °C. Then, we first fit the data corresponding to 40 °C, setting the range of the PNIPAM RI plateau between the water RI and 1.46, where 1.46 is the RI plateau value fitted for the PNIPAM microgels (see sec. 4.3). The thickness search range is set between the core and hydrodynamic radius. The upper search limit for the particle radius at 20 and 40 °C is the hydrodynamic radius provided by DLS (see Table 5.3). To end this fit, we determined the PS/PNIPAM search ranges at 20 °C. We set the same search steps for the size, RI, and polydispersity parameters used in the MSA1 and MSA2 routines.

Table 5.3: Parameters for the MSA3 best fit from the experimental data of our PS/PNIPAM particles at 20 and 40 °C and the hydrodynamic radius measured by DLS, R_h^{DLS}. The radius and thickness values are in nanometers, the temperature is in °C, and κ is in arbitrary units.

		MSA3					
T	R_h^{DLS}	T_{PP}	n_{PP}	σ_{PP}	R_s	σ_s	κ
20	298	42.5	1.34	1.15	298	1.14	3.80
40	159.5	92.5	1.36	1.00	144	1.00	2.88

The best-fit value for the PS standard plain particles is $R = 51.3$ nm with a monodisperse distribution. The best-fit values for PS/PNIPAM particles are presented in Table 5.3. In all cases, the scattering intensities fit well with the experimental data, and these results could show that the shell grew with uniform size in our PS/PNIPAM synthesis. The structural differences of the shell due to the synthesis process can be observed below LCST, where the size of the PNIPAM RI plateau in the shell and the size of the shell are not monodisperse. Also, as observed in the hydrodynamic radius characterization by DLS (see Table 5.2), above the LCST, the particle size distribution is monodispersed. The best-fit parameters of MSA3 for our PS/PNIPAM particles at 20 and 40 °C are shown in Table 5.3.

In Fig. 5.6(b) is shown the radial RI profile for the MSA3 calculation obtained by the best fit to the experimental data. Here, we can observe that the coating is not very dense. Still, despite this, the scattering properties of the PS/PNIPAM particles are dominated by the optical and geometrical parameters of the shell. In the inset of Fig. 5.6(b) is shown the form factor functions, calculated using Eq. (2.16), corresponding to the best-fit scattering intensity of Fig. 5.6(a). The PS plain standard particles scatter in the Rayleigh scattering regime due to their small size. [27] The shell is responsible for losing the Rayleigh scattering behavior of our core/shell particles. As far as we know, our results are the first attempt to describe the form factor and RI profile of this kind of composite particle in the Mie Scattering regime. As a final remark, it's crucial to say that the RI profile model used to describe the dielectric properties for PS/PNIPAM core/shell particles is probably not suitable for describing PNIPAM coatings in whose synthesis other reagents, such as acrylic acid. The use of this reagent in the PNIPAM synthesis aims to reduce the optical contrast between the PNIPAM and the water. [14, 15, 64] This will be briefly discussed in the next section.

5.4 Light scatterd by PS/PNIPAM-co-Acc core/shell particles

Meng *et al.* studied the scattering properties of core-shell particle suspensions with a PS spherical core coated with PNIPAM crosslinked with acrylic acid (AAc). [15] The addition of AAc to PNIPAM reduces the density of the microgel shell, and the particle radius can be increased up to a factor of 2 compared to PNIPAM alone. [14] Consequently, PNIPAM-co-AAc is expected to absorb significantly more water than PNIPAM microgels, leading to a good refractive index match with water in the swollen state. [14] Our model can describe the form factor of core-shell composite particles reported by Meng et al., who measured the light scattering intensity at $\lambda = 532$ nm.

Fig. 9a presents the Meng et al. [15] experimental scattering intensity versus scattering angle of PS particles coated (PS/PNIPAM-co-AAc) and without coating (PS) at 25 °C (swollen state) and 35 °C (shrunk state). The experimental data for uncoated PS and PS/PNIPAM-co-AAc particles

at 25 °C are very similar, despite the hydrodynamic radius of PS/PNIPAM-co-AAc particles being ~ 850 nm, *i.e.*, approximately ten times the core radius. However, at 35 °C, the scattering intensity of PS/PNIPAM-co-AAc scatters light preferentially at small angles (forward scattering); here, the hydrodynamic radius is 438 nm.

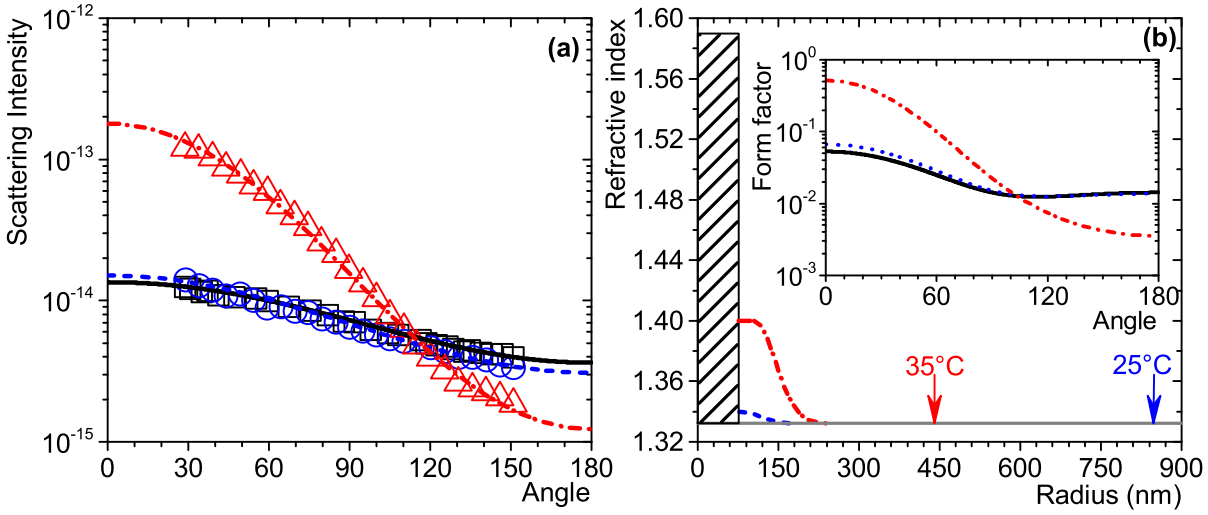

Figure 5.7: (a) Experimental temperature-dependent scattering intensity (arbitrary units) as a function of scattering angle (degrees) of plain PS particles (black squares) and of PS/PNIPAM-co-AAc at 25 °C (blue circles) and 35 °C (red triangles). Models: HSPH for plain PS particles (black line); MSA3 for core-shell particles (blue dashed and red dashed-dot lines) at 25 and 35 °C, respectively. (b) Radial RI profile obtained by fitting the experimental data of core/shell particles at 25 °C and 35 °C using MSA3. Arrows indicate the hydrodynamic radius. [15] A dashed rectangle represents the PS core, and the RI profile has the same color-line code as in Fig. 5.7(a). The inset of Fig. 5.7(b) presents the form factor fits for the PS plain and core/shell particles, shown with the same color-line code used in this figure.

.

We use the MSA3 procedure (see sec. 5.3 to fit the scattering intensity data measured in a vertical polarization setup. Here, we assume that PS/PNIPAM-co-AAc particles have a core with homogeneous RI. $n_{PSC} = 1.59$. The radius of the PS core was obtained from the best fit to PS plain experimental data, [15], and we considered that the PNIPAM-co-AAc shell has a Gaussian RI profile given by Eq. (4.1), consistent with previous systems studied in this dissertation. Fig. 5.7(a) presents our best fitting for different models, HSPH for PS plain particles and MSA3 for PS/PNIPAM-co-AAc particles at 25 and 35 °C. The best-fit value for the experimental data of the PS plain monodisperse particles is $R_c = 76$ nm. The best-fit value for the experimental data of the core-shell particles in hydrated (swollen) state is $R_s = 190$ nm, and in dehydrated (shrunk) state is $R_s = 247$ nm. Although the fitted scattering intensities agree well with the experimental data, the best-calculated shell radius in both cases underestimates the hydrodynamic radius measured by Meng et al. [15] The parameters for the best fit of MSA3 for PS/PNIPAM-co-AAc particles at 25

and 35 °C are in Table 5.4.

Fig. 5.7(b) presents the radial RI profile of the MSA3 obtained by the best fit to the experimental data. The RI remains relatively flat at 25 °C and decreases quickly at 35 °C. This behavior is likely due to the PNIPAM-co-AAc shell, which retains a significant amount of water even in the shrunk state. Under these conditions, the RI profile of the PNIPAM-co-AAc is probably not well described by a Gaussian decay. The inset of Fig. 5.7(b) shows the form factors for plain PS particles and PS/PNIPAM-co-AAc particles at 25 and 35 °C. As noted by Meng *et al.*, we also observed two main scattering features: (1) Below the LCST, the scattering properties are primarly determined by the PS core. 2) Above the LCST, scattering properties are influenced by both the core and the shrunk shell. [14, 15]

Table 5.4: The parameters for the MSA3 best fit to the experimental data for PS/PNIPAM-co-AAc particles at 25 °C and 35 °C, as well as the hydrodynamic radius measured by Meng, R_h^{e}. et al. [15] Radius and thickness values are given in nanometers, temperature in °C, and κ in arbitrary units.

		MSA3					
T	R_h^{e}	T_{PP}	n_{PP}	σ_{PP}	R_s	σ_s	κ ($\times 10^{-13}$)
25	847	1	1.34	1.00	190	1.11	2.59
35	438	74	1.40	1.00	247	1.01	4.44

Chapter 6

Conclusions

This thesis applies the Mie scattering solution for a multilayer sphere to predict and analyze the static light scattering of nonhomogeneous colloidal particles with spherical symmetry. The colloidal systems studied include pure PNIPAM particles and core-shell PS/PNIPAM and PS/PNIPAM-co-AAc particles. These systems were chosen for their potential applications in the design of optical devices, which served as the primary motivation for this research. The central objective is to reversibly tune the scattering properties of PNIPAM-based particles in order to achieve a distinctive transmittance spectrum [2, 14, 15].

Throughout this doctoral research, we observed that in PNIPAM light scattering experiments, the Mie scattering solution is not used by the soft matter physics community to describe the light scattering properties of nonhomogeneous colloidal particles with spherical symmetry. Instead, the Rayleigh-Gans-Debye (RGD) approximation is always employed, even when the system does not fully satisfy the validity conditions of RGD. This may lead to an inaccurate description of the light scattering properties of PNIPAM particles. [18, 24, 25]

One of the main reasons experimentalists prefer the RGD approximation over the Mie scattering solution is the mathematical complexity involved in the latter approach. [24, 26] However, various numerical methods are available to evaluate the Mie scattering solution for homogeneous and non-homogeneous particles with spherical symmetry. [27, 31, 38] In our work, we considered that Yang's formulation for the Mie scattering solution for a multilayer sphere provides the most intuitive and stable numerical scheme to describe the light scattered by nonhomogeneous spherical colloidal particles. Therefore, we adapted Yang's algorithm for our needs, and it was used to fit experimental data from static light scattering experiments successfully.

For this reason, the primary objective of this dissertation is to demonstrate that applying the Mie scattering solution for homogeneous and nonhomogeneous spheres for particles with spherical symmetry is now straightforward, provided their dielectric properties are known. To this end, this dissertation reviews the Mie scattering solution for homogeneous and multilayer spheres. It provides

numerical algorithms for both approaches, including algorithms to solve the average integrals for particles with size polydispersity, and they are available in our GitHub repository (`https://github.com/Complex-Fluids-IFUNAM/Mie-Scattering`) for anyone interested in using them. Finally, the developed numerical tools are applied to successfully study the light scattering of the particles of interest.

In this work, we employed a radial refractive index (RI) profile model for PNIPAM microgels that resembles the structure of a core-shell particle: a core with constant RI and a shell where the RI decays in a Gaussian manner until it matches that of the surrounding solvent (see Eq. (**??**)). After discretizing this RI profile, we applied the Mie scattering solution for a multilayer sphere to calculate the form factor functions of suspensions of PNIPAM, PS/PNIPAM, and PS/PNIPAM-co-AAc core/shell particles.

For the PNIPAM case presented in Chapter **??**, the scattering intensity in the swollen state is accurately predicted, as evidenced by the excellent agreement with experimental data reported in Ref. [18] (see Fig. **??**). In the shrunk state, however, the Gaussian RI profile combined with our polydispersity model does not describe the scattering properties effectively, as the microgel behaves more like a solid homogeneous sphere. In this regime, the Mie scattering solution for homogeneous spheres becomes more appropriate. As a future direction, it would be valuable to explore how variations in parameters such as core and shell polydispersity influence the form factor.

To the best of our knowledge, this is the first time the form factor of PNIPAM microgels in the swollen state has been described using the Mie scattering solution for a multilayer sphere with a refractive index profile based on the PNIPAM density distribution.

Chapter **??** details the synthesis and characterization of PS/PNIPAM core/shell particles. Their light scattering properties were successfully described using the Mie scattering solution for multilayer spheres. In this case, we proposed a discontinuous RI profile model, in which the PNIPAM shell was modeled in the same way as for the pure PNIPAM particles discussed in Chapter **??**.

Finally, in Chapter **??**, we explored the applicability of the same RI profile model to static light scattering data of PS/PNIPAM-co-AAc particles reported in Ref. [15]. PNIPAM-co-AAc absorbs significantly more water than conventional cross-linked PNIPAM microgels. Although the scattering intensity was well described using our RI profile and the Mie scattering solution for multilayer spheres, the fitted radii were notably smaller than the hydrodynamic radii reported by the authors. These results suggest that the refractive index distribution of PS/PNIPAM-co-AAc particles may be substantially more complex than that of conventional PNIPAM microgels, warranting further study to determine a more suitable RI profile model.

It is also important to note, as discussed in Section 2.1.4, that the Rayleigh-Gans-Debye (RGD) approximation is not valid for describing the light scattering properties of polystyrene particles in water. Consequently, it is also unsuitable for modeling the scattering of more complex particles that

incorporate a polystyrene core. The Mie scattering solution, derived from the full electromagnetic theory, provides an exact solution for the scattered field and establishes a direct relationship between the incident wave and the scattered intensity. In this way, it offers a significant improvement over the RGD approximation.

For all the reasons mentioned above, we conclude that the primary limitation in using the Mie scattering solution for homogeneous and multilayer spheres to study the light scattering properties of homogeneous and nonhomogeneous spherical particles is not the mathematical complexity of Mie solutions, but rather our lack of knowledge of the dielectric properties of the particles under study.

Chapter 7

Applications and future research directions

The results presented in this dissertation can be immediately used in many applications where a concise methodology was lacking to apply the Mie scattering solution to adequately describe light scattering experiments on particles where the RGD approximation is not valid. Next, some of the future research directions or applications are enumerated:

1. A natural extension of this experimental technique could be using the Mie scattering model for multilayered spheres to characterize more complex colloidal particles, like hollow sphere particles, multilayer composite colloidal particles, etc.

2. Our open-source computational programs for the Mie scattering solution could help to develop numerical tools for engineered particles with optical properties that are of scientific and technological interest, like the PNIPAM composite particles. [16, 17]

3. As Mie scattering solutions formulation includes imaginary refractive indices, our method is an alternative to the RGD approximation and Monte Carlo simulations to describe the absorption spectra of metallic core/shell gold particles coated with PNIPAM. [27] This kind of composite particle is currently being studied for its properties, which may be useful in biomedical applications and photonic technology [25]

4. Since the extinction cross-section is related to the scattered light and, consequently, to the amplitude scattering coefficients, the Mie scattering solutions can be related to light scattering spectroscopy, which looks for a nonintrusive characterization of submicron particles. The influence of the internal structure of nonhomogeneous particles on their radiative properties is an open issue in many fields of science and technology. [71, 72]

5. Our model for multilayered spheres could be a starting point for studying particles with spherical symmetry. Furthermore, video holographic microscopy characterization of colloidal spheres has been developed by fitting their measured hologram normalized images to a theoretical expression of these normalized images. It involves the Mie scattering coefficients of colloidal particles, whose radius and refractive index are free parameters. [73]

6. Knowing the light scattering of mesoscopic core-shell particles makes it possible to predict their photonic properties as the transport mean-free path of the light. The transport mean-free path of the light is closely related to pseudogaps in light transmittance through colloidal suspensions with strong short-range structural correlations. In this sense, for the systems studied in this thesis, the next step is to study the structural correlations of PNIPAM and PS/PNIPAM suspensions and include them in numerical schemes to predict the transmittance spectrum as a function of wavelength. [6, 8]

Appendix A

Vector harmonic functions

The Mie scattering solution introduces vector harmonic functions to simplify the mathematical representation of the incident, internal, and scattered electromagnetic fields. The derivation of these vector harmonic functions can be found in Bohren and Huffman's book. [27] They are defined as follows:

$$\begin{aligned}
\mathbf{M}_{o1n}^{z_n} &= \cos\varphi \pi_n z_n \hat{\mathbf{e}}_\theta - \sin\varphi \tau_n z_n \hat{\mathbf{e}}_\varphi, \\
\mathbf{M}_{e1n}^{z_n} &= -\sin\varphi \pi_n z_n \hat{\mathbf{e}}_\theta - \cos\varphi \tau_n z_n \hat{\mathbf{e}}_\varphi, \\
\mathbf{N}_{o1n}^{z_n} &= \sin\varphi n(n+1)\sin\theta \pi_n \frac{z_n}{\rho}\hat{\mathbf{e}}_r + \sin\varphi \tau_n \frac{[\rho z_n]'}{\rho}\hat{\mathbf{e}}_\theta + \cos\varphi \pi_n \frac{[\rho z_n]'}{\rho}\hat{\mathbf{e}}_\varphi, \\
\mathbf{N}_{e1n}^{z_n} &= \cos\varphi n(n+1)\sin\theta \pi_n \frac{z_n}{\rho}\hat{\mathbf{e}}_r + \cos\varphi \tau_n \frac{[\rho z_n]'}{\rho}\hat{\mathbf{e}}_\theta - \sin\varphi \pi_n \frac{[\rho z_n]'}{\rho}\hat{\mathbf{e}}_\varphi,
\end{aligned} \tag{A.1}$$

where z_n denotes the spherical Bessel function of the first kind $j_n(\rho)$, and the Hankel function of the first kind $h_n^{(1)}(\rho)$. The prime symbol denotes differentiation concerning ρ, where $\rho = kr$.

Using vector harmonic functions, it is possible to write the electromagnetic incident fields that define the incident plane wavefront as follows: [27]

$$\mathbf{E}_i = \sum_{n=1}^{\infty} E_n (c_n \mathbf{M}_{o1n}^{j_n(\rho)} - i d_n \mathbf{N}_{e1n}^{j_n(\rho)}), \tag{A.2}$$

$$\mathbf{H}_i = -\frac{k_1}{\omega \mu_1} \sum_{n=1}^{\infty} E_n (d_n \mathbf{M}_{e1n}^{j_n(\rho)} - i c_n \mathbf{N}_{o1n}^{j_n(\rho)}). \tag{A.3}$$

References

[1] Diederik S. Wiersma. Disordered photonics. *Nature Photonics*, 7:188–196, 3 2013.

[2] Kevin Vynck, Romain Pierrat, Rémi Carminati, Luis S. Froufe-Pérez, Frank Scheffold, Riccardo Sapienza, Silvia Vignolini, and Juan José Sáenz. Light in correlated disordered media. *Reviews of Modern Physics*, 95:045003, 11 2023.

[3] Bahaa E. A. Saleh and Malvin Carl Teich. *Fundamentals of Photonics*. John Wiley Sons, Inc., 8 1991.

[4] Alexander Dorodnyy, Jasmin Smajic, and Juerg Leuthold. Mie scattering for photonic devices. *Laser Photonics Reviews*, 17, 9 2023.

[5] P. D. Kaplan, Ming Hsii Kao, A. G. Yodh, and David J. Pine. Geometric constraints for the design of diffusing-wave spectroscopy experiments. *Applied Optics*, 32:3828, 7 1993.

[6] Mathias Reufer, Luis Fernando Rojas-Ochoa, Stefanie Eiden, Juan José Sáenz, and Frank Scheffold. Transport of light in amorphous photonic materials. *Applied Physics Letters*, 91:171904, 10 2007.

[7] Victoria Hwang, Anna B. Stephenson, Sofia Magkiriadou, Jin Gyu Park, and Vinothan N. Manoharan. Effects of multiple scattering on angle-independent structural color in disordered colloidal materials. *Physical Review E*, 101:1–11, 2020.

[8] L. F. Rojas-Ochoa, J. M. Mendez-Alcaraz, J. J. Sáenz, P. Schurtenberger, and F. Scheffold. Photonic properties of strongly correlated colloidal liquids. *Physical Review Letters*, 93:073903, 8 2004.

[9] P.D. García, R. Sapienza, Á. Blanco, and C. López. Photonic glass: A novel random material for light. *Advanced Materials*, 19:2597–2602, 9 2007.

[10] Pierre Barthelemy, Jacopo Bertolotti, and Diederik S. Wiersma. A lévy flight for light. *Nature*, 453:495–498, 5 2008.

[11] Benedikt Groever, Barmak Heshmat, and Ramesh Raskar. Tyndall windows: Tunable scattering of disordered solid-liquid matching mixtures. *ACS Photonics*, 3:930–935, 6 2016.

[12] Mengchun Wu, Yusuf Shi, Renyuan Li, and Peng Wang. Spectrally selective smart window with high near-infrared light shielding and controllable visible light transmittance. *ACS Applied Materials and Interfaces*, 10:39819–39827, 11 2018.

[13] Amanda Eklund, Shanming Hu, Yuhuang Fang, Henri Savolainen, Haotian Pi, Hao Zeng, Arri Priimagi, Olli Ikkala, and Hang Zhang. Bright and switchable whiteness in macro-crosslinked hydrogels. *Advanced Optical Materials*, 12, 4 2024.

[14] Adeline Perro, Guangnan Meng, Jerome Fung, and Vinothan N. Manoharan. Design and synthesis of model transparent aqueous colloids with optimal scattering properties. *Langmuir*, 25:11295–11298, 2009.

[15] Guangnan Meng, Vinothan N. Manoharan, and Adeline Perro. Core-shell colloidal particles with dynamically tunable scattering properties. *Soft Matter*, 13:6293–6296, 2017.

[16] Thomas Hellweg. Responsive core-shell microgels: Synthesis, characterization, and possible applications. *Journal of Polymer Science Part B: Polymer Physics*, 51:1073–1083, 7 2013.

[17] Matthias Ballauff and Yan Lu. "smart" nanoparticles: Preparation, characterization and applications. *Polymer*, 48:1815–1823, 2007.

[18] M. Reufer, P. Díaz-Leyva, I. Lynch, and F. Scheffold. Temperature-sensitive poly(n-isopropylacrylamide) microgel particles: A light scattering study. *European Physical Journal E*, 28:165–171, 2 2009.

[19] Robert Pelton. Temperature-sensitive aqueous microgels. *Advances in Colloid and Interface Science*, 85:1–33, 2 2000.

[20] Avraham Halperin, Martin Kröger, and Françoise M. Winnik. Poly(n -isopropylacrylamide) phase diagrams: Fifty years of research. *Angewandte Chemie International Edition*, 54:15342–15367, 12 2015.

[21] Frank Scheffold. Pathways and challenges towards a complete characterization of microgels. *Nature Communications*, 11:4315, 9 2020.

[22] Markus Stieger, Walter Richtering, Jan Skov Pedersen, and Peter Lindner. Small-angle neutron scattering study of structural changes in temperature sensitive microgel colloids. *Journal of Chemical Physics*, 120:6197–6206, 4 2004.

[23] Mónica Ledesma-Motolinía, Marco Braibanti, Luis F. Rojas-Ochoa, and Catalina Haro-Pérez. Interplay between internal structure and optical properties of thermosensitive nanogels. *Colloids and Surfaces A: Physicochemical and Engineering Aspects*, 482:724–727, 10 2015.

[24] O. L. J. Virtanen, A. Mourran, P. T. Pinard, and W. Richtering. Persulfate initiated ultra-low cross-linked poly(n-isopropylacrylamide) microgels possess an unusual inverted cross-linking structure. *Soft Matter*, 12:3919–3928, 2016.

[25] Ekaterina Ponomareva, Ben Tadgell, Marco Hildebrandt, Marcel Krüsmann, Sylvain Prévost, Paul Mulvaney, and Matthias Karg. The fuzzy sphere morphology is responsible for the increase in light scattering during the shrinkage of thermoresponsive microgels. *Soft Matter*, 18:807–825, 1 2022.

[26] B.R Jennings and H.G Jerrard. Rayleigh-gans-debye and mie theories in the determination of spherical particle sizes. *Journal of Colloid Science*, 20:448–452, 6 1965.

[27] Craig F. Bohren and Donald R. Huffman. *Absorption and Scattering of Light by Small Particles*. Wiley, 4 1998.

[28] Andrew Zangwill. *Modern Electrodynamics*. Cambridge University Press, 12 2012.

[29] O. Glatter. Neutrons, x-rays and light: Scattering methods applied to soft condensed matter. North Holland Delta Series, 2002.

[30] Jasmin Simons, Nabanita Hazra, Alexander V. Petrunin, Jérôme J. Crassous, Walter Richtering, and Max Hohenschutz. Nonionic microgels adapt to ionic guest molecules: Superchaotropic nanoions. *ACS Nano*, 18:7546–7557, 3 2024.

[31] Thomas Wriedt. Mie theory: A review. *Springer Series in Optical Sciences*, 169:53–71, 2012.

[32] W. J. Wiscombe. Improved mie scattering algorithms. *Applied Optics, Vol. 19, Issue 9, pp. 1505-1509*, 19:1505–1509, 5 1980.

[33] Milton Abramowitz and Irene A. Stegun. *Handbook of Mathematical Functions with formulas, graphs, and mathematical tables*. Dover Publications, 1965.

[34] Inc. Bangs Laboratories. Physical properties of polymer and silica. `https://bangslabs.com/technical-library/physical-properties-of-polymer-and-silica/`. accessed: 2025-05-23.

[35] Arthur L. Aden and Milton Kerker. Scattering of electromagnetic waves from two concentric spheres. *Journal of Applied Physics*, 22:1242–1246, 10 1951.

[36] Milton. Kerker. *The Scattering of Light and Other Electromagnetic Radiation*. Elsevier, 1969.

[37] B. R. Johnson. Light scattering by a multilayer sphere. *Applied Optics*, 35:3286, 6 1996.

[38] Wen Yang. Improved recursive algorithm for light scattering by a multilayered sphere. *Applied Optics*, 42:1710, 3 2003.

[39] Andrea Di Falco, Susanne C. Kehr, and Ulf Leonhardt. Luneburg lens in silicon photonics. *Optics Express*, 19:5156, 3 2011.

[40] Isabelle Staude and Jörg Schilling. Metamaterial-inspired silicon nanophotonics. *Nature Photonics*, 11:274–284, 5 2017.

[41] John C Thomas. The determination of log normal particle size distributions by dynamic light scattering. *Journal of Colloid and Interface Science*, 117:187–192, 5 1987.

[42] L B Kiss, J Söderlund, G A Niklasson, and C G Granqvist. New approach to the origin of lognormal size distributions of nanoparticles. *Nanotechnology*, 10:25–28, 3 1999.

[43] Natalia Farkas and John A. Kramar. Dynamic light scattering distributions by any means. *Journal of Nanoparticle Research*, 23:120, 5 2021.

[44] Arturo Quirantes, Rosario Plaza, and Angel Delgado. Static light scattering study of size parameters in core-shell colloidal systems. *Journal of Colloid and Interface Science*, 189:236–241, 1997.

[45] Gualberto J. Ojeda-Mendoza, Humberto Contreras-Tello, and Luis F. Rojas-Ochoa. Refractive index matching of large polydisperse silica spheres in aqueous suspensions. *Colloids and Surfaces A: Physicochemical and Engineering Aspects*, 538:320–326, 2 2018.

[46] W. F. Espenscheid, M. Kerker, and E. Matijević. Logarithmic distribution functions for colloidal particles. *The Journal of Physical Chemistry*, 68:3093–3097, 11 1964.

[47] William D Ross. Logarithmic distribution functions for particle size. *Journal of Colloid and Interface Science*, 67:181–182, 10 1978.

[48] William H. Press, Brian P. Flannery, Saul A. Teukolsky, and William T. Vetterling. *Numerical Recipes in Fortran 77: The Art of Ccientific Computing*. Cambrige University Press, second edition, 1992.

[49] G. M. Phillips and P. J. Taylor. *Theory and Applications of Numerical Analysis*. Academic Press, second edition, 1996.

[50] Renliang Xu. Light scattering: A review of particle characterization applications. *Particuology*, 18:11–21, 2 2015.

[51] Peter Schurtenberger and Meredith E. Newman. *Characterization of Biological and Environmental Particles Using Static and Dynamic Light Scattering*, volume 2. CRC Press, 2018.

[52] Otto Glatter. *Scattering Methods and Their Application on Colloid and Interface Science.* Elsevier, 2018.

[53] Kayori Takahashi, Atsushi Takano, Shinichi Kinugasa, and Hiromu Sakurai. Determination of the rayleigh ratio with an uncertainty analysis by static light-scattering measurements of certified reference materials for molecular weight. *Analytical Sciences*, 35:1045–1051, 9 2019.

[54] Robert Pecora, editor. *Dynamic Light Scattering.* Springer US, 1985.

[55] P.N. Pusey and W. Van Megen. Dynamic light scattering by non-ergodic media. *Physica A: Statistical Mechanics and its Applications*, 157:705–741, 6 1989.

[56] Pavel Zakharov and Frank Scheffold. *Advances in dynamic light scattering techniques*, pages 433–467. Springer Berlin Heidelberg, 2009.

[57] Barbara J. Frisken. Revisiting the method of cumulants for the analysis of dynamic light-scattering data. *Applied Optics*, 40:4087, 8 2001.

[58] Frank Babick. *Dynamic light scattering (DLS)*, pages 137–172. Elsevier, 1 2020.

[59] Sergey K. Filippov, Ramil Khusnutdinov, Anastasiia Murmiliuk, Wali Inam, Lucia Ya. Zakharova, Hongbo Zhang, and Vitaliy V. Khutoryanskiy. Dynamic light scattering and transmission electron microscopy in drug delivery: a roadmap for correct characterization of nanoparticles and interpretation of results. *Materials Horizons*, 10:5354–5370, 2023.

[60] Robert Pelton. Poly(n-isopropylacrylamide) (pnipam) is never hydrophobic. *Journal of Colloid and Interface Science*, 348:673–674, 8 2010.

[61] Haydn Mitchell, Spencer Schultz, Philip Costanzo, and Andres Martinez. Poly(n-isopropylacrylamide) hydrogels for storage and delivery of reagents to paper-based analytical devices. *Chromatography*, 2:436–451, 7 2015.

[62] Franziska Obst, Anthony Beck, Chayan Bishayee, Philipp J. Mehner, Andreas Richter, Brigitte Voit, and Dietmar Appelhans. Hydrogel microvalves as control elements for parallelized enzymatic cascade reactions in microfluidics. *Micromachines*, 11:167, 2 2020.

[63] Martin Dulle, Sarah Jaber, Sabine Rosenfeldt, Aurel Radulescu, Stephan Förster, Paul Mulvaney, and Matthias Karg. Plasmonic gold–poly(n-isopropylacrylamide) core–shell colloids with homogeneous density profiles: a small angle scattering study. *Physical Chemistry Chemical Physics*, 17:1354–1367, 2015.

[64] Sofia Magkiriadou, Jin-Gyu Park, Young-Seok Kim, and Vinothan N. Manoharan. Disordered packings of core-shell particles with angle-independent structural colors. *Optical Materials Express*, 2:1343, 10 2012.

[65] Jae Hyung Cho, Roberto Cerbino, and Irmgard Bischofberger. Emergence of multiscale dynamics in colloidal gels. *Physical Review Letters*, 124:088005, 2 2020.

[66] Julian Oberdisse and Thomas Hellweg. Recent advances in stimuli-responsive core-shell microgel particles: synthesis, characterisation, and applications. *Colloid and Polymer Science*, 298:921–935, 7 2020.

[67] Dongmei Zhu, Fei Wang, Cuiling Gao, and Zheng Xu. Construction of ps/pnipam core-shell particles and hollow spheres by using hydrophobic interaction and thermosensitive phase separation. *Frontiers of Chemical Engineering in China*, 2:253–256, 9 2008.

[68] Inc. Bang Laboratories. Safety data sheet for polystyrene spheres. `h0ttps://bangslabs.com/wp-content/uploads/SDS_PG110.pdf`. accessed: 2025-05-23.

[69] In-Hwa Choi and Joon-Seop Kim. Glass transition temperature of styrene-based ionomer controlled over a very wide temperature range by nonpolar plasticizer content and ion content. *Journal of Applied Polymer Science*, 140, 11 2023.

[70] Min Zhang, Yuan Li, Qili Yang, Liulian Huang, Lihui Chen, and Huining Xiao. Adsorption of methyl violet using ph- and temperature-sensitive cellulose filament/poly(nipam-co-aac) hybrid hydrogels. *Journal of Materials Science*, 53:11837–11854, 8 2018.

[71] R.E.H. Miles, A.E. Carruthers, and J.P. Reid. Novel optical techniques for measurements of light extinction, scattering and absorption by single aerosol particles. *Laser Photonics Reviews*, 5:534–552, 7 2011.

[72] I.T. Horvath, P. Colinet, and M.R. Vetrano. Assessment of the light extinction spectroscopy technique for submicron particle characterization. *Powder Technology*, 291:375–382, 4 2016.

[73] Sang-Hyuk Lee, Yohai Roichman, Gi-Ra Yi, Shin-Hyun Kim, Seung-Man Yang, Alfons van Blaaderen, Peter van Oostrum, and David G. Grier. Characterizing and tracking single colloidal particles with video holographic microscopy. *Optics Express*, 15:18275, 12 2007.